

Simulation of advection at the sea surface based on a velocity field reconstructed from point measurements: doctoral thesis

Jakac, Karlo

Doctoral thesis / Doktorski rad

2025

Degree Grantor / Ustanova koja je dodijelila akademski / stručni stupanj: **University of Rijeka, - FACULTY OF ENGINEERING / Sveučilište u Rijeci, - Tehnički fakultet**

Permanent link / Trajna poveznica: <https://um.nsk.hr/um:nbn:hr:190:612715>

Rights / Prava: [Imenovanje 4.0 međunarodna](#) / [Attribution 4.0 International](#)

Download date / Datum preuzimanja: **2026-03-20**



Repository / Repozitorij:

[Repository of the University of Rijeka, Faculty of Engineering / Repozitorij Tehničkog fakulteta u Rijeci](#)



UNIVERSITY OF RIJEKA
FACULTY OF ENGINEERING

Karlo Jakac

**SIMULATION OF ADVECTION AT THE
SEA SURFACE BASED ON A VELOCITY
FIELD RECONSTRUCTED FROM POINT
MEASUREMENTS**

DOCTORAL THESIS

Rijeka, 2025

UNIVERSITY OF RIJEKA
FACULTY OF ENGINEERING

Karlo Jakac

**SIMULATION OF ADVECTION AT THE
SEA SURFACE BASED ON A VELOCITY
FIELD RECONSTRUCTED FROM POINT
MEASUREMENTS**

DOCTORAL THESIS

Supervisor: Assoc. Prof. Stefan Ivić, PhD

Rijeka, 2025

SVEUČILIŠTE U RIJECI
TEHNIČKI FAKULTET

Karlo Jakac

**SIMULACIJA ADVEKCIJE NA MORSKOJ
POVRŠINI TEMELJENA NA POLJU
BRZINE REKONSTRUIRANOM IZ
TOČKASTIH MJERENJA**

DOKTORSKI RAD

Rijeka, 2025.

Doctoral thesis supervisor: Assoc. Prof. Stefan Ivić, PhD

The doctoral thesis was defended on _____ at the University of Rijeka, Faculty of Engineering, Croatia, in front of the following Evaluation Committee:

1. Prof. Siniša Družeta, PhD, University of Rijeka, Faculty of Engineering
2. Assoc. Prof. Bojan Crnković, PhD, University of Rijeka, Faculty of Mathematics
3. Prof. Hrvoje Kozmar, PhD, University of Zagreb, Faculty of Mechanical Engineering and Naval Architecture

ABSTRACT

Accurate assessment of the sea surface velocity field is essential for various applications, particularly for predicting the movement of objects and substances on the sea surface, as well as for search and rescue (SAR) operations. However, reconstructing the full flow field from sparse and scattered observations is both difficult and computationally demanding. This challenge is compounded by the highly dynamic and variable nature of oceanic flows, which makes accurate prediction of surface transport even with advanced measurement techniques such as coastal radar systems or high-resolution numerical ocean models particularly challenging, especially in time-sensitive scenarios.

To address these challenges, this thesis proposes a rapid, data-driven approach for reconstructing sea surface velocity fields from sparsely distributed measurements. The flow field is represented using two simplified two-dimensional models that together capture submesoscale dynamics across the entire domain while enabling near-real-time computation. To ensure reliable prediction of object trajectories and target probabilities, the framework incorporates model of passive scalar advection with compensating diffusion, explicitly accounting for flow reconstruction errors, measurement noise, and other system uncertainties. The central hypothesis of this work is that realistic sea surface flow patterns can be effectively approximated by iteratively fitting a steady-state numerical surrogate model to real-time scattered measurements, thereby avoiding the computational cost of complex oceanic models. This approach enables continuous updates of the target probability distribution representing its possible location in realistic search scenarios.

This research introduces several methodological innovations essential for implementing the proposed concept. The fusion methodology converts scattered velocity measurements into a coherent flow field using a novel surrogate modeling approach that preserves key flow dynamics while maintaining computational efficiency. Numerical optimization algorithms are employed to iteratively adjust model parameters and boundary conditions, ensuring that the reconstructed fields remain consistent with observational constraints. The quasi-steady implementation captures temporal flow evolution through periodic field updates rather than continuous

time-dependent simulations, substantially reducing computational overhead.

The methodology was systematically validated through simulation tests and real-world field trials. In these trials, GPS drifters measured sea surface velocities, while purpose-deployed marine targets served as test objects for trajectory prediction. Unmanned Aerial Vehicles provided aerial tracking and verification of target movements, based on its advected probability, as well as searching for and locating custom sea targets based on their estimated trajectories. Validation was achieved by comparing observed drifter paths with predictions generated exclusively from the reconstructed flow fields, allowing direct assessment of accuracy under realistic operational conditions.

The results demonstrate that the proposed concept successfully balances computational efficiency with the fidelity of the reconstructed flow field. It provides flow and advection reconstructions that are sufficiently accurate for operational decision-making, while being fast enough to support real-time or near-real-time applications. These outcomes highlight its potential as a practical operational tool for time-critical maritime applications, particularly in scenarios where traditional high-resolution simulations are computationally prohibitive and rapid response is required.

Keywords: Velocity field reconstruction, Point measurements, Surrogate model, Model fitting, Advection, Diffusion, Computational Fluid Dynamics

PROŠIRENI SAŽETAK

Pouzdana procjena polja brzine morske površine ključna je za brojne primjene, osobito za praćenje kretanja objekata i tvari na površini mora, kao i za operacije traganja i spašavanja. Međutim, rekonstrukcija cjelokupnog strujnog polja na temelju rijetkih i prostorno razbacanih mjerenja istodobno je zahtjevna i računalno skupa. Izrazito dinamična i promjenjiva priroda oceanskih strujanja dodatno otežava precizno predviđanje površinskog transporta, koje ostaje izazovno čak i uz napredne tehnologije poput obalnih radara i visokorezolucijskih numeričkih oceanskih modela u vremenski osjetljivim situacijama.

Strujno polje aproksimira se pomoću dva pojednostavljena dvodimenzionalna modela koji zajedno obuhvaćaju submezoskalnu dinamiku na cijelom području, a pritom omogućuju izračune gotovo u stvarnom vremenu. Kako bi se osiguralo pouzdano predviđanje putanja objekata i vjerojatnosti nalaženja mete, sustav uključuje model advekcije pasivnog skalara s kompenzacijskom difuzijom, pri čemu se eksplicitno uzimaju u obzir pogreške rekonstrukcije polja, šum mjerenja i druge nesigurnosti sustava. Središnja hipoteza ovog rada jest da se realistični obrasci strujanja morske površine mogu učinkovito aproksimirati iterativnim prilagođavanjem stacionarnog numeričkog surogat-modela stvarnim prostorno razbacanim mjerenjima, čime se izbjegava računalna zahtjevnost složenih oceanskih modela. Ovakav pristup omogućuje kontinuirano ažuriranje distribucije vjerojatnosti nalaženja mete u realnim scenarijima pretraživanja.

Ovo istraživanje uvodi nekoliko metodoloških inovacija ključnih za provedbu predloženog koncepta. Metodologija fuzije strujnih polja površine mora pretvara razbacana mjerenja brzina u koherentno strujno polje koristeći novi pristup surogatnog modeliranja koji zadržava ključne dinamike strujanja, a istovremeno održava računalnu učinkovitost. Numerički optimizacijski algoritmi koriste se za iterativno prilagođavanje parametara modela i rubnih uvjeta, osiguravajući da rekonstruirana polja ostanu usklađena s dostupnim mjerenjima i fizičkim ograničenjima. Kvazi-stacionarna implementacija bilježi vremenski razvoj strujanja kroz periodična ažuriranja strujnih polja, umjesto kontinuiranih vremenski ovisnih simulacija, što znatno smanjuje računalno opterećenje.

Metodologija je sustavno validirana kroz simulacijske testove i stvarne terenske eksperimente. U tim eksperimentima, GPS drifteri mjerili su brzine morske površine, dok su namjenski postavljeni morske mete služile kao objekti za predviđanje putanja. Bepilotne letjelice pružale su zračno praćenje i verifikaciju kretanja meta, temeljeno na advekciji gustoće vjerojatnosti njihova nalaska, kao i traženje i lociranje meta na temelju njihovih procijenjenih putanja. Validacija je provedena usporedbom promatranih putanja driftera s predviđanjima generiranim isključivo iz rekonstruiranih strujnih polja, što je omogućilo izravnu procjenu točnosti u realnim operativnim uvjetima.

Rezultati pokazuju da predloženi koncept uspješno uravnotežuje računalnu učinkovitost i vjerodostojnost rekonstruiranog strujnog polja. Rekonstrukcije strujnog polja i advekcije dovoljno su precizne za operativno donošenje odluka, a istovremeno dovoljno brze da podrže primjene u stvarnom ili gotovo stvarnom vremenu. Ovi ishodi ističu njegov potencijal kao praktičnog operativnog alata za vremenski kritične pomorske primjene, osobito u scenarijima gdje su tradicionalne visokorezolucijske simulacije računalno zahtjevne, a potrebna je brza reakcija.

Ključne riječi: Rekonstrukcija polja brzine, Točkasta mjerenja, Surogat-model, Prilagodba modela, Advekcija, Difuzija, Računalna dinamika fluida

CONTENTS

1	Introduction	1
1.1	Hypothesis and Research Goals	2
1.2	Scientific Contribution	2
1.3	Thesis Structure	3
2	Literature overview	5
2.1	Sea surface velocity reconstruction	5
2.1.1	Acquiring velocity data	5
2.1.2	Reconstruction techniques	7
2.1.2.1	Spatial interpolation methods	8
2.1.2.2	Data Assimilation	9
2.1.2.3	Machine Learning and Hybrid approaches	9
2.2	Advection and transport modeling at the sea surface	11
2.2.1	Lagrangian vs. Eulerian approaches	12
2.2.2	Computational models	13
2.3	Applications in Search and Rescue	15
3	Technology of sea surface velocity measurements	17
3.1	Floating sensors	17
3.2	High-Frequency (HF) radar systems	19
3.3	Satellite-based surface velocity measurements	21
3.4	Measurement uncertainty	23
3.5	Effective number of measurements	23
4	Dynamics of sea surface drift	27
4.1	Drift of floating objects	27
4.2	Influence of object shape and environmental factors	28

5	Surrogate modeling of sea surface dynamics	30
5.1	Steady 2D flow model	31
5.2	Fusion model	32
5.3	Transient flow estimation	34
5.4	Numerical implementation	35
5.4.1	Governing Equations of Fluid Flow	35
5.4.1.1	Conservation of Mass	35
5.4.1.2	Conservation of Momentum	36
5.4.1.3	Conservation of Energy	37
5.4.2	Principles of the Finite Volume Method	38
5.4.3	Turbulence	39
5.4.4	Numerical simulations in OpenFOAM	40
5.4.5	Boundary conditions	41
6	Model fitting framework	44
6.1	Objectives	45
6.2	Constraints	46
6.3	Progressive field initialization and search narrowing	47
6.4	Modeling drifter advection	49
7	Advection diffusion processes	51
7.1	Passive scalar transport	51
7.2	Assessment of passive scalar field advection accuracy	52
7.3	Adaptive diffusion coefficient	54
7.4	Application in dynamic search scenarios	55
7.4.1	Dynamic probability distribution field	56
7.4.2	Search agent motion model	57
7.4.3	Implementation of the integrated search framework	59
8	Simulation results	61
8.1	Preparation of test cases	61
8.2	Analysis of steady flow reconstruction approach	64
8.2.1	Multimodality	64
8.2.2	Optimization methods and benchmark	65

8.2.3	Impact of available measurements on flow reconstruction accuracy . . .	69
8.2.4	Mesh independence	71
8.2.5	Case studies of Steady Flow Fit	71
8.2.5.1	Gulf of Trieste	72
8.2.5.2	Vis island	75
8.3	Analysis of transient flow reconstruction	76
8.3.1	Robustness analysis of quasi-steady period	77
8.3.2	Case studies of Transient Flow Fit	78
8.3.2.1	Simple bay	79
8.3.2.2	Unije Channel	81
9	Experimental results	84
9.1	Equipment and preparation	84
9.2	Plomin Bay flow experiment	89
9.3	Valun Bay flow experiment	92
9.4	Valun Bay search experiment	98
10	Limitations and discussion	107
11	Conclusion	111
	Bibliography	113
	List of Figures	131
	List of Tables	136
	Curriculum Vitae	137
	List of Publications	138

1 INTRODUCTION

Objects and substances floating on the sea surface, such as debris, oil spills, or drifting vessels, are constantly in motion due to currents, wind, and waves. Understanding and predicting these movements is crucial for a wide range of applications, including search and rescue (SAR) operations, environmental monitoring, pollution control, and maritime navigation. This physical phenomenon is known as advection, which in this specific instance refers to the transport of material/objects by the surface flow. Additionally, floating materials tend to gradually spread out on the surface over time, moving from areas of higher concentration to areas of lower concentration, in a process known as diffusion.

Accurately modeling both advection and diffusion requires insight into the sea surface velocity field, which can be obtained or estimated through various measurement techniques, each suited to different environments and applications. For instance, fixed systems like coastal radar provide continuous coverage in nearshore regions, while mobile platforms such as floating sensors (drifters) offer flexibility and precision in open waters. If large-scale areas need to be monitored, satellite-based observations can provide wide coverage, although they typically offer low resolution and limited accessibility to frequent updates.

While current approaches to surface flow reconstruction are effective in certain respects, they often lack detail regarding specific flow field characteristics, accuracy, and spatial or temporal resolution. To overcome these limitations, this research proposes a modeling approach in which numerical simulations from Computational Fluid Dynamics (CFD) are combined with available point measurements of sea surface velocity. Since point measurements provide ad hoc data, this approach reduces both the cost and effort associated with data acquisition. Due to the complexity of oceanic models, a simplified numerical surrogate model is introduced to ensure near real-time applicability. This flow surrogate model is iteratively adjusted until the resulting velocity fields align with the measurements. The method not only provides reliable velocity approximations across the entire domain but also enables predictions of object trajectories and probability field advection.

1.1 Hypothesis and Research Goals

Earlier studies on velocity field reconstruction, particle and object advection, and scalar transport with diffusion have largely relied on available measurements to derive flow fields. However, these approaches often required extensive data, while still neglecting important aspects of sea flow complexity. From these limitations, the research hypothesis emerges:

- A meta-model-based reconstruction of the sea surface flow field using a small number of drifter measurements is suitable for accurate modelling and prediction of target probability density dynamics.

The research goals are:

- Develop a rapid approximation method for sea surface velocity estimation using scattered drifter measurements.
- Apply the surrogate modeling approach to fit numerical simulations with available data for efficient flow field reconstruction.
- Analyze and predict the advection of objects or target probability fields based on the reconstructed velocity fields.
- Assess the applicability of the proposed methodology for mesoscale processes and operational modeling.
- Perform numerical and experimental validation of the methodology under realistic conditions.

1.2 Scientific Contribution

The scientific contribution of the proposed research lies in the development of a rapid approximation method for surface flow reconstruction using a surrogate model that replicates realistic submesoscale flow. This approach enables fast and detailed assessment of the surface velocity field from a limited number of measurements, reducing both the cost and time associated with flow reconstruction. Moreover, it provides an adequate velocity field for the entire simulated domain, including areas not covered with measurements.

The framework is easily extended to incorporate the advection of particles or objects, as well as passive scalar advection and diffusion, making it suitable for modeling and predicting target probability density dynamics. Additionally, it includes an auto-adaptive mechanism that compensates for potential measurement errors and flow reconstruction inaccuracies using a diffusion, enabling dynamic updates of the target probability distribution. The framework has been validated through numerical simulations in both synthetic and realistic domains. Its performance was further confirmed in carefully designed experiments using custom drifters, which addressed practical challenges such as drifting dynamics and data transmission, as well as realistic search scenarios involving Unmanned Aerial Vehicle (UAV) operations to locate deployed custom sea targets based on their estimated movements.

1.3 Thesis Structure

This thesis is organised into eleven chapters with corresponding subchapters. The introductory chapter presents the hypothesis and research goals, outlines the scientific contributions, and describes the overall thesis structure.

The second chapter provides an overview of scientific literature covering sea surface velocity reconstruction, advection and transport modeling at the sea surface, and applications in search and rescue.

The third presents the technology behind sea surface velocity measurement techniques. It covers data collection methods, including floating sensors (drifters), high-frequency radar systems, and satellite-based measurements, and discusses measurement uncertainties and spatial resolution, along with a proposal for the effective number of measurements.

The fourth chapter examines the dynamics of sea surface drift. It covers the drift of floating objects, influence of object shape, environmental factors, and overall complexity of the drift phenomenon.

The fifth chapter introduces the surrogate modeling approach for surface flow. It covers a steady two-dimensional model, the fusion model concept, a transient flow estimation method based on quasi-steady assumptions, and the numerical implementation of the proposed approach.

The sixth chapter focuses on the formulation of the model fitting and optimization problem, defining the objective functions and constraints.

The seventh chapter addresses advection–diffusion processes, including the formulation of the advection–diffusion term, modeling of passive scalar transport, evaluation of advection accuracy, proposal of an adaptive diffusion coefficient, and discussion of applications in search and rescue.

The eighth chapter presents simulation results from various test cases. It covers the preparation of synthetic and realistic domains, examines multimodality, compares optimization methods, analyzes robustness, investigates mesh independence, and validates the results.

The ninth chapter details the experimental results, describing preliminary and search experiments conducted in the areas of Plomin and Cres, Croatia. These experiments validate the proposed methodology and illustrate a practical application of the developed methods.

The tenth chapter discusses limitations of the current research, reflecting on challenges encountered and potential areas for improvement. The final chapter summarizes the main findings and scientific contributions, and confirms the thesis hypothesis.

2 LITERATURE OVERVIEW

In recent decades, accurately predicting the movement of objects and substances at sea has been a major challenge, particularly in search and rescue operations and environmental emergencies. Such incidents make rapid and informed decision-making crucial, especially when events like hazardous material pollution pose significant risks to marine ecosystems and coastal communities [1–4]. A variety of numerical models are regularly adopted to simulate the transport and distribution of probability densities representing the likely location of drifting objects or concentrations of pollutants, often serving as the most practical tool for forecasting their movement at sea. The performance of these models depends heavily on the quality of input data, including sea surface velocities, wind measurements, and the precise location of the source. Accurate reconstruction of surface flow is therefore a key prerequisite for reliable transport modeling and underpins numerous real-world applications, from tracking floating debris and locating lost objects to supporting search and rescue operations.

2.1 Sea surface velocity reconstruction

Generally, all transport modeling and prediction methods depend on sea surface velocity fields calculated from a variety of data sources. These sources vary quite a bit in how they measure velocity, how often and where they collect data, and how accurate they are. Knowing the strengths and weaknesses of each method is important for choosing the right data and building accurate surface flow maps. The following section reviews common velocity measurement methods and their roles in ocean surface flow reconstruction.

2.1.1 Acquiring velocity data

Among the different methods for measuring sea surface velocity, satellite-tracked drifters have become widely used due to their affordability and reliable performance. Over the past two

decades, their use has grown significantly, with many deployments across different ocean regions [5]. These floating devices, designed specifically to record surface current data and to study circulation patterns, particularly in semi-enclosed seas, have been the subject of extensive research and analysis [6–9]. They typically use Global Positioning System (GPS) technology to enable continuous tracking, providing valuable information about ocean surface dynamics and circulation patterns. However, drifters can sometimes move outside the area of interest, leading to widely scattered measurements that don't provide usable data. Moreover, because they only collect measurements at specific points, they can't offer a complete view of circulation throughout the entire domain. Although drifter data provide detailed information on movement over time and space, researchers often use it not only to study trajectories but also to reconstruct Eulerian velocity fields. Numerous studies have employed drifter observations for this purpose [10–12].

To overcome the limitations of drifting in-situ instruments, high-frequency (HF) radar systems have become an increasingly valuable tool for near real-time monitoring of surface currents and for validating ocean circulation models [13, 14]. HF radar provides broad spatial coverage of surface currents, typically interpreted in the Eulerian framework, and primarily senses the upper meter of the ocean [15]. These systems are particularly suited for coastal regions, encompassing areas from a few kilometers to over 200 kilometers offshore, and can operate under nearly all weather conditions due to their ability to propagate radio waves beyond the horizon [15]. HF radar data have proven especially useful in time-sensitive scenarios such as Search and Rescue (SAR) operations and oil spill response [16]. However, a single HF radar station only captures the radial component of surface flow, either toward or away from the antenna. As such, combining data from at least two stations is necessary to reconstruct full vector current fields [17]. Despite their numerous advantages, high-frequency (HF) radar systems also come with notable limitations. They typically operate within shallow coastal waters, are prone to radio interference, offer limited spatial resolution, and demand significant infrastructure and maintenance efforts.

These observational measurements are often combined with or compared to Acoustic Doppler Current Profilers (ADCPs), which provide an additional in-situ approach for measuring flow velocities by capturing vertical profiles from surface to bottom using the Doppler shift principle, as demonstrated in multiple studies [18, 19]. Unlike surface drifters, ADCPs deliver continuous measurements throughout the water column, offering detailed mapping of flow structure

[20]. They can be deployed from vessels, moorings, or autonomous platforms, providing high temporal resolution and complementing both drifter and HF radar observations, particularly for understanding vertical shear and validating numerical models.

To address the inherent limitations of traditional in-situ methods, satellite altimetry has emerged as a powerful tool, offering broader spatial coverage and additional insights into surface flow dynamics. Since the early 1990s, radar altimeters on satellites, which look directly downward, have provided near-global observations of the ocean surface, offering coverage that HF radar systems cannot offer. Rather than measuring surface currents directly, these satellites estimate them indirectly by first measuring Absolute Dynamic Topography (ADT) along one-dimensional tracks. The data are then interpolated into two-dimensional ADT maps, from which surface velocities are derived using the geostrophic approximation [21]. This approximation, which relates sea surface height (SSH) gradients to ocean surface velocity, is widely accepted for resolving large-scale circulation. This is because geostrophic flow dominates ocean dynamics on spatial scales larger than approximately 10 km and over timescales longer than a few days [22]. However, despite its utility, this method has inherent limitations. Due to the coarse spatial and temporal sampling of ADT and the assumptions underlying the geostrophic balance, satellite altimetry primarily captures mesoscale dynamics, on the order of 100 km and 10 days [21]. As a result, it struggles to resolve finer sub-mesoscale motions, which are essential for capturing detailed advection and energy exchange processes [23].

While satellite altimetry has greatly advanced the ability to monitor broad oceanic flows, its reliance on the geostrophic approximation leaves a gap in observing smaller, faster, or unbalanced motions. These include common processes in dynamic coastal zones and within energetic eddies, which play a key role in sub-mesoscale dynamics. This gap poses a fundamental limitation when it comes to accurately simulating near-surface advection, where finer-scale variability can have a substantial impact [21].

2.1.2 Reconstruction techniques

To overcome the limitations of sparse observational data and assumptions inherent in geostrophic approximations, various computational techniques have been developed for reconstructing sea surface velocity fields. These range from classical interpolation schemes to advanced data assimilation and machine learning methods [24, 25]. More recently, hybrid approaches combining

physical constraints with data-driven models have shown promise in improving reconstruction accuracy [26, 27].

2.1.2.1 Spatial interpolation methods

Reconstructing continuous velocity fields from scattered measurements, such as those collected by GPS drifters, remains one of the central challenges in oceanography. Because ocean currents are often sampled at irregular locations and times, researchers rely on interpolation techniques to estimate flow conditions across unsampled areas. A wide range of methods has been explored, from straightforward geometric approaches to more advanced statistical and physics-informed techniques [28].

For scalar fields like sea surface temperature or elevation, methods such as Inverse Distance Weighting (IDW) and Ordinary Kriging (OK) are commonly used [29, 30]. However, vector fields like ocean currents pose additional challenges, as they involve both direction and magnitude. In these cases, Radial Basis Function (RBF) interpolation methods, especially those designed to be divergence-free, thereby preserving the incompressibility of ocean flow, have shown promising results [31–33]. Such methods have demonstrated improved accuracy in reconstructing realistic coastal circulation patterns from sparse data [34].

While simple geometric methods are computationally efficient, they often struggle to capture complex flow features, especially in dynamic regions with sharp gradients or rapidly changing directions. Kinematic interpolation techniques, which take into account the movement behavior of particles, tend to perform better under such conditions [35, 36]. Furthermore, methods that incorporate temporal dynamics, such as spatio-temporal kriging, can improve reconstructions by leveraging flow evolution patterns over time. However, these approaches often require more computational resources and careful tuning. Robust handling of measurement noise and missing data remains an ongoing challenge.

Recently, machine learning-based interpolation models have emerged as a compelling alternative [37, 38]. By learning spatial and temporal patterns from large datasets, they can potentially offer more accurate reconstructions, though they require substantial amounts of training data and computational power to be effective [39]. The trade-off between computational cost and reconstruction quality remains a key consideration, especially for large-scale or real-time applications.

2.1.2.2 Data Assimilation

While spatial interpolation techniques estimate flow fields using scattered observations alone, Data Assimilation (DA) methods improve these reconstructions by optimally combining observational data with dynamical ocean models. DA effectively merges real-world measurements and model forecasts to provide a more accurate and comprehensive representation of the ocean's current state [24]. By weighting information based on the uncertainties of both data sources, DA corrects errors and fills in gaps, leading to enhanced estimates of key variables such as current velocity, salinity, and temperature.

Among the advanced DA techniques, methods like Four-Dimensional Variational Assimilation (4D-Var) and the Ensemble Kalman Filter (EnKF) have become prominent in recent research [24]. While 4D-Var is known for producing smooth and dynamically consistent results, it tends to be computationally demanding. On the other hand, lighter-weight methods such as Ensemble Optimal Interpolation (EnOI) can offer practical alternatives with less computational cost, though sometimes at the expense of some accuracy or detail [40]. Despite their potential, applying DA effectively remains a complex task as it depends heavily on having high-quality observational data, precise models, and sufficient computing power, especially when working with fine-scale, high-resolution ocean simulations [41].

2.1.2.3 Machine Learning and Hybrid approaches

To overcome the limitations of both spatial interpolation and DA, recent research has increasingly explored machine learning (ML) techniques as a complementary or alternative approach for predicting flow fields [42]. For instance, artificial neural networks (ANNs) have been employed to learn spatio-temporal patterns from drifter trajectories, leading to improved long-term trajectory prediction and reduced modeling errors [43, 44]. Beyond trajectory analysis, deep learning (DL) techniques have also been employed to construct surrogate models of fluid flows [45, 46], allowing rapid and efficient flow predictions while avoiding the computational cost of conventional fluid dynamics simulations. The accessibility of ML algorithms has driven their growing use in oceanography, for tasks ranging from estimating chlorophyll concentration to reconstructing three-dimensional ocean structure and surface current fields [47]. Convolutional Neural Networks (CNNs) have been widely used to increase the resolution of gridded ocean datasets, by learning spatial patterns and reconstructing fine-scale velocity structures while respecting geostrophic balance [48, 49].

However, ML models still face well-known challenges: they tend to overfit to training data, struggle with novel or anomalous conditions (known as "distribution shift") [50], and are often criticized as "black boxes" because the decision-making process can be difficult to interpret. Nevertheless, ML offers strong potential for classification, regression, anomaly detection, and integration of diverse data streams through self-supervised and hybrid physics-informed learning [26]. Therefore, the combination of spatial interpolation, data assimilation, and machine learning is leading to a major change in modeling ocean surface velocities. Since each method has its own challenges, a shift is being made away from relying solely on traditional physics-based models toward more flexible, hybrid data-driven frameworks. Interpolation needs sufficient number of data points, data assimilation can be heavy on computation, and machine learning sometimes doesn't perform well outside its training conditions. However, when these approaches are used together, they can fill in each other's weaknesses. For instance, machine learning is increasingly becoming part of data assimilation processes to improve forecast accuracy. Meanwhile, physics-informed neural networks help preserve important physical principles in the models [51, 52].

This integration reflects the reality of modern oceanography's big data era, characterized by the collection of vast datasets from diverse sources such as satellites, autonomous underwater vehicles, and drifters. Effectively processing and assimilating this extensive data demands advanced analytical tools, with the added challenge of maintaining transparency and trustworthiness in such enhanced models, especially for critical applications like search and rescue operations [53].

To provide an overview of sea surface velocity reconstruction methods, Table 2.1 compares commonly used observation platforms with advanced techniques. It highlights the main strengths and limitations of each approach, including traditional methods such as drifters and HF radar, as well as modern methods like data assimilation, machine learning, and hybrid models that integrate physical and data-driven components.

Table 2.1: Overview of observation platforms and reconstruction techniques for sea surface velocity estimation.

Method	Cost	Spatial coverage	Temporal resolution	Accuracy
Drifters	Low	Point measurements	High	Medium
HF Radar	High	Coastal	High	High
ADCP	Medium-High	Vertical profiles	High	High
Satellite Altimetry	High	Near-global	Low	Medium
Spatial Interpolation	Low	Sparse data	Moderate	Medium
Data Assimilation	High	Observation density	High	High
Machine Learning	Medium-High	Training data	High	Medium-High
Hybrid (ML + DA)	High	Obtained data	High	High

As shown in Table 2.1, different observation platforms provide direct measurements with varying cost, coverage, and resolution. Reconstruction techniques complement these observations by estimating velocity fields where measurements are sparse. Spatial interpolation is simple and low-cost but less accurate in complex flows, while data assimilation and machine learning can capture detailed flow structures and fill gaps but require accurate models, large datasets, or high computational resources.

2.2 Advection and transport modeling at the sea surface

The ability to accurately reconstruct sea surface flows is key to simulating how passive scalars, representing concentration fields of pollutants or nutrients, or probability densities of debris and objects, spread over time. These transport processes are governed by the combined effects of advection and diffusion, which determine how a scalar like concentration (s) changes in space and time without affecting the fluid’s velocity or pressure. This makes passive scalar modeling particularly useful for studying mixing and dispersion in environmental and engineering flows [54].

Mathematically, this behavior is described by the advection-diffusion equation. The non-conservative (advective) form of this equation is often used for its clarity in separating the effects of advection and diffusion:

$$\frac{\partial s}{\partial t} + \mathbf{u} \cdot \nabla s = D \cdot \nabla^2 s + R - \gamma \cdot s. \quad (2.1)$$

Here, s represents a passive scalar, also referred to as a tracer, describing a concentration or probability density in the domain. The term $\frac{\partial s}{\partial t}$ represents the temporal change in scalar concentration at a fixed location, while $\mathbf{u} \cdot \nabla s$ describes its transport by the surrounding flow field

u. The term $D\nabla^2 s$ captures the gradual spreading caused by diffusion, with D denoting the diffusion coefficient. R accounts for any sources introducing tracer or sinks removing it, while $\gamma \cdot s$ represents decay, which models continuous loss of scalar proportional to its concentration (e.g. evaporation, degradation) [55].

At the ocean surface, these combined processes interact with wind-driven currents, swirling eddies, and small-scale turbulence, while also being influenced by changes in depth and tidal variations, resulting in complex and often unpredictable transport pathways. Capturing these dynamics through modeling is challenging, largely because they span multiple scales and involve nonlinear interactions. To tackle this complexity, researchers rely on various theoretical frameworks and computational strategies to approximate the flow field and simulate how tracers like pollutants or nutrients disperse over time, as discussed in [56].

Two of the most commonly used approaches are the Lagrangian and Eulerian frameworks. These methods adopt fundamentally different perspectives: the Lagrangian approach tracks individual particles, whereas the Eulerian approach focuses on changes occurring at fixed locations. Each approach has its own strengths, and often they are combined to provide a more comprehensive understanding.

2.2.1 Lagrangian vs. Eulerian approaches

The Lagrangian approach describes fluid motion from the perspective of fluid particles moving with the flow [57]. In this framework, large numbers of virtual particles are embedded in three-dimensional, time-evolving ocean velocity fields. This method is particularly powerful for analyzing pathways, understanding connectivity between regions, and investigating the origin of water masses through reverse-time analysis [57]. Lagrangian analysis is well-suited for handling transport barriers, including eddies and currents, which substantially impact dispersal patterns. It can also yield accurate results in turbulent or complex geometric flow fields by directly simulating particle movement [58]. However, the Lagrangian approach can be computationally demanding, especially for large scales, and the resulting complex and unpredictable paths of individual particles can be more difficult to analyze compared to other oceanographic techniques.

In contrast, the Eulerian approach describes fluid motion from a fixed point in space, focusing on the changes in fluid properties (i.e. tracer concentration) at specific locations over time [58]. For fast, first-order estimates of particle transport and dispersion, particularly in

environments like vegetated coastal zones, a simplified Eulerian approach is often the more practical and cost-effective option compared to Lagrangian models, which tend to require more detailed input data and greater computational resources [59]. Eulerian models are well adapted for capturing large-scale concentration changes, but they generally offer less insight into individual particle trajectories and may struggle to represent the full complexity of fine-scale, unpredictable movements that Lagrangian methods are designed to resolve [58].

To improve model accuracy and make better use of Lagrangian observations, researchers have explored methods to incorporate such data into predictive frameworks. One approach estimates velocities by tracking changes in observed positions over time and then adjusts the model predictions accordingly [60]. Another approach uses an observational operator derived from the particle advection equation to improve the Eulerian velocity field by minimizing discrepancies between observed and simulated trajectories [61]. Early studies [62] demonstrated that using basic Euler methods in non-uniform flow fields can produce substantial trajectory errors. Consequently, modern pollution prediction models often employ more physically grounded techniques, remaining within an Eulerian framework while calculating slick thickness with layer-averaged Navier–Stokes equations and modeling pollutant transport through the advection–diffusion equation [63].

The decision between using a Lagrangian or Eulerian framework largely depends on the specific objectives of the study and the resources available. In many cases, the two are used together, as their strengths are complementary. For example, Eulerian models can supply the velocity fields needed for Lagrangian particle tracking, providing a more complete picture of ocean transport processes.

2.2.2 Computational models

Computational models represent numerical or mathematical approaches for simulating ocean dynamics and particle transport. These models vary widely in complexity, from large-scale circulation simulations to simplified stochastic or particle-tracking approaches, each addressing different research needs.

Numerical ocean models: Large-scale ocean circulation models, such as ROMS (Regional Ocean Modeling System) [64], HYCOM (Hybrid Coordinate Ocean Model) [65], and NEMO (Nucleus for European Modelling of the Ocean) [66], simulate the key physical processes that govern currents, temperature, and salinity across spatial and temporal scales. These velocity

fields form the backbone for most transport simulations. To maintain reliability, such models require continuous updates through data assimilation, blending real-time measurements with physical constraints. Techniques like 4D-Var are vital for improving the accuracy of short-term forecasts and capturing dynamic features like eddies [40].

Lagrangian particle tracking: These models are designed to simulate the motion of virtual particles through ocean velocity fields, making them well adapted for studying connectivity, dispersal, and biophysical interactions [57]. While tracking on structured model grids is computationally efficient, many coastal ocean applications use unstructured grids to balance nearshore resolution with offshore efficiency. Historically, particle tracking on unstructured meshes has been slower, limiting the number of particles and behaviors modeled [67]. However, tools like OceanTracker (OT) have greatly improved computational efficiency. They include innovations such as the Short Triangle Walk (STW) method and interpolation weight reuse, which enable simulation of millions of particle trajectories on unstructured grids at speeds often two orders of magnitude faster than earlier approaches [67].

Stochastic models: Particle transport in the ocean is affected not only by the main flow but also by diffusion and unresolved subgrid-scale processes. These are typically modeled using stochastic terms added to particle trajectories via stochastic differential equations (SDEs) [57]. Such approaches are particularly useful for representing eddy-driven transport and sharp tracer gradients while avoiding numerical artifacts like negative concentrations [57]. Choosing when and how to incorporate stochastic terms remains an open question and depends on factors such as resolution and flow complexity.

Beyond these foundational modeling strategies, recent research highlights the complexity and unpredictability of passive scalar transport in dynamic ocean environments. For example, [68] examined how deterministic flows impact the probability density function (PDF) of passive scalars, emphasizing the challenges of predicting scalar decay in turbulent systems. Similarly, [69] explored how chaotic advection generates localized ‘hot spots’ in boundary layers, underscoring the sensitivity of scalar transport to fine-scale structures. These findings illustrate that even in seemingly stable conditions, complex internal dynamics can strongly influence tracer dispersion.

In practical applications, modeling scalar transport often serves urgent societal needs, such as tracking pollutants, predicting harmful algal blooms, or guiding search and rescue operations. For instance, [70] proposed reduced-order stochastic models that efficiently approximate the

statistics of passive tracers in turbulent flows, enabling fast forecasts of extreme events. In disaster response scenarios, such as oil spills or locating individuals lost at sea, the ability to predict short-term drift patterns becomes critical. The work of [71] highlights the need for highly accurate short-term forecasts, especially under rapidly changing atmospheric conditions and sea states, including the influence of wind waves and their interaction with ocean currents.

Emerging applications are also expanding the role of transport modeling beyond traditional marine contexts. For example, [72] introduced a novel framework for autonomous search strategies in dynamic environments. Their approach uses an advection-diffusion-based global saliency map, where particles originating from visually salient regions are guided toward the robot's position.

Altogether, the continuous refinement of computational tools, from high-fidelity circulation models to efficient particle tracking and stochastic formulations, reflects a broader effort to accurately simulate the complex, multi-scale nature of ocean transport. Hybrid methods that combine the strengths of Eulerian and Lagrangian frameworks are increasingly used to capture both the broad-scale structure and fine-scale variability of oceanic flows [73].

2.3 Applications in Search and Rescue

The accuracy of transport modelling in marine SAR operations strongly depends on the quality of met-ocean forecast data used to predict object movement in the water [74]. For quick responses in a variety of changing conditions, SAR operators rely on several forecast products that deliver near-real-time ocean and wind data. Over time, different modeling methods have been proposed to improve the precision of predictions, where early approaches focused mainly on wind-driven drift models that account for specific object characteristics like shape, buoyancy, and how much wind they catch [75–77]. These models, known as leeway models, offer a simplified but practical way to estimate how objects drift in the water during operations.

More recent efforts focus on integrating high-resolution oceanographic data and numerical model outputs into ensemble-based prediction systems. These systems account for environmental uncertainty and sub-grid variability, which are especially critical in dynamically active coastal zones [78]. The use of ensemble trajectory modeling helps mitigate uncertainties in object initialization, forcing inputs, and small-scale ocean processes that are often not captured in

deterministic models [79, 80]. By simulating multiple plausible scenarios, ensemble approaches can yield more robust predictions and support probabilistic search strategies.

Operational transport forecasting increasingly benefits from the assimilation of near-real-time observational data, such as those from HF radar systems, ocean drifters, and satellite-derived wind and current products. These data sources improve the spatial and temporal resolution of input fields, enhancing model performance in short-term prediction horizons [74]. However, limitations in data coverage, particularly in remote or offshore regions, continue to present significant challenges to operational implementation [53].

Efforts to refine such modeling also include the incorporation of wave-induced motion and stochastic perturbations to simulate unresolved turbulence and variability [81, 82]. Probabilistic frameworks combining wind, current, and random motion components have shown potential to produce more realistic trajectories, particularly in high-variability environments. Still, performance remains sensitive to both object-specific characteristics and the accuracy of environmental inputs [83]. Complementary approaches have been proposed to augment trajectory models, including the use of Lagrangian Coherent Structures (LCS) to identify flow features that influence material transport. These methods can help define regions of convergence or separation in the flow, offering additional guidance for narrowing SAR search areas [84]. Such techniques are especially valuable when traditional trajectory predictions diverge or when direct object tracking is not available.

While advances in modeling and observation have significantly improved transport prediction capabilities, key limitations persist. The operational usability of models depends not only on their accuracy but also on their ability to integrate diverse data sources and deliver timely, interpretable output to SAR personnel [85]. Furthermore, large-scale and long-duration transport events, such as those involving aviation debris, reveal the influence of broad ocean circulation patterns and highlight the need for multi-scale modeling approaches [86].

Overall, the progression from deterministic wind-transport models to sophisticated ensemble-based systems reflects a broader shift toward coupling physical realism with probabilistic analysis. Continued research into submesoscale dynamics, object characterization, and hybrid observational-modeling frameworks remains essential to further advance SAR effectiveness [87–89].

3 TECHNOLOGY OF SEA SURFACE VELOCITY MEASUREMENTS

Every sea surface velocity reconstruction requires the acquisition of velocity measurements. The quality and reliability of the reconstruction are directly influenced by the characteristics of these measurements, specifically their accuracy, spatial resolution, temporal resolution, and total amount of measurements. The resolution and precision of the obtained data determine the level of detail that can be resolved in the resulting flow field, while a wider spatial distribution helps reduce uncertainty in areas far from measurement points. The time available for data processing, the method of measurement (e.g., drifters, HF radar, remote sensing), and the speed at which the measurements are obtained all play critical roles in shaping the final reconstruction. In real-world scenarios, these factors are often constrained by logistical and operational limitations, requiring a balance between measurement density and timeliness. Therefore, the effectiveness of any reconstruction method depends not only on the methods employed but also on the quality, configuration, and interpretation of the collected velocity data.

3.1 Floating sensors

One of the most popular and cost-effective ways to gather sea surface velocity data is through satellite tracking of drifting sensors, commonly known as drifters. Over the last twenty years, their use has expanded significantly, with deployments spread across diverse ocean regions [5]. These floating instruments are specifically designed to record surface current information, and their data have been the focus of extensive research and numerous analyses [6, 7].

While GPS is commonly used for positioning, modern drifters are often equipped with additional sensors that can measure salinity, temperature, pressure, and other relevant parameters, providing improved insight into sea conditions. Such drifters rely primarily on satellite communication for data transmission, where the most widely used communications are Argos and Iridium. A comparison of their performance, including the advantages of the newer Argos-3 system relative to Iridium, is presented in [90]. In contrast, when velocity measurements are

collected over smaller spatial domains, data transfer can also be achieved using terrestrial communication technologies such as General Packet Radio Service (GPRS) or Very High Frequency (VHF) systems.

However, thanks to their ability to move freely with the currents, their trajectories are naturally uncontrolled, which can cause them to drift far beyond the intended monitoring areas. This characteristic presents both an advantage and a limitation: while it allows for the capture of natural Lagrangian paths, it also means that coverage can become spatially uneven and unpredictable.

As illustrated in Figure 3.1, drifters come in various designs, reflecting differences in instrumentation, energy sources, and communication technologies. These variations allow them to be adapted for specific environments or research objectives.



Figure 3.1: Examples of surface drifters used in oceanographic studies. Different models are optimized for various applications and primarily differ in their communication and data transmission capabilities [91–94].

One of the key factors to consider is the number of available measurements. A larger drifter deployment can improve spatial coverage and data resolution, but practical constraints such as cost, deployment logistics, and maintenance limit the number of devices that can be used at one time [81, 82]. Furthermore, the precision of onboard sensors and the accuracy of position measurements also influence the quality of the data collected.

A significant advancement in obtaining reliable Lagrangian velocity time series was achieved by attaching a sea anchor, or drogue, to drifters. A variety of drogue shapes and designs exist,

each optimized for specific measurement objectives. Some of the designs can be seen in Figure 3.2.

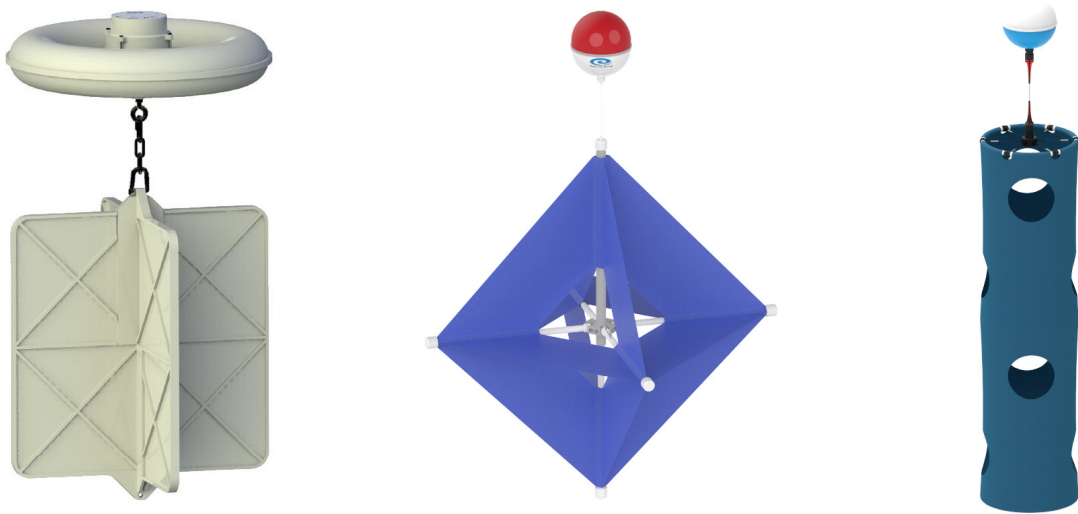


Figure 3.2: Different types of drogues, constructed from various materials and designed for different deployment conditions [95].

These drogues stabilize the instrument by minimizing the influence of wind and waves, allowing the drifter to follow the water movement more accurately. The choice of drogue depends on the measurement objectives, drifter design, and environmental conditions. Larger or high-drag drogues are used to minimize wind influence and accurately track water motion, especially in rough seas or deeper layers, while smaller drogues are mostly used for near-surface currents in calm conditions [95]. Material and durability also influence the selection to ensure stability and reliable measurements over time.

Despite their value, it is important to recognize that drifter data represent discrete, point-based measurements. As a result, while they offer critical insight into localized flow dynamics, they cannot provide a complete, continuous map of circulation patterns over an entire area on their own. Combining drifter data with other observational methods, such as HF radars and satellite measurements, is often necessary to build a more comprehensive understanding of sea surface velocities [53, 78, 85].

3.2 High-Frequency (HF) radar systems

In situations where long-term monitoring of surface currents within a fixed coastal area is needed, HF radar systems offer clear advantages over drifting sensors. Unlike drifters, which

move with the flow and can quickly leave the area of interest, HF radar provides continuous measurements over a defined, stationary region. This makes it an ideal solution for observing dynamic changes in coastal circulation patterns over time without the risk of losing coverage due to sensor drift.

In general, HF radar operates by emitting electromagnetic waves that interact with the ocean surface and reflect back information about current velocities. This happens through the analysis of Doppler shifts in radio waves backscattered by surface gravity waves, a phenomenon known as Bragg scattering [96]. These systems provide near-real-time data with broad spatial coverage, often measuring currents over the upper meter of the ocean, making them especially useful for operational oceanography and model validation [13]. For instance, assimilation of HF radar data into numerical models has been shown to improve the accuracy of current predictions, especially in regions with complex circulation where other measurement methods may struggle [14]. An example of an HF radar system is visible in Figure 3.3.



Figure 3.3: Great Lakes Observing System HF radar providing live snapshots of lake surface currents, 24 hours a day [97].

HF radar systems can cover large coastal regions, as their wide coverage is enabled by the propagation of radio waves beyond the visible horizon through the “ground wave” effect over conductive seawater [98]. One limitation is that a single HF radar site only measures the component of flow directly toward or away from that site (radial velocity). To obtain a full vector of surface currents, data from at least two sites with a suitable angle (typically between 30° and 150°) must be combined [17]. This is needed to overcome the so-called “baseline problem” and accurately estimate flow direction and speed. Additionally, the effective range can be reduced by radio interference, high sea states, or poor ground conductivity near receiving antennas (i.e., dry rocky terrain that weakens the signal) [17]. It is also important to note that HF radar measurements represent an integrated flow over a shallow depth rather than a single point measurement, requiring careful interpretation [96].

Installing and operating HF radar systems comes with logistical challenges. They require coastal installation sites with suitable terrain, infrastructure, and an unobstructed view of the ocean surface. Because these systems are fixed installations, they lack portability, which may leave some coastal regions unmonitored due to geographic or logistical constraints. They provide high-resolution two-dimensional surface current maps, with spatial resolution from several hundred meters to a few kilometers and temporal resolution from tens of minutes to about one hour. However, they cannot capture vertical flow structures and are sensitive to electromagnetic interference, weather conditions, and noise from nearby infrastructure.

Despite these limitations, HF radar remains one of the most efficient and reliable tools for maintaining consistent, long-duration surface current observations over specific coastal zones. Its ability to monitor large areas continuously without deploying sensors directly into the water makes it a valuable complement to drifters and other mobile platforms.

3.3 Satellite-based surface velocity measurements

When it comes to observing sea surface velocities over vast or remote areas, satellite-based measurements offer a powerful and unmatched advantage, which is global reach. Satellites can cover regions that are difficult or impossible to access with ships, radars, or drifters, and they do so on a regular basis. This makes satellite data especially appealing for large-scale monitoring efforts, where having at least some level of observation across wide spatial domains is more valuable than high-resolution, localized measurements [99, 100].

One of the greatest strengths of satellite systems is that they do not require any deployment or maintenance on the ocean surface. With a single satellite pass, it becomes possible to gather data from areas thousands of kilometers away, including open oceans and politically sensitive or environmentally protected zones. This passive, wide-area access opens the door to comprehensive mapping of oceanic features like eddies, large-scale currents, or even seasonal circulation patterns [101, 102].

However, this convenience comes with significant trade-offs. A key limitation lies in spatial resolution. While some satellites can provide measurements at a scale of about 1 km, many standard products offer coarser resolutions as reported in [102]. This may be sufficient for detecting broad circulation trends, but if the goal is to understand finer details, such as currents near the coastline or around small islands where dynamics occur at scales of tens of meters, then satellite data quickly becomes inadequate [100]. Therefore, when a satellite provides only one data point per square kilometer, it is unable to capture sub-kilometer-scale features that may be crucial for navigation, search and rescue, or pollution tracking [103].

Temporal resolution presents another constraint. In many cases, surface velocity estimates derived from satellite imagery or altimetry are only available every few days or even weekly, depending on satellite orbits. Additionally, this approach is also limited by the inability to acquire data during cloudy conditions, which can create significant gaps in monitoring fast-evolving events such as short-lived eddies or storm-driven currents [101, 104].

Accessing high-resolution satellite data can also come at a cost. While many datasets are freely available, finer spatial and temporal products often generated by commercial satellites may require paid access or subscriptions [105]. Even after obtaining the data, the process of transforming raw satellite observations into usable velocity fields is not straightforward. It involves complex data processing, including atmospheric correction, image interpretation, and often the integration of multiple data sources like sea surface height, ocean color, and sea surface temperature [99, 106]. Without proper algorithms, experience, or computing resources, turning satellite data into meaningful current estimates can be slow and error-prone. Additionally, data usage permissions and latency can be a limiting factor in operational scenarios. Some datasets may be restricted due to national security or commercial licensing, and delays in data delivery can reduce their value for real-time applications [102].

3.4 Measurement uncertainty

When comparing how accurately different methods measure surface currents, it’s important to look at their uncertainties and how often they collect data, as shown in Table 3.1. Drifters can provide very accurate point-based measurements, with low uncertainty and frequent sampling, making them ideal for tracking water movement at specific locations. However, their spatial coverage is limited since they only provide point measurements, and because they move freely with the currents, they can drift away from the area of interest. In contrast, HF radars cover extensive coastal regions with good spatial and temporal resolution, though their accuracy can fluctuate, with root-mean-square-error (RMSE) sometimes reaching up to 16 cm/s. Satellite altimetry typically delivers lower uncertainty over open-ocean areas, but its coarser spatial and temporal resolution makes it less suitable for capturing short-term or small-scale changes.

Table 3.1: Measurement characteristics of surface current data collection methods, including resolution and uncertainty ranges.

Instrument	Spatial Resolution	Temporal Resolution	Uncertainty / RMSE	Reference
Drifters	Point measurement	5 min	RMSE up to 1.9 cm/s	[107, 108]
HF radar	200 m - 12 km grid	10-60 min	RMSE up to 16 cm/s	[109, 110]
Satellite altimetry	25-100 km	7-10 days	RMSE up to 12 cm/s	[22, 111]

Overall, each method has trade-offs: drifters excel in precision at specific points, HF radar balances coverage and frequency nearshore, and satellite altimetry provides broader, less frequent snapshots of surface currents.

3.5 Effective number of measurements

Reconstruction accuracy of the surface flow field depends not only on the amount of available measurements but also on how they are distributed within the domain. Although increasing the number of measurements generally improves the stability and accuracy of the reconstruction by providing more data, this improvement is not always guaranteed. When velocity measurements are placed too closely together, they tend to capture redundant information about the flow field. In such cases, the contribution of each additional measurement becomes negligible. To better assess the scope of measurement placement, the authors of [112] proposed the concept of the effective number of measurement points, denoted as η . This represents the number of points that provide unique and valuable information for the reconstruction of surface flows. Importantly, η is based on the criterion of uniform distribution of measurements across the observed area.

Such an approach is particularly relevant for drifters, as other measurement systems typically sample on a predefined uniform grid.

The influence area of a single measurement point \mathbf{m}_i is estimated using a 2D Gaussian function:

$$\Phi_i(\mathbf{x}) = \frac{1}{2\pi\sigma^2} \exp\left(-\frac{(\mathbf{x} - \mathbf{m}_i)^T \cdot (\mathbf{x} - \mathbf{m}_i)}{2\sigma^2}\right), \quad (3.1)$$

where σ is the standard deviation, while $\frac{1}{2\pi\sigma^2}$ presents the scaling factor which ensures that the total volume under the Gaussian curve equals 1, regardless of the value of σ .

The objective is to cover the domain with n_{MP} measurement points such that, ideally, each point covers a circular area with a radius of three standard deviations, capturing approximately 99.7% of the volume under Φ . Assuming all measurement points have equal influence (i.e., σ is the same for all i), in the ideal case, the total influence of all measurement points is equal to the area of the domain Ω :

$$9\sigma^2 \cdot \pi \cdot n_{MP} = |\Omega|. \quad (3.2)$$

From (3.2), the value of σ can be directly calculated. Once the measurement point locations and the corresponding standard deviation σ are known, the Gaussian influence function can be evaluated around each measurement point within the domain. If some measurements are placed close to one another, their influence regions will overlap.

To quantify the effective influence of the measurement locations, the maximum value of the combined influence functions at each point in the domain is used. The *effective number of measurement points*, denoted by η , is then defined as:

$$\eta = \int_{\Omega} \max(\Phi_1(\mathbf{x}), \Phi_2(\mathbf{x}), \dots, \Phi_{n_{MP}}(\mathbf{x})) d\mathbf{x}. \quad (3.3)$$

The resulting η is expected to be a positive real number, bounded by the total number of measurement points ($1 \leq \eta \leq n_{MP}$). For an ideal configuration where all measurement points contribute unique information, η approaches n_{MP} . A visual illustration of the concept of *effective number of measurement points* is provided in Figure 3.4.

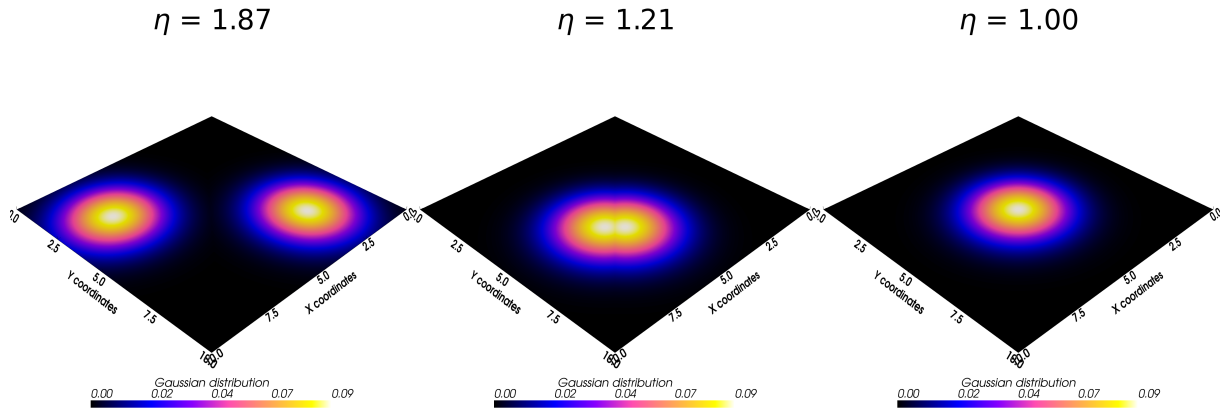


Figure 3.4: Illustration of the effective number of measurement points η .

As illustrated in Figure 3.4, the measurement points on the figure's left side are well spaced, with each covering a distinct portion of the domain. However, due to the rectangular shape, some corners remain uncovered, so the effective number η is slightly less than the total number of measurement points n_{MP} . In the middle part, the points are clustered too closely, causing their reach areas to overlap and resulting in redundant information. Consequently, η is much lower than n_{MP} . On the right side, as an illustrative example, two measurement points overlap and provide identical information. In this case, the effective number reduces to $\eta = 1$, even though $n_{MP} = 2$.

To illustrate the impact of measurement point placement in a realistic coastal domain, Figure 3.5 shows two configurations of 15 measurement points within a domain featuring a complex coastline and an inlet-outlet boundary. Although the total number of points is the same, the effective number of measurements η differs depending on their spatial distribution.

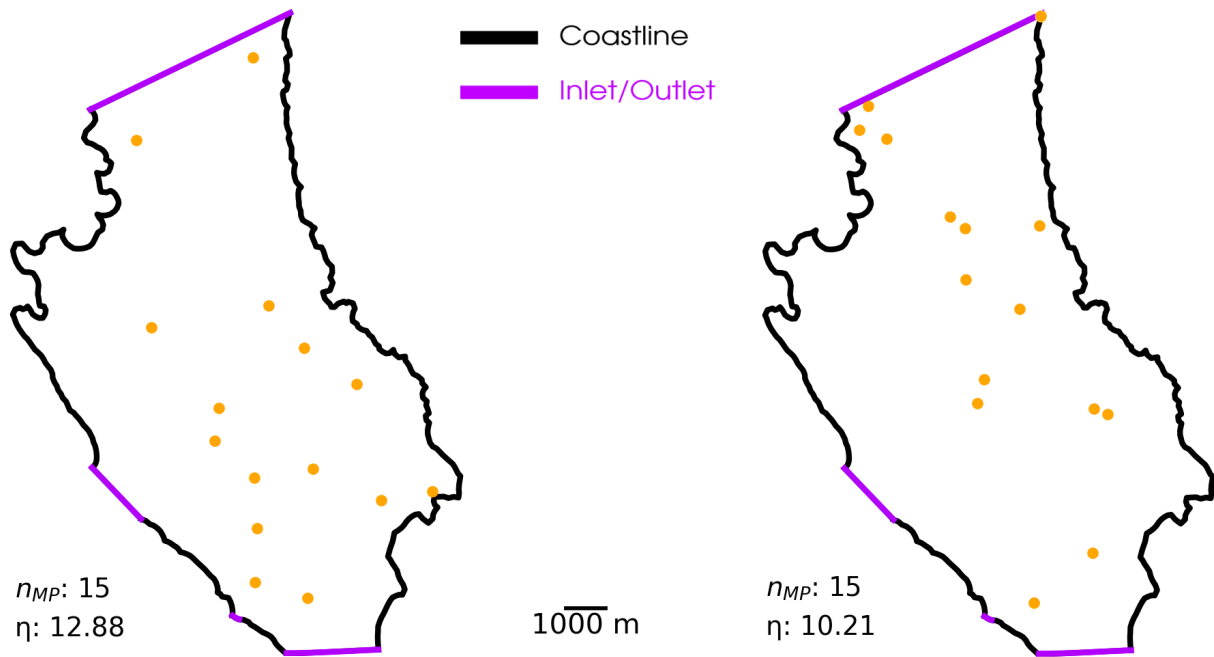


Figure 3.5: Example of measurement point configurations in a coastal domain with different effective number of measurements η .

In the left configuration, the points are well spaced, resulting in $\eta = 12.88$, which indicates minimal redundancy. In contrast, the right configuration contains several closely spaced measurement points, reducing the effective number of measurements to $\eta = 10.21$ due to overlapping areas. This example highlights how clustering of measurement points can decrease reach efficiency and overall information yield, motivating the use of the proposed concept, η , in the analyses of the following chapters.

4 DYNAMICS OF SEA SURFACE DRIFT

Operational ocean forecasting is primarily concerned with predicting key hydrodynamic variables, such as sea level, temperature, salinity, and ocean currents. While these parameters are fundamental for describing the physical state of the ocean, the broader interest often lies in their practical implications. One particularly relevant application is the transport of floating objects or substances, commonly referred to as drift [88]. From maritime safety and pollution control to search and rescue efforts, understanding how materials move across the sea surface represents a critical link between ocean dynamics and real-world decision-making.

Sea surface drift is governed by a wide range of environmental processes that interact in complex, often nonlinear ways. These environmental influences are tightly interconnected and work across a wide range of spatial and time scales, where changing one can propagate through the entire system. For example, large-scale climate systems can shift wind and temperature patterns, which then impact local wave generation and current dynamics. At the same time, small-scale turbulence, wave breaking, and interactions with shorelines further complicate the movement of drifting objects, especially near coasts.

This multiscale aspect makes it inherently difficult to model sea surface drift in a cohesive way. The complexity means that predicting drift accurately requires factoring in many interacting variables at once. However, creating and running detailed models that capture all relevant processes, from global to local scales, demands a lot of computational time and resources. Even with the use of modern supercomputers, addressing all aspects of sea surface drift for either operational or research purposes remains a significant challenge.

4.1 Drift of floating objects

Historically, knowledge of surface ocean circulation has often been inferred from the observed drift of floating objects. The movement of these objects across the ocean surface is driven by a complex combination of forces. Ocean currents, wind stress, and wave motion all act on the

object's surface, while internal forces like gravity and buoyancy influence its center of mass [88]. Together, these factors determine the object's overall trajectory.

Mathematically, the drift velocity of an object, denoted as \mathbf{u}_{drift} , can be expressed as the sum of the ocean current velocity \mathbf{u}_{curr} and the object's motion relative to the water \mathbf{u}_{rel} :

$$\mathbf{u}_{drift} = \mathbf{u}_{curr} + \mathbf{u}_{rel}. \quad (4.1)$$

Here, \mathbf{u}_{curr} typically includes contributions from various processes such as baroclinic circulation, tidal and inertial currents, wind-driven Ekman flow, and the wave-induced Stokes drift [88]. This component is usually assumed to affect all floating objects similarly and is often derived from numerical ocean models, wind parameterizations, or in situ measurements.

The relative component \mathbf{u}_{rel} , on the other hand, is highly dependent on the object's properties, including its shape, size, buoyancy, and how much of it is exposed above the water. This term reflects the wind and wave forces acting directly on the object and often varies significantly between different types of debris or vessels.

As a result, modeling the drift of objects has been a longstanding research challenge. Early approaches, such as the Leeway method introduced in [75], provided practical frameworks for estimating drift by incorporating empirical relationships between wind forcing and object motion. However, these models rely on simplifications and can struggle to account for real-world complexities such as irregular object shapes, variable sea states, or uncertain object characteristics.

The drift behavior of both human survivors and man-made objects ranging from life rafts and shipping containers to various types of marine debris has been extensively studied, particularly in the context of SAR by [75, 76], as well as more recent advances in modeling uncertainty and wind-wave-object interactions [82, 83, 86, 89]. Despite progress, predicting the precise path of drifting objects remains difficult in practice due to the stochastic nature of environmental forcing and the diversity in object geometries.

4.2 Influence of object shape and environmental factors

The types of objects involved in operational contexts such as SAR, ship drift prediction, and hazardous material (HAZMAT) tracking span a wide range of shapes and sizes, from small debris such as life jackets or broken containers to large vessels. Regardless of size, an object's

drift is often characterized by its leeway motion. A comprehensive review by [75] categorized 63 object types relevant to SAR planning, providing empirical values for leeway speed and divergence angle. From these values, leeway coefficients are derived to quantify the motion of drifting objects relative to ambient water as a function of wind speed, typically decomposed into downwind and crosswind components. These coefficients were later expressed as functional relationships in [76] and remain widely used in operational SAR tools. More recent studies, such as [77], expanded these models to incorporate wind drag, wave effects, and uncertainty estimates, improving the robustness and realism of modern drift forecasts [81].

The influence of object shape is not limited to rigid bodies. Oil spills, for example, represent a dynamic class of drifting objects with evolving physical characteristics. Depending on their source, oil spills from vessels or leaks at drilling sites behave quite differently, spreading across the surface, changing in thickness, and partially mixing into the underlying water [113]. While smaller spills from routine ship operations are frequent and contribute substantially to global marine pollution, it is the large-scale events that cause the most severe environmental damage. In most countries, oil spill response, including drift forecasting, is a coordinated government-administered service.

In both SAR and HAZMAT contexts, an object's exposure to wind and shape-dependent drag determines how much it deviates from the current-driven path. Streamlined or submerged objects tend to follow ocean currents closely, whereas objects with large above-water profiles are more influenced by wind. Consequently, object trajectories can diverge significantly over time, especially under variable environmental conditions.

This complexity is not just a technical issue, as it shows the real difficulty of forecasting movement in a constantly changing marine environment. Models need to balance physical realism with practical feasibility, which often leads to trade-offs between resolution, accuracy, and speed. Given these challenges, it is clear that traditional modeling methods alone are not always sufficient. They often need simplifications that reduce realism, or they require computing power that is not easily accessible. This creates a growing need for alternative, more efficient strategies like surrogate modeling, which provides a practical way to overcome the limitations of traditional methods, allowing for more efficient and thorough analyses.

5 SURROGATE MODELING OF SEA SURFACE DYNAMICS

Simulating how the ocean changes over time can be very demanding, due to multiple factors. Fully resolving all relevant physical phenomena requires very complex mathematical models, which demand significant computing power and long simulation times. Additionally, many necessary inputs, such as precise geometry, boundary conditions, wind forcing, and other environmental parameters, are often unavailable as either constant or transient data, further complicating accurate modeling. High-fidelity simulations are also not well suited for data assimilation based on drifter measurements, as they are computationally too expensive for real-time updates. Moreover, the necessity of super-precise simulations is questionable, since even highly detailed models may not realistically capture drifter trajectories or small-scale flow variability. These limitations motivate the development of surrogate models, which provide sufficient approximations of sea surface dynamics while remaining computationally feasible. Accordingly, this thesis adopts a surrogate-based approach employing a steady-state, incompressible flow model. This simplifies the physical setup by excluding dynamic influences like wind, tides, waves, and temperature fluctuations in the initial stage. Instead of fully resolving these effects, the surrogate model focuses on estimating the drift velocity, \mathbf{u}_{drift} , rather than the full current velocity, \mathbf{u}_{curr} . A secondary fusion model can later be applied to provide greater flexibility in accounting for additional influences, without explicitly including the full physics of wind, waves, or tides.

The proposed approach combines two simplified two-dimensional surrogate models: one for the realistic coastal region with inlet/outlet boundaries, and another circular open-domain model to represent the broader offshore influence. Each domain is computed separately before being fused (added), creating a hybrid solution capable of capturing submesoscale flow behavior and passive scalar transport, such as pollution or drifting objects.

By avoiding the need for dense measurement data, complex domain setups, and full transient simulations, this approach greatly improves computational efficiency. CFD simulations still provide physically meaningful flow fields, while the fusion of surrogates makes it possible to

reflect wider hydrodynamic behavior with low computational cost. This makes the model ideal for scenarios that require fast yet reliable drift velocity predictions, particularly in time-sensitive applications like emergency response or real-time tracking.

5.1 Steady 2D flow model

A steady-state, incompressible flow model is defined over a two-dimensional domain $\Omega \subset \mathbb{R}^2$. The flow is governed by the steady incompressible Navier-Stokes equations [114–116]:

$$\rho(\mathbf{u} \cdot \nabla)\mathbf{u} = -\nabla p + \mu \nabla^2 \mathbf{u} + \rho \mathbf{f} \quad (5.1)$$

$$\nabla \cdot \mathbf{u} = 0, \quad (5.2)$$

where \mathbf{u} is the velocity vector, p is the dynamic pressure, ρ the fluid density, μ the dynamic viscosity, and \mathbf{f} represents external forces. The assumption of incompressibility implies that the density ρ is constant.

As the approach focuses on two-dimensional surface flows, vertical dynamics are not resolved explicitly. Instead, hydrostatic balance is assumed and pressure at the surface is represented only by the dynamic component as introduced in [117]. This assumption is typical in surface-flow modeling but may limit reliability where different layers and pressure variations impact horizontal transport. To realistically simulate interactions between the modeled region and the surrounding sea, boundary conditions in the form of tangential velocity components and pressure values are applied. These are not assigned arbitrarily, rather, they are chosen within physically realistic ranges to reflect plausible ocean dynamics and tuned to the measurements as described in the next chapters.

In submesoscale regions of the Adriatic Sea, which serves as the primary area of interest, surface currents exhibit significant variability due to the interaction between mesoscale structures and smaller-scale processes. Based on HF radar, numerical studies, and satellite imagery, surface velocities vary from less than 0.1 m/s to more than 0.5 m/s [118–120], with typical values within the range of 0.1–0.2 m/s. Faster currents, occasionally surpassing 1.0 m/s, are observed in high-flow regions such as the Strait of Otranto [121], but this study is primarily concerned with calmer, semi-enclosed coastal basins.

The flow model is formulated as pressure-driven, making it suitable for situations where the domain boundaries are known but it is uncertain which segments function as inlets or outlets. In this setup, inlet and outlet conditions are not prescribed in advance but are implicitly determined during the solution. Specifically, zero-gradient conditions are applied at outlet boundaries, while inlet velocities are inferred from fluxes in the patch-normal direction. This requires specifying the tangential velocity \mathbf{u}_t and total pressure p_0 along the boundary. The dynamic pressure is then calculated depending on whether the boundary behaves as an inlet or outlet:

$$p = \begin{cases} p_0 & \text{for outlet,} \\ p_0 + 0.5\rho|\mathbf{u}|^2 & \text{for inlet.} \end{cases} \quad (5.3)$$

Assigned tangential velocity and total pressure are interpolated smoothly along the open-sea boundaries while enforcing zero values at boundary endpoints. This boundary condition setup allows for flexibility in the placement and strength of inlet and outlet regions, while maintaining a robust and consistent solution. These profiles are iteratively adjusted until the resulting flow field closely matches the point velocity measurements. The parametrization of boundary conditions is described in detail in the following chapters.

5.2 Fusion model

The fusion framework combines two steady-state incompressible flows, each defined over a specific domain with its own boundary conditions. The bounded domain is tailored to a realistic area of interest and includes features such as coastlines and inlets/outlets. This is enclosed by an open, fully circular region that encompasses the bounded domain and accounts for broader environmental influences. Flow fields for each domain are computed separately and then combined, enabling the flexibility of simplified two-dimensional surrogate to better capture real-world variability. This concept is illustrated in Figure 5.1, where a synthetic scenario called Simple bay case is used to demonstrate the workflow applied to a representative domain.

To account for external conditions, the open domain employs four control points (contributing eight variables to the optimization vector) that influence the background flow. The velocity field fusion is achieved by extracting the velocity values at each node within the bounded domain, retrieving corresponding values from the open domain, and summing them point-wise:

$$\mathbf{u}_{fused} = \mathbf{u}_{bounded} + \mathbf{u}_{open}, \quad (5.4)$$

where $\mathbf{u}_{bounded}$ and \mathbf{u}_{open} denote the velocity fields from the bounded and open domains, respectively.

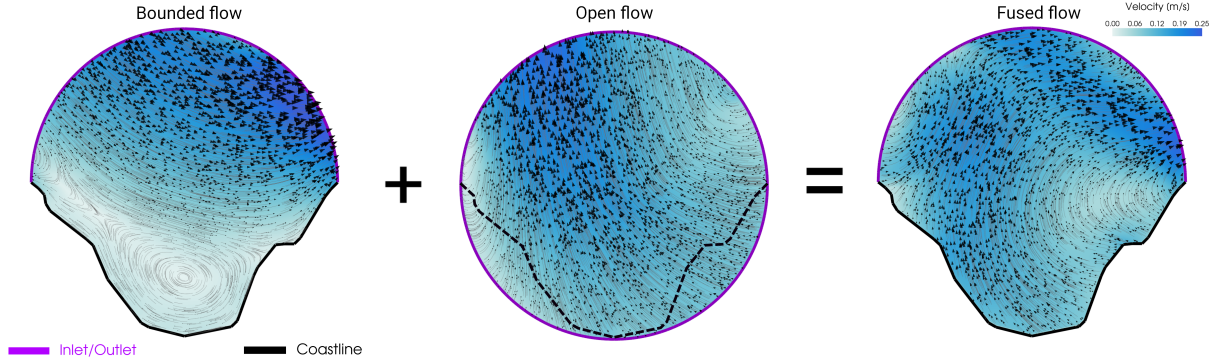


Figure 5.1: Illustration of the fusion model methodology. The bounded domain, shown on the left, incorporates coastlines and represents the primary area of interest. The open domain, depicted in the middle, encloses the bounded domain and reflects broader environmental conditions. The fused velocity field, obtained by superimposing the two simulations, is displayed on the right. In the overlapping region, velocity values from both domains are interpolated and summed at each grid point.

By fusing these velocity fields, the model delivers a more comprehensive and responsive representation of surface flow dynamics. In practical marine scenarios, unusual flow patterns, such as currents seemingly originating from land, have been documented in high-frequency radar studies [16, 122, 123]. Such patterns cannot be accurately captured using conventional two-dimensional CFD methods, which are not capable of representing complex three-dimensional coastal effects. Since the methodology focuses on reconstructing surface flow from observational data, the fusion model is deliberately designed to capture both typical and atypical patterns observed in measurements. This adaptability enables real-time updates of the flow field, significantly improving the fidelity of passive scalar reconstruction. By incorporating dynamic environmental influences, the model offers a more accurate representation of real-world coastal and marine conditions.

5.3 Transient flow estimation

Fully transient flow simulations are computationally demanding, often requiring very small time steps and fine spatial resolution to capture rapid variations accurately. This makes them challenging to apply in real-time scenarios, particularly when high-resolution meshes or large domains are involved. Such limitations are well documented in studies employing the open-source toolkit OpenFOAM [124]. To overcome this challenge, the transient flow is approximated using a quasi-steady approach, in which a sequence of steady flow reconstructions represents the temporal evolution of the flow.

The quasi-steady approximation relies on the observation that many oceanic flows evolve gradually rather than abruptly, allowing them to be considered approximately steady over short time intervals. The flow field is updated at regular intervals, denoted T_s , at which measurements are obtained. The choice of T_s is based on the expected timescale of flow variations and the frequency of available measurements, ensuring that each interval is short enough to resolve significant changes but long enough to maintain computational efficiency. The impact of different T_s values on flow reconstruction accuracy and efficiency is analyzed in the results section.

The strategy for reconstructing passive scalar advection and diffusion assumes that the flow remains approximately steady within short time intervals. The scalar is transported and spread according to the flow field reconstructed at the time of the measurements. Since the scalar field evolution is highly sensitive to the flow field, small inaccuracies can accumulate over time, but with frequent measurement updates these deviations are progressively corrected. As long as measurement updates are frequent enough, this allows us to simulate the evolving flow effectively by piecing together a series of steady states.

This framework offers a range of advantages. By combining a series of quasi-steady states, it effectively captures the evolution of transient flows while avoiding the substantial computational cost associated with fully time-dependent simulations. It naturally represents gradual changes in the flow, providing a realistic approximation of the evolving dynamics. The method allows the flow field to be updated continuously as new measurements become available, ensuring that deviations from the true state are progressively corrected. Moreover, it enables a clear assessment of how measurement frequency and spatial coverage influence the accuracy of the reconstruction. This combination of efficiency, adaptability, and informative output makes the framework well-suited for operational oceanography, environmental monitoring, pollutant tracking, and other scenarios where timely and reliable flow estimates are essential.

5.4 Numerical implementation

The governing equations of fluid motion are complex, non-linear partial differential equations. In many scientific and engineering problems, finding exact solutions is difficult or impossible. Computational fluid dynamics (CFD) addresses this by discretizing these equations into algebraic forms that can be solved numerically.

5.4.1 Governing Equations of Fluid Flow

Fluid motion follows the basic conservation laws of mass, momentum, and energy. These laws are expressed mathematically as partial differential equations. They form the basis of fluid dynamics and explain how fluids act and change over time [125, 126]. A key assumption in this field is the continuum hypothesis. This idea suggests that fluids can be viewed as continuous media, ignoring their separate molecular nature [126, 127]. This perspective allows us to treat physical properties like velocity (\mathbf{u}), pressure (p), density (ρ), temperature (T), and viscosity (μ) as smoothly changing field variables at every point within the computational area [128]. This hypothesis holds true for most engineering applications dealt with in CFD.

The thesis adopts the Eulerian perspective for modelling the flow, focusing on fixed spatial locations to observe changes in fluid properties as the fluid passes through them, rather than tracking individual fluid particles as in the Lagrangian approach. A key concept in this formulation is the control volume (CV). This is a specific area in space where conservation laws apply [126]. The general conservation principle for a quantity ϕ within a control volume V surrounded by surface S is shown by the integral equation:

$$\frac{\partial}{\partial t} \int_V \rho \phi dV + \int_S \rho \phi (\mathbf{u} \cdot \mathbf{n}) dS = \int_S \Gamma_\phi (\nabla \phi \cdot \mathbf{n}) dS + \int_V S_\phi dV, \quad (2.1)$$

where t denotes time, \mathbf{n} is the surface normal vector, Γ_ϕ is the diffusion coefficient, and S_ϕ represents a source or sink term.

5.4.1.1 Conservation of Mass

The principle of mass conservation dictates that the mass within a CV can only change due to the net flow of mass across its boundaries. For a fixed control volume, the integral form of the mass conservation equation is derived from the general conservation equation by setting the

property $\phi = 1$, with a diffusion coefficient $\Gamma_\phi = 0$ and no source terms $S_\phi = 0$. This results in:

$$\frac{\partial}{\partial t} \int_V \rho dV + \int_S \rho(\mathbf{u} \cdot \mathbf{n}) dS = 0. \quad (5.5)$$

The term $\rho(\mathbf{u} \cdot \mathbf{n})$ represents the mass flux through the control volume boundary. Applying the divergence theorem to the surface integral yields the differential form of the mass conservation equation:

$$\frac{\partial \rho}{\partial t} + \nabla \cdot (\rho \mathbf{u}) = 0. \quad (5.6)$$

This equation is applicable to both compressible and incompressible flows. For incompressible flow, where the material derivative of density (ρ) is zero, the continuity equation simplifies to:

$$\nabla \cdot \mathbf{u} = 0. \quad (5.7)$$

5.4.1.2 Conservation of Momentum

The law of momentum conservation is essentially an application of Newton's second law to fluids [125, 126]. It states that the rate at which a fluid particle's momentum changes is equal to the net force acting upon it. These forces can be categorized into surface forces, such as pressure and viscous forces, and body forces, like gravity [125, 126]. By setting $\phi = \mathbf{u}$ in the general control volume equation, the integral form of the momentum conservation equation is derived:

$$\frac{d}{dt} \int_V \rho \mathbf{u} dV + \int_S \rho \mathbf{u}(\mathbf{u} \cdot \mathbf{n}) dS = \int_S \boldsymbol{\sigma} \cdot \mathbf{n} dS + \int_V \rho \mathbf{g} dV + \int_V \mathbf{f} dV, \quad (5.8)$$

where $\boldsymbol{\sigma}$ is the stress tensor, \mathbf{g} represents gravitational acceleration, and \mathbf{f} denotes other body forces acting per unit volume.

The left side of the equation describes the rate of change of momentum within a control volume, including both local time variations and momentum transported by the flow itself. On the right side, the terms represent the forces acting on the fluid: surface forces expressed through the stress tensor acting on the control volume boundaries, and body forces such as gravity and other external influences distributed throughout the fluid. The differential form, obtained by applying the divergence theorem, results in:

$$\frac{\partial(\rho\mathbf{u})}{\partial t} + \nabla \cdot (\rho\mathbf{u} \otimes \mathbf{u}) = -\nabla p + \nabla \cdot \boldsymbol{\tau} + \rho\mathbf{g} + \mathbf{f}. \quad (5.9)$$

Here, $\rho\mathbf{u}$ is the momentum density, $\rho\mathbf{u} \otimes \mathbf{u}$ represents the convective momentum flux, p is the static pressure, $\boldsymbol{\tau}$ is the viscous stress tensor, $\rho\mathbf{g}$ denotes gravitational body forces, and \mathbf{f} represents other body forces per unit volume [129, 130].

For an incompressible Newtonian fluid with constant dynamic viscosity μ , the viscous stress tensor simplifies to:

$$\boldsymbol{\tau} = \mu (\nabla\mathbf{u} + (\nabla\mathbf{u})^T), \quad (5.10)$$

where \mathbf{u} is the velocity vector and $(\cdot)^T$ denotes the transpose.

Using this, the Navier-Stokes equation can be written in simplified form as:

$$\rho \frac{\partial\mathbf{u}}{\partial t} + \rho(\mathbf{u} \cdot \nabla)\mathbf{u} = -\nabla p + \mu \nabla^2\mathbf{u}, \quad (5.11)$$

where ρ is the fluid density, p the pressure, and μ the dynamic viscosity. The gravitational term $\rho\mathbf{g}$ and other body forces \mathbf{f} are omitted here, as they are not applied in the present study.

The difficulty in solving the Navier-Stokes equations largely stems from the nonlinear convective term, $\mathbf{u} \cdot \nabla\mathbf{u}$, which causes interaction between velocity components and leads to complex flow features such as turbulence and vortices [127].

5.4.1.3 Conservation of Energy

The fluid energy conservation equation, derived from the first law of thermodynamics, accounts for convection, heat conduction, work performed by surface forces (pressure and viscous stresses), and heat addition from body forces or internal sources [131]. By substituting $\phi = E$ (total energy per unit mass) into the general control volume equation and including appropriate source terms, the differential form of the energy equation is obtained:

$$\begin{aligned} \frac{d}{dt} \int_V \rho E dV + \int_S \rho E (\mathbf{u} \cdot \mathbf{n}) dS = & - \int_S p (\mathbf{u} \cdot \mathbf{n}) dS + \int_S (\boldsymbol{\tau} \cdot \mathbf{u}) \cdot \mathbf{n} dS \\ & - \int_S \mathbf{q} \cdot \mathbf{n} dS + \int_V \rho (\mathbf{g} \cdot \mathbf{u}) dV + \int_V \dot{Q} dV. \end{aligned} \quad (5.12)$$

In this equation, $E = e + \frac{1}{2}|\mathbf{u}|^2$, where e is the internal energy, \mathbf{q} is the heat flux vector, and \dot{Q} represents internal heat sinks or sources. By applying the divergence theorem to convert surface integrals into volume integrals, the differential form of the energy equation becomes:

$$\frac{\partial(\rho E)}{\partial t} + \nabla \cdot (\rho E \mathbf{u}) = -\nabla \cdot (p \mathbf{u}) + \nabla \cdot (\boldsymbol{\tau} \cdot \mathbf{u}) - \nabla \cdot \mathbf{q} + \rho(\mathbf{g} \cdot \mathbf{u}) + \dot{Q}. \quad (5.13)$$

5.4.2 Principles of the Finite Volume Method

Numerical discretization approximates continuous derivatives and integrals in the governing equations at a limited number of points or over finite volumes within the computational domain [126, 127]. In the Finite Volume Method (FVM), the computational domain is divided into a finite number of non-overlapping control volumes or cells. The integral forms of the conservation laws are applied directly to these cells [126].

A key feature of FVM is local conservation. The flux leaving one control volume through a shared face is exactly equal in amount and opposite in direction to the flux entering the adjacent volume. This ensures global conservation of quantities such as mass, momentum, and energy, regardless of mesh resolution [132, 133]. The general semi-discrete form of the FVM for a scalar quantity s in cell i can be expressed as:

$$\Delta V_i \frac{ds_i}{dt} = \sum_f F_f + R_i, \quad (5.14)$$

where ΔV_i is the volume of cell i , F_f represents the flux through face f of the cell (which may depend nonlinearly on the state of neighboring cells), and R_i accounts for source terms within the cell. This formulation shows that the time rate of change of s in a cell is governed by the net flux through its faces and any internal or external sources. Upon discretization in both space and time, these equations are transformed. For a scalar s , the resulting fully discrete form is:

$$\frac{ds_P^{(t+1)}}{dt} = a_P s_P^{(t)} + \sum_N a_N s_N^{(t)} + R, \quad (5.15)$$

where s_P^{t+1} is the value at the center of cell P at the new time step, s_N^t are the neighboring cell values, a_P and a_N are coefficients derived from flux and source term discretization, and R accounts for contributions from sources and boundary conditions.

This conservation property remains valid regardless of mesh resolution, making the FVM robust and reliable even on coarse grids.

5.4.3 Turbulence

Turbulence is a chaotic regime of fluid motion characterized by irregular velocity and pressure fluctuations, in contrast to the smooth and orderly behavior of laminar flow [126]. The shift from laminar to turbulent conditions typically occurs near a critical Reynolds number, where turbulence may intermittently appear within an otherwise laminar flow. This transition is highly sensitive to factors such as surface roughness, background turbulence, pressure gradients, and geometric features that promote instabilities. Once established, turbulence is inherently unsteady, three-dimensional, and rotational, spanning a broad range of time and length scales that make its exact prediction virtually impossible. Since resolving all turbulent motions with Direct Numerical Simulation (DNS) is computationally impractical for most applications, turbulence is generally modeled. Common strategies include Reynolds-averaged Navier-Stokes (RANS), which captures the averaged effects efficiently, and Large Eddy Simulation (LES), which resolves larger structures while modeling the smaller scales [126, 127].

In this thesis, turbulence is modeled using the k - ω *Shear Stress Transport* (SST) model [134], which integrates the benefits of the k - ω and k - ε models to improve the accuracy and stability of complex turbulent flow simulations. Using this approach, the computational domain is separated into near-wall regions and outer regions. Near the walls, a dedicated wall function is applied to effectively resolve turbulence behavior close to solid boundaries. In the free-stream outer region, the model operates as a k - ε model, providing stable and reliable results away from the wall [135]. In this thesis, the turbulence variables are initialized using:

$$k = \frac{3}{2}(|\mathbf{u}|I)^2, \quad (5.16)$$

$$\omega = \frac{k^{0.5}}{C_\mu^{0.25}L}. \quad (5.17)$$

Here, k denotes the turbulence kinetic energy, I the turbulence intensity, ω the specific dissipation rate, C_μ a model constant (set to 0.09), and L the turbulent length scale.

5.4.4 Numerical simulations in OpenFOAM

In this thesis, OpenFOAM was employed to numerically solve the governing equations using the Finite Volume Method (FVM). OpenFOAM is a C++ toolbox for computational continuum mechanics, providing core libraries for meshing, discretization, and turbulence modeling, along with application-specific solvers and utilities [136–138]. Several significant forks of OpenFOAM exist, including those from the OpenFOAM Foundation, ESI-OpenCFD, and the community-driven foam-extend project, which may differ in syntax and solver behavior [136, 139]. For the purposes of this thesis, OpenFOAMv2306 from ESI-OpenCFD was used.

OpenFOAM is built in a modular, object-oriented way, where core libraries handle tasks such as mesh operations, numerical calculations, linear solvers, and turbulence modeling. On top of these libraries, the software provides applications that make simulations easier to set up and run, divided into solvers and utilities:

- **Solvers:** Programs that solve specific types of flow problems, like:
 - `simpleFoam` for steady turbulent flows
 - `pisoFoam` for transient flows
 - `interFoam` for multiphase flows
- **Utilities:** Tools for preprocessing, postprocessing, and general case management, such as `blockMesh` (mesh generation), `mapFields` (field mapping between cases), `setFields` (initializing fields), and `foamToVTK` (exporting data for visualization)

A typical OpenFOAM project is organized into three main folders:

- **constant:** Contains data that usually remains unchanged, including:
 - Mesh in `polyMesh`
 - Dictionaries for material properties, e.g., `physicalProperties`, `momentumTransport`, `thermophysicalProperties`
 - Files for dynamic mesh operations, e.g., `dynamicMeshDict`
- **system:** Holds configuration files controlling the simulation, such as:
 - `controlDict` for overall execution

- `fvSchemes` for numerical discretization
 - `fvSolution` for solver settings, linear solvers, and relaxation factors
 - Additional optional dictionaries for parallel computing or specialized settings
- **time directories:** Store field data at different simulation times. The initial folder (usually `0`) defines starting and boundary conditions for all variables.

The typical workflow in OpenFOAM starts with creating the computational mesh, which can be generated using built-in tools like `blockMesh`, `snappyHexMesh`, `cfMesh` (in some OpenFOAM distributions), or imported from other sources. After the mesh is prepared, the physical properties of the fluid and case-specific parameters are defined within the `constant` folder. The initial state of the simulation, including boundary conditions and field values, is set in the `0` directory. Next, numerical schemes, solver options, and other runtime settings are specified in the `system` directory. Once the configuration is complete, the chosen solver is launched to perform the simulation.

In the context of scalar transport phenomena, OpenFOAM includes dedicated solvers such as `scalarTransportFoam`, which model the passive advection and diffusion of scalar quantities without influencing the underlying velocity field [136].

5.4.5 Boundary conditions

At the coastline, a no-slip condition (Dirichlet) is imposed on the velocity, ensuring that fluid motion vanishes at solid walls. For boundary faces where the fluid exits the domain, a Neumann condition is applied, allowing velocity to be extrapolated from the interior solution. On the open-sea boundary, where fluid enters the domain, a Dirichlet condition is used where velocity is determined from the prescribed flux in the direction normal to the boundary. Additionally, tangential velocity components are set to accommodate flow directions that are not perfectly perpendicular to the boundary, enabling a more realistic representation of rotational or oblique inflow.

At the open boundary, pressure is prescribed via a Dirichlet condition constrained to physically realistic values, while a Neumann condition is enforced along the coastline. To ensure numerical stability and resolve pressure gradients consistently, one internal reference cell is chosen and set to a fixed pressure of zero. The pressure field is then computed relative to this reference.

Initial estimates of turbulent kinetic energy and specific dissipation rate are obtained from (5.16) and (5.17), with appropriate wall functions applied at boundaries where required. Table 5.1 summarizes the boundary conditions applied for all test cases.

Table 5.1: An overview of the OpenFOAM boundary condition type employed in flow simulations for surrogate model.

Field	Inlet/Outlet	Coastline
u	pressureInletOutletVelocity	noSlip
p	totalPressure	zeroGradient
k	fixedValue	kqRWallFunction
ω	fixedValue	omegaWallFunction

To simulate quasi-steady flow conditions in this study, the `simpleFoam` solver from the OpenFOAM suite was employed, as it is designed for steady-state incompressible flow. Although the solver is inherently steady, a sequence of short, steady simulations was carried out to approximate transient-like behavior. The pressure–velocity coupling was handled using the SIMPLEC (SIMPLE-consistent) algorithm, a variation of the classic SIMPLE method originally proposed by [140]. This algorithm was controlled by setting a fixed number of iterations along with convergence criteria based on the residuals of velocity, pressure, and turbulence variables.

In terms of discretization, second-order accurate gradient and Laplacian schemes were applied to maintain solution accuracy, whereas first-order upwind schemes were used in regions with sharp gradients to ensure numerical stability, particularly for divergence terms related to convective transport. The `meshWave` method was used to compute wall distances required for turbulence modeling.

All simulations across test cases were configured using consistent boundary conditions and solver settings. For this pressure-driven flow, the initial conditions for velocity specified tangential velocity components using the `pressureInletOutletVelocity` boundary condition, along with total pressure, turbulent kinetic energy, and specific dissipation rate, while the internal field values were set to zero. The boundary conditions were specified in a non-uniform manner, with each boundary cell assigned a pair of values (u_t, p) representing the tangential velocity and total pressure, respectively. This treatment allows tangential velocity components to be prescribed, accounting for possible misalignment of the inflow with the inlet boundaries and providing more realistic conditions that capture swirl and tangential fluid motion.

Further implementation details, including grid structure, cell distribution, discretization schemes, and complete numerical setups for both bounded and open-domain cases, can be found in the repository on the Open Science Framework: <https://osf.io/wjsb2/>.

6 MODEL FITTING FRAMEWORK

The proposed methodology addresses a model fitting problem in which the objective is to match measured and simulated flow measurements. On one side, measurements provide velocity vectors at specific locations in the domain, while on the other, the numerical model simulates a flow field whose behavior can be adjusted by modifying the boundary conditions. The goal is to identify boundary values that yield a simulated flow matching the measurements as closely as possible at the measurement locations. This fitting problem is solved using an optimization algorithm, which iteratively updates the boundary values in order to minimize the error between the simulated and the referent flow.

To set boundary cell values, a user-defined number of control points is uniformly distributed along the boundary, with each point specifying a pair of (u_t, p) . Cubic spline interpolation is then applied to generate smooth velocity and pressure profiles across all boundary cells, ensuring continuity while allowing the boundary conditions to be controlled with a reduced number of variables. Because of this, the quality and fidelity of the flow reconstruction rely heavily on the optimization vector \mathbf{b} , which contains the tangential velocity and pressure values at the boundary control points:

$$\mathbf{b} = (\mathbf{u}_{t,1}, p_1, \dots, \mathbf{u}_{t,n_{CP}}, p_{n_{CP}})^T, \quad (6.1)$$

where n_{CP} stands for the number of boundary control points. An illustration of the velocity profile resulting from the components of the optimization vector can be seen in Figure 6.1.

To realistically represent surface flows and account for natural fluctuations in surface currents, especially at submesoscale levels, the bounds of the optimization variables were set between -0.5 and 0.5 m/s for tangential velocity, and between -0.05 and 0.05 m²/s² for pressure at the boundary points (in OpenFOAM for incompressible flow, pressure is expressed as p/ρ). These ranges were chosen to maintain computational stability, with initial candidates randomly placed within these limits. It should be noted that the final total pressure and tangential velocity values at the boundaries may slightly differ from the initially assigned ones, as they adjust

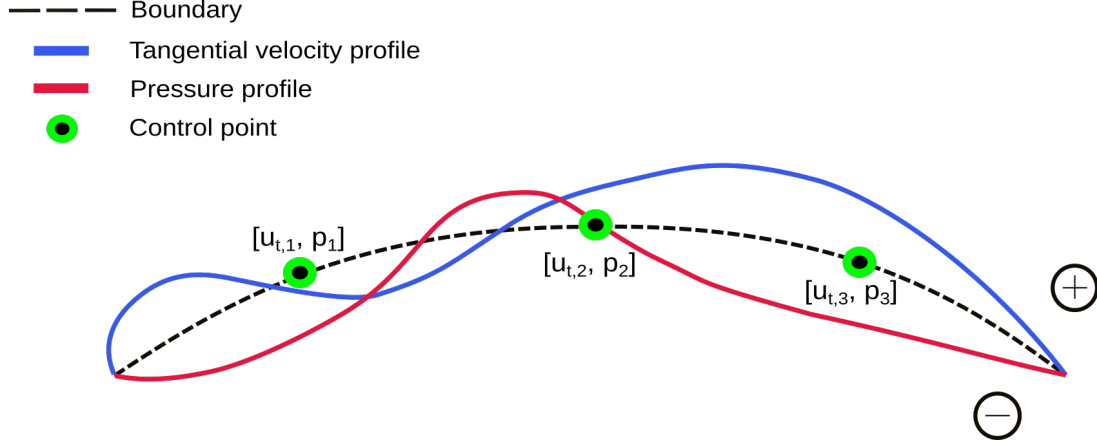


Figure 6.1: Figure depicts the parametrization of boundary conditions by placing control points along the boundary, each specifying a pair (u_t, p) , with cubic spline interpolation used to generate the tangential velocity and pressure profiles.

through through the solution of the Navier-Stokes equations in the domain.

6.1 Objectives

During each evaluation, a full OpenFOAM simulation is run to compute the velocity field across the entire domain. Velocity vectors are then extracted at measurement points corresponding to drifter positions and treated as referent data that the simulation aims to match. To measure how well the simulation matches these references, the cost function calculates the drifter error, E_d , defined as the root mean square of the velocity differences at these points (in meters per second). The optimization objective is to minimize E_d , ensuring the simulated velocities match the referent measurements as closely as possible:

$$\begin{aligned} \underset{\mathbf{b}}{\text{minimize}} \quad E_d(\mathbf{b}) &= \sqrt{\frac{1}{n_{MP}} \sum_{i=1}^{n_{MP}} (\mathbf{u}_{r,i} - \mathbf{u}_{s,i}(\mathbf{b}))^2} \\ \text{subject to} \quad \mathbf{b}_l &\leq \mathbf{b} \leq \mathbf{b}_u. \end{aligned} \quad (6.2)$$

Here, n_{MP} is the number of measurement points, $\mathbf{u}_{r,i}$ is the referent velocity, and $\mathbf{u}_{s,i}$ is the simulated velocity at measurement point location. This approach is presented on Figure 6.2).

To evaluate the quality of the reconstructed flow field, a global error measure, denoted as E_f , is additionally defined. This metric quantifies the overall discrepancy in the velocity field, analogous to (6.2). The velocity vectors at selected field points are considered solely for assessing

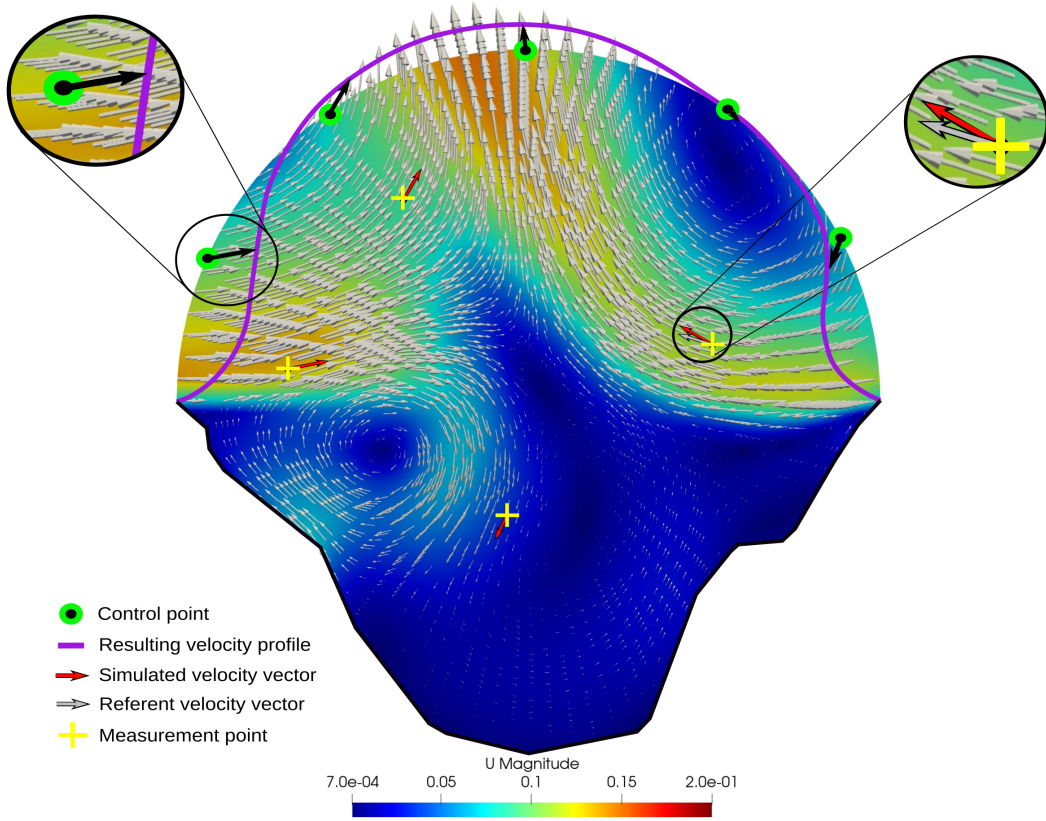


Figure 6.2: This figure illustrates the objective of adjusting the optimization variables at control points (green dots) until the red arrow (representing the current simulated velocity vector) aligns with the grey arrow (representing the referent velocity vector) for every measurement point (yellow cross).

the reconstruction performance and are not included in the optimization process:

$$E_f(\mathbf{b}) = \sqrt{\frac{1}{n_{FP}} \sum_{j=1}^{n_{FP}} (\mathbf{u}_{r,j} - \mathbf{u}_{s,j}(\mathbf{b}))^2}, \quad (6.3)$$

where n_{FP} is the total number of field points, $\mathbf{u}_{r,j}$ denotes the reference velocity vector, and $\mathbf{u}_{s,j}$ represents the simulated velocity vector at the field point location.

6.2 Constraints

To ensure the solutions found are feasible within this simulation-driven optimization, it is essential to enforce certain constraints. These constraints relate to simulation residuals and help steer the optimization toward solutions that are both accurate and numerically stable. Both simulation and optimization residuals are included in the optimization process and must remain

below the defined thresholds for the constraints to be considered satisfied; otherwise, penalties are applied.

The pressure residual constraint

$$r_p(\mathbf{b}) \leq 10^{-3}, \quad (6.4)$$

helps keep pressure values consistent throughout the optimization, avoiding unrealistic pressure imbalances. Velocity residuals, which guarantee physically plausible fluid behavior, are defined individually for each velocity component:

$$r_{u_x}(\mathbf{b}) \leq 10^{-4} \quad (6.5)$$

$$r_{u_y}(\mathbf{b}) \leq 10^{-4}. \quad (6.6)$$

The turbulent kinetic energy residual

$$r_k(\mathbf{b}) \leq 10^{-4}, \quad (6.7)$$

maintains the turbulence energy at acceptable levels. Likewise, the specific dissipation rate residual

$$r_\omega(\mathbf{b}) \leq 10^{-4}, \quad (6.8)$$

limits the turbulence dissipation rate to maintain physical accuracy.

Taken together, these constraints guide the optimization process, promoting stable, realistic, and physically meaningful fluid flow representations. All five constraints are checked for both bounded and open flow simulations, in a single optimization candidate \mathbf{b} evaluation.

6.3 Progressive field initialization and search narrowing

The optimization routine works by iteratively adjusting the values in the optimization vector to minimize the cost function. Initially, all cases begin with internal field values set to zero, while the boundary conditions vary according to each candidate solution. However, certain

combinations of boundary values can lead to slow or failed convergence, thereby extending the duration of the optimization.

Since the flow field is anticipated to vary only slightly between consecutive periods, the full range of optimization variable bounds is used only for the initial flow reconstruction. For all subsequent reconstructions, the bounds are narrowed to focus the search within 60% of initial range around the best solution for the previous quasi-steady time iteration, i.e:

$$\begin{aligned}\mathbf{b}_l^* &= \mathbf{b}_{opt} - 0.3(\mathbf{b}_u - \mathbf{b}_l) \\ \mathbf{b}_u^* &= \mathbf{b}_{opt} + 0.3(\mathbf{b}_u - \mathbf{b}_l),\end{aligned}\tag{6.9}$$

where, \mathbf{b}_l^* and \mathbf{b}_u^* are the updated lower and upper bounds, respectively. This reduction in search space focuses the optimization toward the most suitable parameter ranges in each period, enhancing convergence efficiency and reducing the computational cost of the fitting process.

To further accelerate convergence, a field initialization strategy is introduced, in which the internal field from the currently best-performing simulation is used as the starting point for new simulations. This approach is motivated by the observation that as optimization progresses, many candidates begin to resemble the best solution, resulting in similar flow fields. By initializing new simulations with a flow field already close to the expected final result, convergence can be achieved more rapidly, often in fewer iterations, leading to shorter simulation times. In practice, this method has been shown to reduce simulation time by up to 20%. While this improvement may not be noticeable for small domains or simulations that already converge quickly, it becomes particularly beneficial for larger domains with more complex flow dynamics. In such cases, convergence is more demanding, and the time savings are more substantial.

The effectiveness of this field initialization approach is demonstrated in Figure 6.3, which shows results from 300 pairs of optimization runs for the Simple bay test case. Each pair includes one run with field initialization and one without, using identical initial conditions, target flow fields, and randomly selected measurement points. The same optimization seed is applied to ensure a fair comparison. The figure clearly shows that field initialization leads to a reduction in computational time across iterations. While the advantage is minimal in early stages, after around 100 iterations, the time savings become significant, reaching up to 20%. Similar trends were observed in other test cases as well. These results show that, although the benefit is small during the early iterations, it increases over time, reaching up to 20% improvement by the 100th iteration.

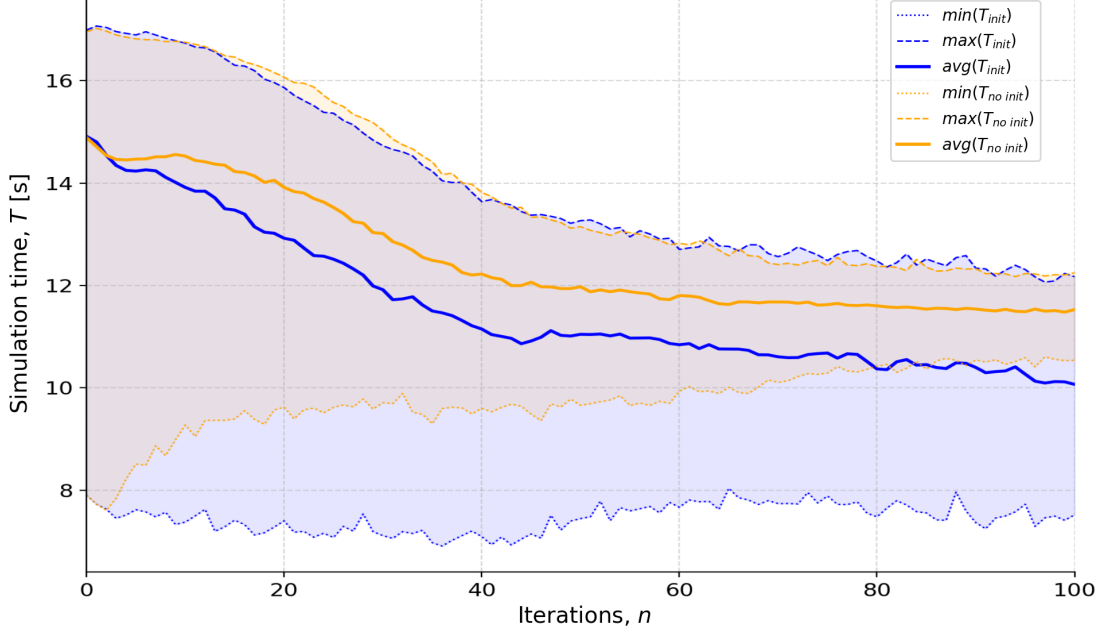


Figure 6.3: Computational improvements from using field initialization in simulations. Colored bands represent simulation durations per iteration, bounded by the average minimum and maximum run times. Dotted lines show the average minimum, and dashed lines indicate the average maximum simulation times.

6.4 Modeling drifter advection

In real-world conditions, drifters are carried by the currents across the domain while continuously emitting measurements. To simulate both their motion and the timing of measurement updates, a quasi-steady advection approach was used. In this approach, the reconstruction of the flow field is not controlled by a fixed number of optimization iterations. Instead, it runs within a predefined time limit T_s , corresponding to the expected interval between real-time measurement updates. This setup allows the system to regularly update the velocity field and trajectory predictions, assimilate new data as it becomes available, and treat the flow as steady within each update cycle. At each interval T_s , a drifter's displacement is computed based on the velocity field from the previous reconstruction, where the updated position is calculated using:

$$\frac{d\mathbf{x}}{dt} = \mathbf{u}(\mathbf{x}, t). \quad (6.10)$$

Here, $\mathbf{x}(t)$ denotes the position of a drifter at time t , and $\mathbf{u}(\mathbf{x}, t)$ is the velocity at that position and time. This ensures that simulated drifter positions evolve consistently with the reconstructed flow field, enabling their trajectories to be tracked over time. Over consecutive intervals, this produces a realistic and adaptive approximation of transient drifter behavior, supporting fast

and field-ready decision-making.

The approach of advecting drifter positions also provides an additional assessment of the accuracy of the reconstructed flow. This is achieved by calculating a positional error between the referent and simulated drifter locations, defined as

$$S(t) = \frac{1}{N} \sum_{i=1}^N \left\| \mathbf{x}_{referent}^{(i)}(t) - \mathbf{x}_{simulated}^{(i)}(t) \right\|, \quad (6.11)$$

which measures the deviation of the simulated drifter positions from their expected locations and provides an indication of how well the reconstructed velocity field reproduces the actual drifter motion. However, it should be noted that this was only used in the simulation framework. In real deployments, drifters naturally follow the currents, and no explicit advection of measurement points is needed.

This process of updating the velocity field in real time allows the system to keep accuracy in scalar transport modeling and meet the demands of operational time scales. Along with providing reliable performance, this ability supports the overall aim of the framework, which is designed to work as a useful decision-support tool that gives quick feedback. This responsiveness is particularly important in field operations where timely information can support operational choices and enhance the effectiveness of interventions.

7 ADVECTION DIFFUSION PROCESSES

A significant aspect of this work involves modeling the dispersion of pollutants, tracers, and hazardous materials that may be released into the marine environment, as well as modeling the dynamics of probability distribution in maritime SAR operations. These scenarios typically require methods that can simulate how substances evolve over time and space, often driven by ocean currents across broad domains. In such cases, the passive scalar transport framework based on the advection–diffusion equation is widely used due to its simplicity, adaptability, and effectiveness in rapid-response applications.

7.1 Passive scalar transport

A pollutant concentration, represented as a scalar field, evolves through advection by the surface velocity field, usually obtained from ocean circulation models. Since these substances are considered to have little or no influence on the flow itself and typically do not decay or react rapidly, this approach offers an efficient and reasonably accurate way to estimate how they spread. This simplification has been successful in various marine studies, including early models that tracked conservative tracers in large-scale ocean basins [141, 142].

The passive scalar approach plays a key role in many oceanographic and environmental applications. For instance, it forms the basis of biogeochemical and ecological models that monitor the distribution of nutrients and other tracers, transported by oceanic velocity fields and influenced by complex biological interactions [143, 144]. These models often rely on flow fields from hydrodynamic simulations, and to manage the high computational cost of simulating numerous tracers over large areas, efficient numerical techniques such as multigrid solvers have been developed [145]. Regional studies in the Mediterranean, for example, have combined passive advection with particle tracking to map plastic accumulation zones [146]. Similarly, high-resolution CFD tools have been employed to study microplastic dispersal in nearshore regions, where small-scale turbulence significantly impacts particle movement [147].

Here, the advection–diffusion equation introduced in Section 2.2, is adapted for a scalar field s advected by the fused velocity field \mathbf{u}_{fused} without source or sink terms which results in:

$$\frac{\partial s}{\partial t} + \mathbf{u}_{fused} \cdot \nabla s - D\nabla^2 s = 0. \quad (7.1)$$

While it does not resolve the exact shape or detailed dynamics of individual floating objects, it provides sufficiently accurate results for rapid decision-making and emergency response. For scenarios requiring greater physical detail, the framework can be extended to include effects such as turbulent diffusion, buoyancy, biofouling, decay, or reactive transport, allowing it to address a broad range of environmental modeling needs.

7.2 Assessment of passive scalar field advection accuracy

The reliability of passive scalar advection is evaluated by comparing advection-diffusion processes within a synthetic benchmark case. A simulated referent flow is used to generate a baseline passive scalar field, representing the ground truth for advection. The referent flow is inherently unsteady, and its dynamics are driven by time-varying boundary conditions. Evaluation of advection accuracy is only possible when the reference flow is known, as this setup allows assessment of whether the quasi-steady reconstructed flow provides an adequate approximation. Advection of the passive scalar field is then performed using the reconstructed flow, which is approximated by solving a series of steady-state flow fields at discrete intervals of T_s . The resulting scalar field is compared to the baseline to quantify reconstruction accuracy. Both scalar fields are initialized identically, and advection is simulated using the same numerical model and mesh to ensure a fair comparison. The only difference between the two simulations is the underlying velocity field.

To assess passive scalar field advection accuracy, two metrics are introduced. The first is the intersection metric, which quantifies how much of the referent scalar field overlaps with the reconstructed one. It is defined as:

$$I = \frac{\int_{\Omega_{intrsc}} s_{sim} d\Omega}{\int_{\Omega} s_{ref} d\Omega}, \quad (7.2)$$

where Ω_{intrsc} is the intersection region between the referent and simulated scalar fields, and s denotes the scalar values. An intersection value of 1 indicates perfect overlap, meaning the reconstructed flow accurately captures the referent advection. Lower values indicate increasing discrepancies due to reconstruction limitations.

The second metric is the coverage metric, which evaluates how well the simulated scalar field is encompassed by the referent field. This is particularly important in applications where it is crucial that the reconstructed scalar covers the region of possible presence of the target, similar to probability distributions. Even if the reconstruction is not perfectly accurate, ensuring that the simulated field includes the relevant area provides confidence that the target or phenomenon is captured. The coverage metric is therefore defined as:

$$C = \frac{\int_{\Omega_{intrsc}} s_{sim} d\Omega}{\int_{\Omega} s_{sim} d\Omega}, \quad (7.3)$$

where a value of 1 indicates that the referent field fully encompasses the simulated scalar distribution, while a lower value suggests that parts of the reconstructed scalar field deviate from the expected transport path under the referent flow. In practice, a slight overestimation of the covered area is acceptable if it ensures that the target remains within the reconstructed field. A visualization of the intersection region between the referent and simulated scalar fields, from which these metrics can be obtained, is presented in Figure 7.1.

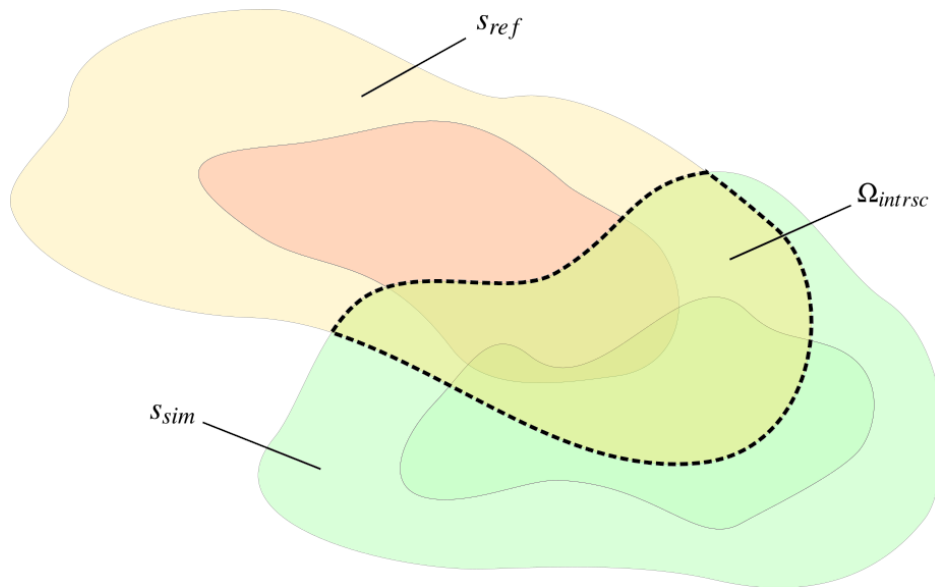


Figure 7.1: Visualization of the intersection between referent and simulated scalar fields, showing uncovered areas of referent scalar field and overestimated areas of the simulated scalar field.

7.3 Adaptive diffusion coefficient

To complement the coverage metric C and account for reconstruction errors in the velocity field, the diffusion coefficient is adjusted using the concept of mean squared displacement (MSD), denoted S^2 . The MSD is based on the drifter location error defined in (6.11) and provides a measure of the typical displacement caused by inaccuracies in the reconstructed flow. This adjustment increases the spread of the advected scalar, improving the possibility that the scalar field encompasses the target even when the reconstructed velocity field deviates from the referent flow. For a Brownian particle, the MSD is expressed as:

$$S^2(t) = 2 \cdot n_{dim} \cdot D \cdot t, \quad (7.4)$$

where $n_{dim} = 2$ is the number of spatial dimensions, D is the diffusion coefficient, and t is time. Here, the measured drifter positional error $S(t)$ from (6.11) can be used to estimate an effective diffusion coefficient for the passive scalar field, improving the possibility that the scalar field covers the relevant regions.

Therefore, an additional compensating diffusion term can be calculated as:

$$D_c = \frac{S^2}{4 \cdot T_s}. \quad (7.5)$$

Here, S^2 represents the average displacement caused by the error over the interval T_s . The compensating diffusion coefficient D_c accounts for the extra uncertainty introduced by the imperfect flow reconstruction. An adaptive diffusion coefficient is then defined for the reconstructed flow:

$$D_{adp} = D_{base} + D_c, \quad (7.6)$$

where D_{base} is the diffusion coefficient of the referent flow.

This adaptive diffusion approach ensures that the advected scalar field more reliably covers regions where the target is likely to be found, even in the presence of unavoidable inaccuracies arising from both measurements and flow reconstruction. By accounting for these uncertainties, D_{adp} enhances the robustness of scalar transport predictions and improves the overall reliability of the reconstruction for practical applications.

7.4 Application in dynamic search scenarios

Despite significant advances in marine technology, accidents at sea remain a serious challenge, keeping SAR operations essential. These efforts are inherently difficult due to the vast search areas and the constantly changing ocean conditions [53]. Time is one of the most critical factors in SAR, as survival rates drop rapidly with delays in finding missing persons.

Unmanned aerial vehicles (UAVs) have evolved into a viable solution for SAR [148, 149]. Path planning, multi-agent coordination, probability field generation, and dynamic target tracking are among the many topics examined. Work by [150], for instance, provides a technique for developing intelligent marine reaction plans, shown to be successful in actual contexts. Additionally, [151] dives deeply into the topic in his thorough investigation of target detection in maritime SAR aerial images and camera sensing systems. A dynamic probabilistic search algorithm is introduced in [148] to include Gaussian mixture models and fluctuating ocean current data. It employs grid-based spatial discretization, which is also found in the method outlined in [152]. Even if the target probability combines environmental data and sensor readings for path planning, its dynamic development is limited. Another example is presented in [153], where USVs were employed to carry out lawnmower-pattern searches, neglecting changes in the underlying probability domain.

A common objective in maritime SAR operations is to prioritize regions where the probability of locating a target is highest. Among the many methods developed for SAR, ergodic search strategies are particularly useful as they allow for precise exploration of areas based on complex and dynamically evolving probability fields. These methods ensure that the search trajectory statistically covers regions in proportion to their likelihood of containing the target. The most widely adopted ergodic search techniques include Model Predictive Control (MPC), Spectral Multiscale Coverage (SMC), and Heat Equation Driven Area Coverage (HEDAC). The SMC technique, originally introduced in [154], employs smoothed Fourier basis functions to generate trajectories that match the spatial distribution of target probability. Its adaptation for dynamic environments is discussed in [155], and further extended in [156] for the search of MH370, using Lagrangian particles to represent dynamic probabilities. MPC-based ergodic control, which frames trajectory generation as an optimization problem, is investigated in [157] and used for dynamic exploration and object detection tasks in [158]. Another promising method is HEDAC, initially proposed in [159]. Its FEM-based version has been shown to work on irregular domains and supports obstacle avoidance [160]. In addition to its spatial coverage capabilities,

the HEDAC framework was further extended to integrate probabilistic sensing, as discussed in [161]. However, its application to searching for drifting or dynamically behaving targets has not yet been demonstrated.

7.4.1 Dynamic probability distribution field

In real-world search scenarios, the domain is explored by multiple agents over the time interval t . These agents can represent unmanned aerial vehicles (UAVs), manned aircraft, or other search platforms, and the search is defined by their trajectories. It is assumed that the positions $\mathbf{z}_i(t)$ and orientations $\theta_i(t)$ of the agents are known, where $i = 1, \dots, n$ indexes the individual agents and n is the total number of agents involved in the exploration. The search process relies on the probability density $s(\mathbf{y}, t) : (\Omega \times t) \rightarrow \mathbb{R}$, which represents the likelihood of a target remaining undetected at position \mathbf{y} and time t . Its initial distribution, defined at $t = 0$, is given by $s_0(\mathbf{y})$ and satisfies the normalization condition:

$$\int_{\Omega} s_0(\mathbf{y}) \, d\Omega = 1. \quad (7.7)$$

Each agent contributes to the exploration of the domain, and its sensing influence is modeled through a sensing function $\gamma_i(\mathbf{r})$, where $\mathbf{r}(t)$ corresponds to coordinates in the agent's local reference frame. A visual illustration is provided in Figure 7.2

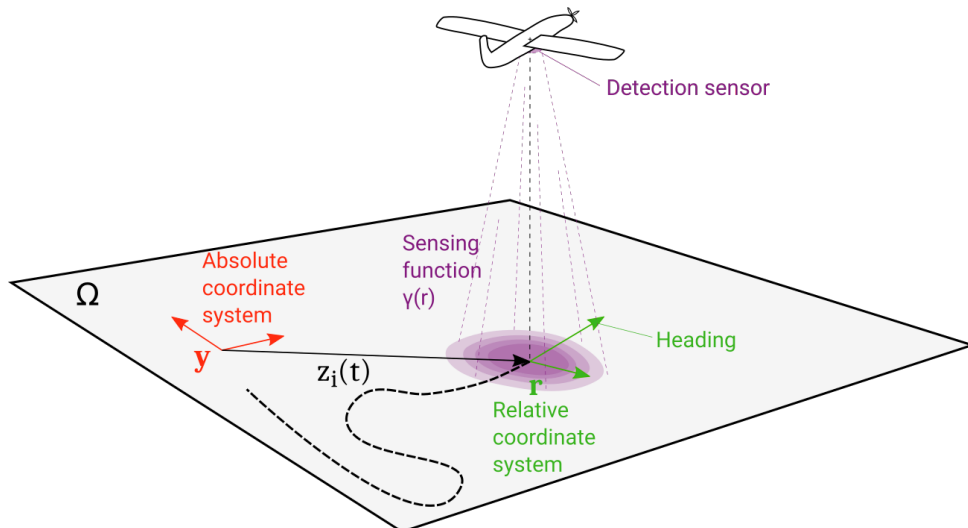


Figure 7.2: Absolute and local coordinate systems, along with the agent's sensing function γ_i .

The cumulative sensing effect exerted by all agents, expressed in the global coordinate system, is defined as

$$\Gamma(\mathbf{y}, t) = \sum_{i=1}^n \gamma_i (\mathbf{R}(\theta_i(t)) \cdot (\mathbf{z}_i(t) - \mathbf{y})), \quad (7.8)$$

with the rotation matrix \mathbf{R} given by

$$\mathbf{R}(\theta) = \begin{bmatrix} \cos \theta & -\sin \theta \\ \sin \theta & \cos \theta \end{bmatrix}. \quad (7.9)$$

The evolution of the search targets is determined by the vector field $\mathbf{w}(\mathbf{y}, t) : (\Omega \times t) \rightarrow \mathbb{R}^2$, representing the fluid flow which drives the dynamics of s . An advection-diffusion partial differential equation is employed, incorporating a sink term that models the impact of agents' sensing. The probability of a target remaining undetected, $s(\mathbf{y}, t)$, evolves according to

$$\frac{\partial s}{\partial t} = D \cdot \nabla^2 s - \mathbf{w} \cdot \nabla s - \Gamma \cdot s, \quad (7.10)$$

where D denotes the diffusion coefficient. The diffusion term accounts for the overall uncertainty in the system, which may arise from inaccuracies in the flow field, errors in initializing the undetected probability field, or localization errors affecting sensing. To incorporate this uncertainty, D is determined according to the adaptive formulation introduced in (7.1), ensuring consistency with the reconstruction error compensating approach used in the scalar transport model. Since the primary objective of the search is the rapid and sustained reduction of undetected targets, the ergodic search task can be formulated as

$$\lim_{t \rightarrow \infty} \int_{\Omega} s(\mathbf{y}) \, d\Omega = 0. \quad (7.11)$$

It should be noted that the search cannot be continued indefinitely, and its duration is not predetermined. Consequently, since the total search time is unknown, the exploration of the dynamic probability distribution cannot be formulated as a conventional optimization problem and is instead treated as an ergodic task.

7.4.2 Search agent motion model

The motion of each agent is described using the Dubins model, where a constant speed v_i is assigned to the agent while its heading angle θ_i is allowed to vary. Accordingly, the trajectory

of each agent is expressed as

$$\frac{d\mathbf{z}_i}{dt} = \begin{bmatrix} v_i \cdot \cos \theta_i \\ v_i \cdot \sin \theta_i \end{bmatrix}. \quad (7.12)$$

The evolution of the heading angle is dictated by the yaw angular velocity $\omega_i(t) = d\theta_i/dt$, which is limited by $|\omega_i| \leq \omega_i^{\max}$. This constraint also defines the minimal turning radius of the agents as $r_i^{\min} = v_i/\omega_i^{\max}$. It should be noted that, since the search is conducted using aerial robotic agents, the flow field \mathbf{w} does not influence their motion.

The agents' motion is directed by the HEDAC algorithm [160], which determines the $\omega(t)$ from a potential field $\phi(\mathbf{y}, t)$. This potential is obtained by solving the partial differential equation:

$$\alpha \nabla^2 \phi(\mathbf{y}, t) - \phi(\mathbf{y}, t) + s(\mathbf{y}, t) = 0, \quad (7.13)$$

where $\alpha > 0$ is a tuning parameter that controls the trade-off between local and global exploration. On the domain boundary B and any internal obstacles, Neumann boundary conditions are applied:

$$\left. \frac{\partial \phi}{\partial \mathbf{n}} \right|_B = 0, \quad (7.14)$$

with \mathbf{n} denoting the outward normal to the boundary B .

The normalized gradient of the potential field ϕ is then computed to guide the exploration agents:

$$\mathbf{v}(\mathbf{y}) = \frac{\nabla \phi(\mathbf{y})}{\|\nabla \phi(\mathbf{y})\|}. \quad (7.15)$$

Based on the gradient \mathbf{v} , the agents' yaw angular velocities are determined by

$$\omega_i = \frac{d}{dt} \left(\angle(\theta_i, \mathbf{v}(\mathbf{z}_i)) \right), \quad (7.16)$$

where the yaw rate ω_i may take positive or negative values, corresponding to the turning direction: positive ω_i denotes a counterclockwise turn, whereas negative ω_i indicates a clockwise turn.

7.4.3 Implementation of the integrated search framework

The proposed methodology is implemented by combining solvers for the advection, diffusion, and sensing of the probability density in (7.10), the potential field described by (7.13), and the agents' motion model in (7.12). The advection and diffusion components in (7.10) are computed using the Finite Volume Method (FVM) through the *scalarTransportFoam* solver in *OpenFOAM*. Sensing is applied directly to the probability field s at each time step, based on the agents' positions \mathbf{z}_i and their corresponding sensing functions γ_i . The potential field equation is solved using the Finite Element Method (FEM) with the *Netgen/NGSolve* library [162, 163], which also provides the gradient of the potential for motion guidance. The integration of the motion model, collision avoidance, utility calculations, visualization, and overall coordination of all components is carried out using the Python programming language.

In the implementation, motion control and sensing are updated at intervals of Δt , whereas the advection and diffusion simulations are computed using a finer time step of $\Delta t/10$ over the course of each control interval Δt .

The two coupled approaches operate differently, as *OpenFOAM* relies on FVM, while HEDAC employs FEM. To accommodate their respective tasks, the underlying meshes are structured differently. *OpenFOAM* applies a three-dimensional hexahedral FVM mesh with a single element along the third dimension to handle the two-dimensional advection-diffusion problem, whereas HEDAC uses a two-dimensional triangular FEM mesh. Furthermore, FVM stores field values at cell centers, while FEM stores them at the mesh nodes, necessitating data transfer between meshes.

The integration of the methods is performed such that agents' sensing effects are directly applied to the FVM scalar field, after which the probability field s is projected onto the FEM mesh for the potential field computation. The projection is implemented using the nearest neighbor interpolation method due to its computational efficiency. Only the probability field s accumulates errors, as the potential field ϕ is recomputed from the updated values of s at each time step. Consequently, the use of the nearest neighbor interpolation and its associated coarseness is considered acceptable.

The integration of the two computational methods is achieved by directly updating the FVM scalar field with the effects of agents' sensing. After this, the probability field s is projected to the FEM mesh to calculate the potential field ϕ . This is done with nearest neighbor interpolation, chosen for its computational simplicity. Only the probability field s is subject to error

accumulation, since the potential field ϕ is recomputed from the updated s values at each time step. The minor coarseness introduced by this interpolation method is therefore considered acceptable for the intended computations.

The complete workflow of the proposed methodology is outlined in Figure 7.3.

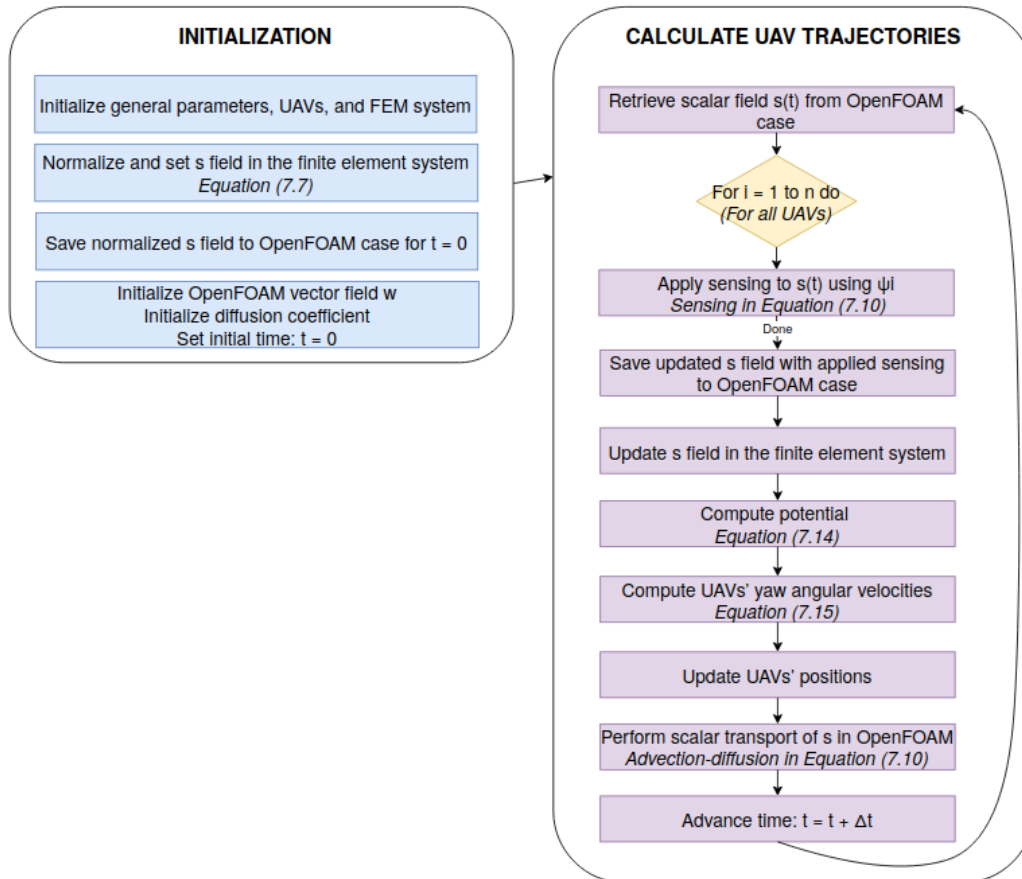


Figure 7.3: UAV navigation procedure based on dynamic probability fields.

8 SIMULATION RESULTS

This chapter presents the outcomes of the proposed methodology, structured to demonstrate its performance under various conditions and validation scenarios. The results are divided into three main parts. First, the preparation of test cases is outlined, providing the foundation for subsequent analyses. Second, the steady reconstruction approach is examined, focusing on multimodality, optimization benchmarks, mesh independence, and validation based on realistic measurements. Finally, the transient flow reconstruction is analyzed, including robustness testing with determination of the optimal sampling period T_s , followed by validation of different approaches for transient flow approximation and the associated passive scalar advection.

8.1 Preparation of test cases

The simulation domains used in the test cases are either synthetic, designed for controlled experimentation, or based on real-world geography to support practical applications. For synthetic domains, the mesh was generated in OpenFOAM using the `blockMesh` utility. This tool allows the user to create a structured grid by defining the computational domain as a set of blocks. Each block is specified by its corner vertices, the number of cells along each edge, and the way edges are shaped or curved. By combining multiple blocks, complex geometries can be approximated, and the resulting mesh defines the spatial resolution for simulations. The example of a numerical mesh generated using `blockMesh` is presented in Figure 8.3.

For realistic domains, coastline shapes were extracted using the Sentinel Hub [164] platform, which provides satellite-derived products such as the Level-2A NDWI (Normalized Difference Water Index), and generates the corresponding computational mesh in OpenFOAM.

The NDWI is a spectral index commonly used to identify surface water features by enhancing the contrast between water and land. It is computed using the surface reflectance values from the green and near-infrared (NIR) spectral bands, as introduced in [165]:

$$\text{NDWI} = \frac{\text{Green} - \text{NIR}}{\text{Green} + \text{NIR}}, \quad (8.1)$$

where water bodies typically yield positive values, while land and vegetation result in zero or negative values. The calculation of (8.1) helps isolate water bodies in satellite imagery by enhancing their spectral signature.

The NDWI data is then retrieved from georeferenced TIFF images, which include both the pixel-wise NDWI values and the spatial metadata necessary for geolocation. Using this metadata, each pixel in the image is mapped to geographic coordinates (latitude and longitude). After normalizing the NDWI image to an 8-bit range, a threshold is applied (e.g., $NDWI > 0.25$, corresponding to 165 in the 0-255 scale) to segment water bodies from land. The difference between water bodies from land is visible on the TIFF image presented in Figure 8.1.

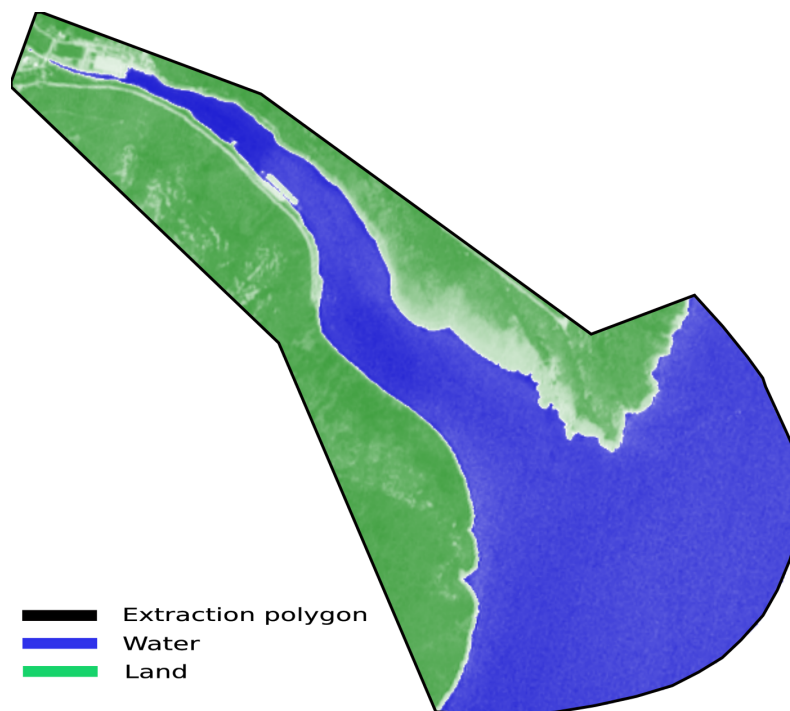


Figure 8.1: The figure illustrates the coastline extraction polygon derived from the NDWI image. Blue colors represent water surfaces, while green areas correspond to land. The clear contrast between these regions reflects the NDWI value distribution, enabling accurate delineation of the coastline for mesh generation.

Contours are extracted from the binary image using standard image processing techniques, and the largest contour is selected to represent the coastline. This raw coastline is initially defined in pixel coordinates, then transformed to geographic coordinates using the image's bounding box and resolution. To improve the accuracy and smoothness of the coastline, a moving average is applied along the contour before it is exported in both global and local coordinates. This process is visible on Figure 8.2.

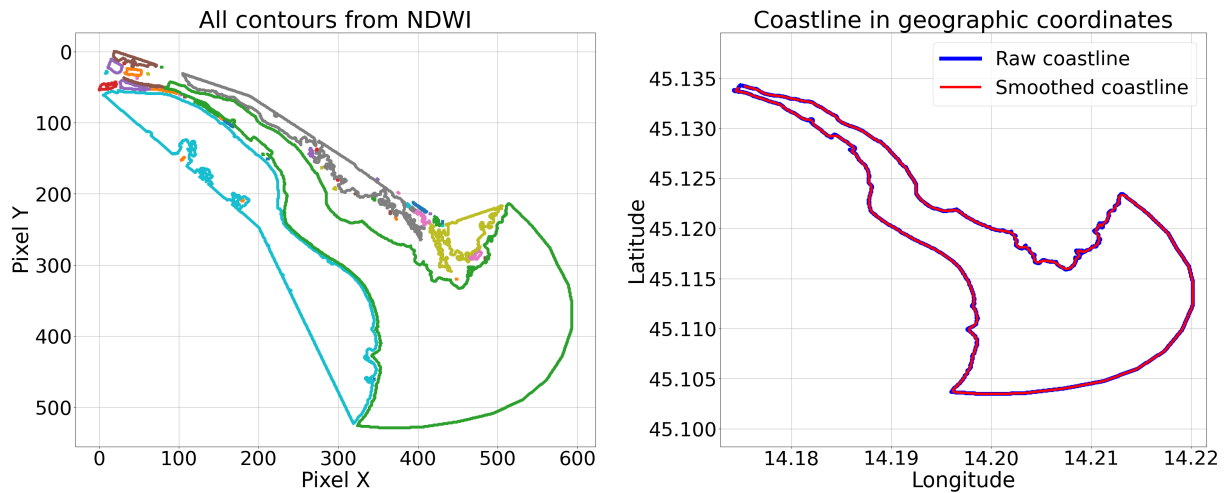


Figure 8.2: Figure depicts the process of coastline extraction from the NDWI image. The largest constour representing raw coastline contour (blue) is smoothed (red) and prepared for conversion from pixels to geographic coordinates.

The refined coastline polygon is used to generate a stereolithography (STL) surface model, which provides the geometric basis for creating the computational mesh. STL model is used with the cfMesh meshing library [166] to generate a two-dimensional mesh, which is subsequently imported into OpenFOAM. This workflow enables accurate representation of coastal geography and supports physically consistent simulations of surface flows in real-world environments. Examples of mesh generation using both blockMesh and cfMesh are shown in Figure 8.3.

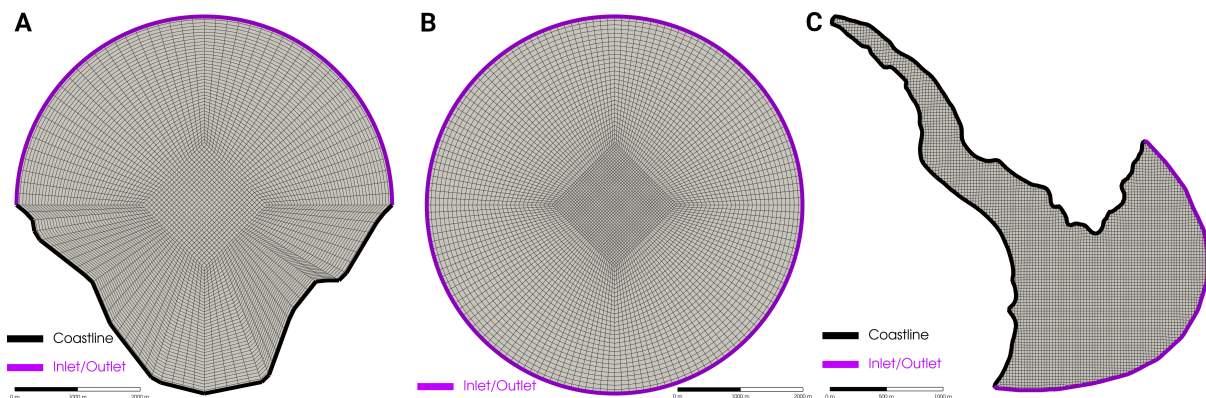


Figure 8.3: (A) Synthetic domain mesh with coastline generated with blockMesh. (B) Synthetic domain mesh without coastline generated with blockMesh. (C) Realistic domain mesh generated with cfMesh.

To validate the proposed methodology, six distinct test cases were developed, each representing a different domain type: a synthetic domain, five realistic domains with distinct features,

and two domains incorporating experimental field measurements. The selected domains vary in size, geometry, boundary complexity, and the presence of coastal features or islands. The key characteristics of each test case are outlined in Table 8.1, providing an overview of the computational and physical properties considered during the simulations.

Table 8.1: Characteristics of the simulation test cases.

Case characteristics	Simple bay	Gulf of Trieste	Vis	Unije	Plomin bay	Valun bay
Test case type	Synthetic	Realistic	Realistic	Realistic	Experimental	Experimental
Domain area [km^2]	24.6	498.94	2273.9	96.49	3.37	55.62
Number of boundaries	1	1	5	4	1	1
Total boundary length [km]	9.4	20.52	120.97	9.63	3.74	7.22
Coastline length [km]	9.1	86.64	197.61	57.12	8.34	31.74
Number of boundary control points	5	5	14	6	3	3
Max velocity in the domain [m/s]	0.25	0.2	0.35	0.4	0.4	0.5
Number of cells	4625	8262	12856	7530	5676	15833
Average cell size [m]	73.02	245.74	412.41	113.21	24.36	59.28

8.2 Analysis of steady flow reconstruction approach

Validation of the steady flow reconstruction methodology serves as the foundation for the quasi-steady approach used in the transient flow replication. The primary objective is to evaluate the effectiveness and limitations of the steady flow fit process by analyzing its performance across different test cases. The section includes a benchmark of optimization outcomes to illustrate potential convergence scenarios, as well as validation results in a realistic domain where real-world drifter measurements were used. These analyses are essential for confirming that the reconstructed steady flow fields achieve sufficient accuracy and that the optimization process is effective, thereby ensuring reliable transient reconstruction in the subsequent stages.

8.2.1 Multimodality

Given that proposed reconstruction processes are at their core optimization problems, a conventional test case, lid-driven cavity, was chosen to determine the best optimization approach. This configuration consists of a square cavity with an area of $1m^2$ filled with fluid, where flow is generated by moving the top lid, controlled through three designated points. The induced motion leads to the development of recirculation zones and vortices, which were the focus of the reconstruction process. A total of 100 different measurement setups were tested, each involving 100 measurement points, with tangential inlet velocities ranging from $-2 m/s$ to $2 m/s$, resulting

in Reynolds numbers up to 200, assuming a kinematic viscosity of 10^{-2} . To accurately capture the complex flow patterns, a structured mesh of 40000 cells was used. Steady-state simulations were employed to investigate the influence of varying Reynolds numbers on the stability, scale, and behavior of the resulting vortical structures.

The findings revealed that identical velocity vectors at specific measurement points can arise from multiple distinct boundary condition combinations. As a result, optimizing to match a target velocity at a single location does not ensure that the overall flow field is accurately represented. This phenomenon is illustrated in Figure 8.4. Given this ambiguity, local search strategies are considered inadequate for the optimization framework adopted in this study.

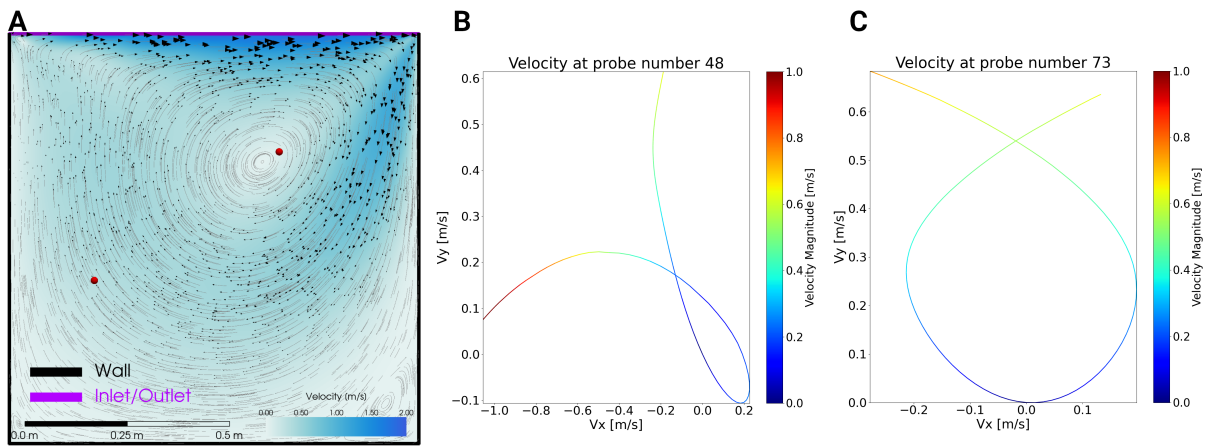


Figure 8.4: Analysis of the multimodal characteristics of the flow fitting task. (A) shows the cavity lid scenario at $Re = 160$ with two marked observation points. (B) presents overlapping velocity profiles at point 48 (left marker), indicating identical local velocities from different boundary conditions, with another example shown in (C) at point 73 (right marker).

Analysis of all measurement positions throughout the parameter range confirmed that multiple optimization inputs can yield the same velocity at specific points in the domain. This behavior reflects the multimodal nature of the problem, indicating that different boundary configurations can produce indistinguishable flow characteristics at certain locations.

8.2.2 Optimization methods and benchmark

In all optimization tests, the objective function is defined using the root mean squared velocity difference at measurement locations, denoted as E_d . Convergence is considered achieved once the measurement velocity error, E_d , falls below the threshold of 10^{-2} , equivalent to a drifter velocity error of 1 cm/s. In addition, the accuracy of the reconstructed velocity field is assessed

using a separate metric, E_f , with a threshold set at $2 \cdot 10^{-2}$, which translates to a drifter velocity error of 2 cm/s. It is important to note that E_f is not incorporated into the optimization process itself, but is instead just monitored to provide a more comprehensive evaluation of flow field reconstruction quality. This metric is calculated for all test cases to ensure consistency in assessing the spatial accuracy of the reconstructed fields. Based on conducted tests, setting E_f to be three times larger than the drifter-based error E_d has proven effective in confirming that the reconstructed flow adequately matches the reference field. All results satisfying both error thresholds are considered acceptable.

Using the computed values of E_d and E_f , the optimization outcomes can be categorized into four distinct groups:

- $E_d > 0, E_f > 0$ (red region)

This represents cases where the optimization did not satisfy both the drifter and field error thresholds.

- $E_d > 0, E_f \approx 0$ (gray region)

A less frequent outcome in which the field error falls within the acceptable limit, but the drifter error remains above the defined threshold.

- $E_d \approx 0, E_f > 0$ (orange region)

Cases where the drifter error meets the target, but discrepancies remain in the reconstructed velocity field compared to the referent one.

- $E_d \approx 0, E_f \approx 0$ (green region)

The ideal outcome, where both drifter and field errors fall below their respective thresholds, indicating a successful reconstruction of the surface velocity field.

Figure 8.5 presents a visual representation of the four distinct groups according to optimization error, obtained during the initial testing phase using the Particle Swarm Optimization (PSO) algorithm.

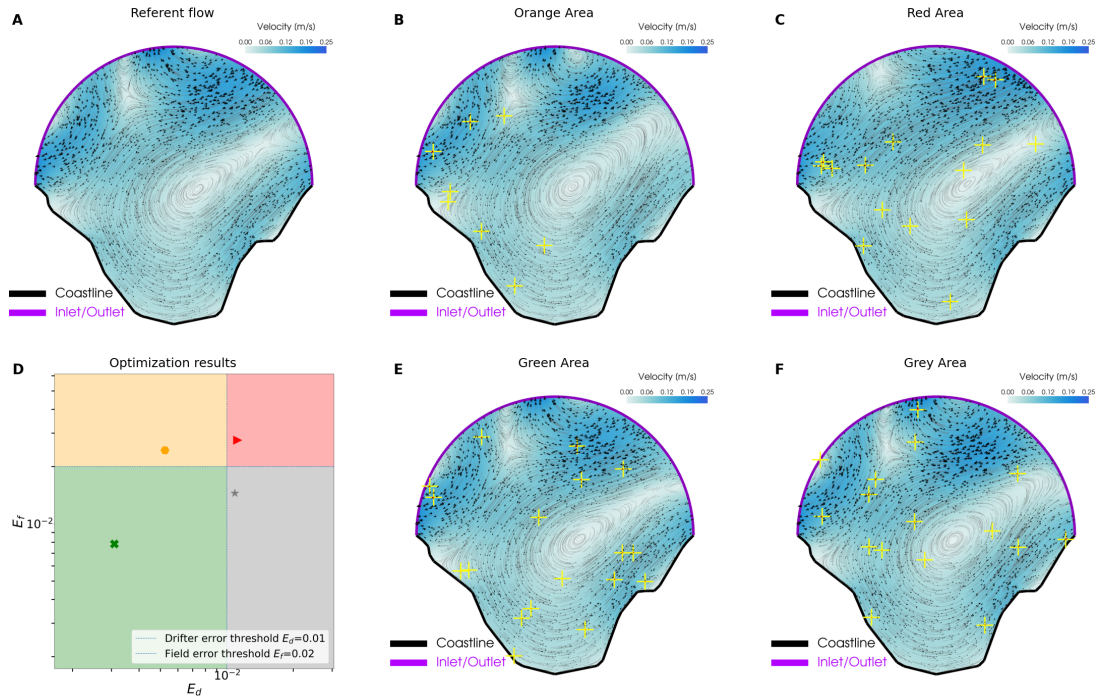


Figure 8.5: **(A)** The referent flow that needs to be reconstructed. **(B)** Velocities matched locally but field error threshold not met. **(C)** Main vortex captured, but northern flow diverges. **(D)** Distribution of optimization outcomes. **(E)** Both drifter and field errors are within limits. **(F)** Field error threshold met, but drifter error not met.

Since reconstruction accuracy depends on the placement of measurement points, the figure confirms the hypothesis that the orange scenario ($E_d \approx 0$, $E_f > 0$) will progressively move toward the green region ($E_d \approx 0$, $E_f \approx 0$) as the number of measurements increases. Conversely, the red scenario ($E_d > 0$, $E_f > 0$) represents a poorly resolved case where adding more measurements does not improve the solution due to insufficient information in critical areas for the optimization algorithm. The grey scenario ($E_d > 0$, $E_f \approx 0$) yields a flow field closely resembling the referent one, with minor velocity deviations at measurement locations. Such instances are uncommon and likely caused by numerical inaccuracies, consistently hovering near the threshold. Although this scenario is very similar to the referent flow, slight differences in measurements can prevent meeting the error threshold. These results emphasize the importance of drifter placement, suggesting that a more uniform distribution could enhance reconstruction accuracy. While varying the error thresholds might produce slightly different outcomes, the current thresholds depicted in the figure appear appropriate for flow reconstruction, given that the absolute error remains below 0.03 cm/s.

To identify the most suitable optimization algorithm for the proposed flow field reconstruction, various methods available in the Python optimization library Indago [167] were assessed. Only the most promising approaches are presented here. The focus was on global search algorithms, as local search methods were excluded due to the multimodal characteristics of the problem discussed in Section 8.2.1. In addition to the PSO algorithm, initially chosen for testing due to its widespread use and proven efficiency in solving complex optimization tasks [168], the Fireworks Algorithm (FWA) was also employed for its potential advantages over PSO, particularly in terms of faster convergence and improved global search capabilities [169]. The Artificial Bee Colony (ABC) algorithm was also considered due to its strong performance in complex search spaces across a variety of optimization problems [170]. To contrast global and local search strategies, the MSGS algorithm [167], a variant of the GPS-MADS method [171], was used to represent local search approaches. Unlike the stochastic global algorithms, MSGS employs a deterministic mesh-based strategy that systematically refines the search space.

Ten distinct Simple bay test cases were randomly generated, each serving as a referent case. Each optimization algorithm was executed 10 times per reference case, utilizing 10 measurement points for flow field reconstruction, resulting in a total of 100 optimization runs per algorithm. The corresponding results are presented in Figure 8.6.

It is clear that, on average, all algorithms met the defined threshold successfully, with 6.5% of results falling in the red region, 5.75% in orange, 3.25% in gray, and the remaining 84.5% in green. The local search method MSGS exhibited notably fast convergence but achieved higher fitness values compared to the global search algorithms. Moreover, as highlighted in the cavity lid test case, MSGS is susceptible to becoming trapped in a local optimum. Consequently, global search techniques were favored for the modeling approach, with Particle Swarm Optimization (PSO) identified as the most effective among them. Despite its effectiveness, PSO converges more slowly than MSGS.

Given the differences in complexity and size among the test cases, PSO was selected as the preferred method, allowing for better capture of complex flow features while avoiding local minimum. This approach was further validated with 50 optimization runs per algorithm, revealing less than 2% variation in results. These findings align with previous observations and support the conclusions drawn.

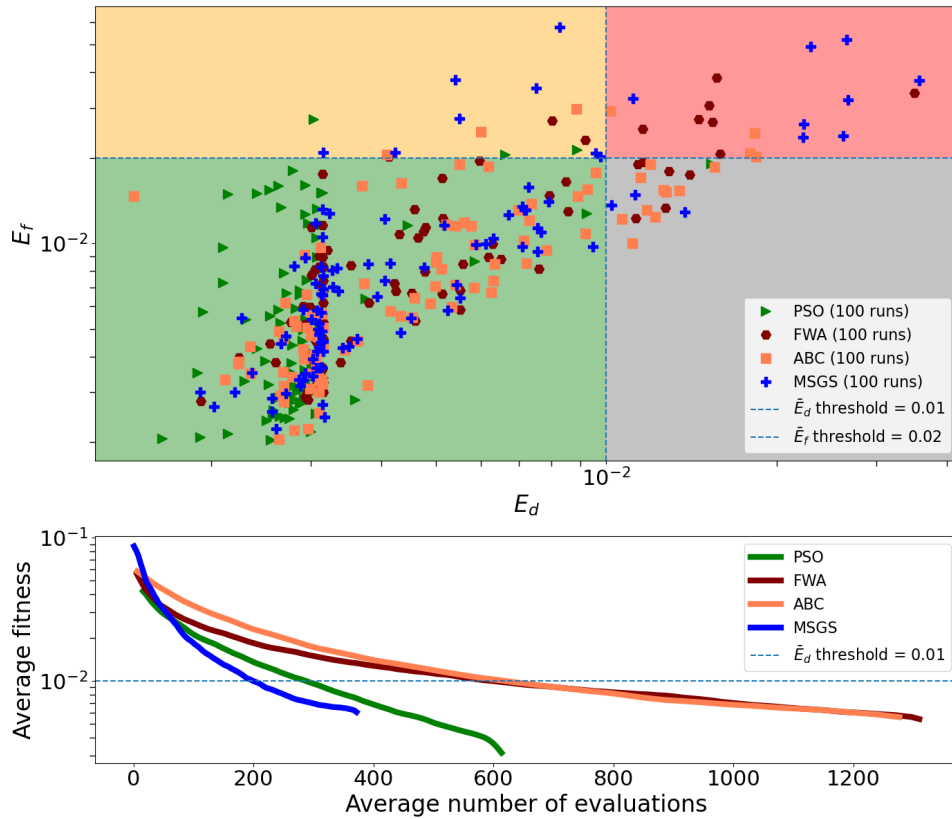


Figure 8.6: Overview of optimization algorithms for flow field reconstruction. Colored squares denote four outcome categories, while the lower panel shows average convergence trends.

8.2.3 Impact of available measurements on flow reconstruction accuracy

The accuracy of surface flow field reconstruction is influenced not only by the total number of measurements but also by their spatial distribution within the domain. In this context, the concept of the effective number of measurements (η) was examined, representing the number of points that provide unique and informative data for reconstructing the flow field.

Figure 8.7 presents the influence of η on the reconstruction results, based on 100 optimization runs for each configuration using 1 to 20 measurement points randomly placed within the Simple bay domain. When only a few measurement points are used (e.g., between 1 and 3), the drifter error E_d often meets the convergence threshold, yet the corresponding field error E_f remains high (represented in orange), indicating insufficient domain information for accurate flow reconstruction. As the number of measurement points increases, the optimization algorithm gains access to more spatially informative data, resulting in improved field reconstruction performance (shown in green).

The orange region should not be interpreted as a failure of the optimization itself, but rather

as a consequence of limited spatial coverage, where the available measurements do not adequately capture the full complexity of the flow. This becomes more evident in the second plot, where the orange region vanishes as the availability of unique measurement information improves.

The second and third plots offer complementary perspectives: the second highlights the proportion of successful reconstructions relative to η , while the third shows the absolute number of optimization runs associated with each η value. Notably, very few runs correspond to higher values of η , reflecting the limitations imposed by random measurement sampling. In some cases (e.g., $\eta = 19$ or $\eta = 20$), no data is available due to insufficient domain coverage under random configurations.

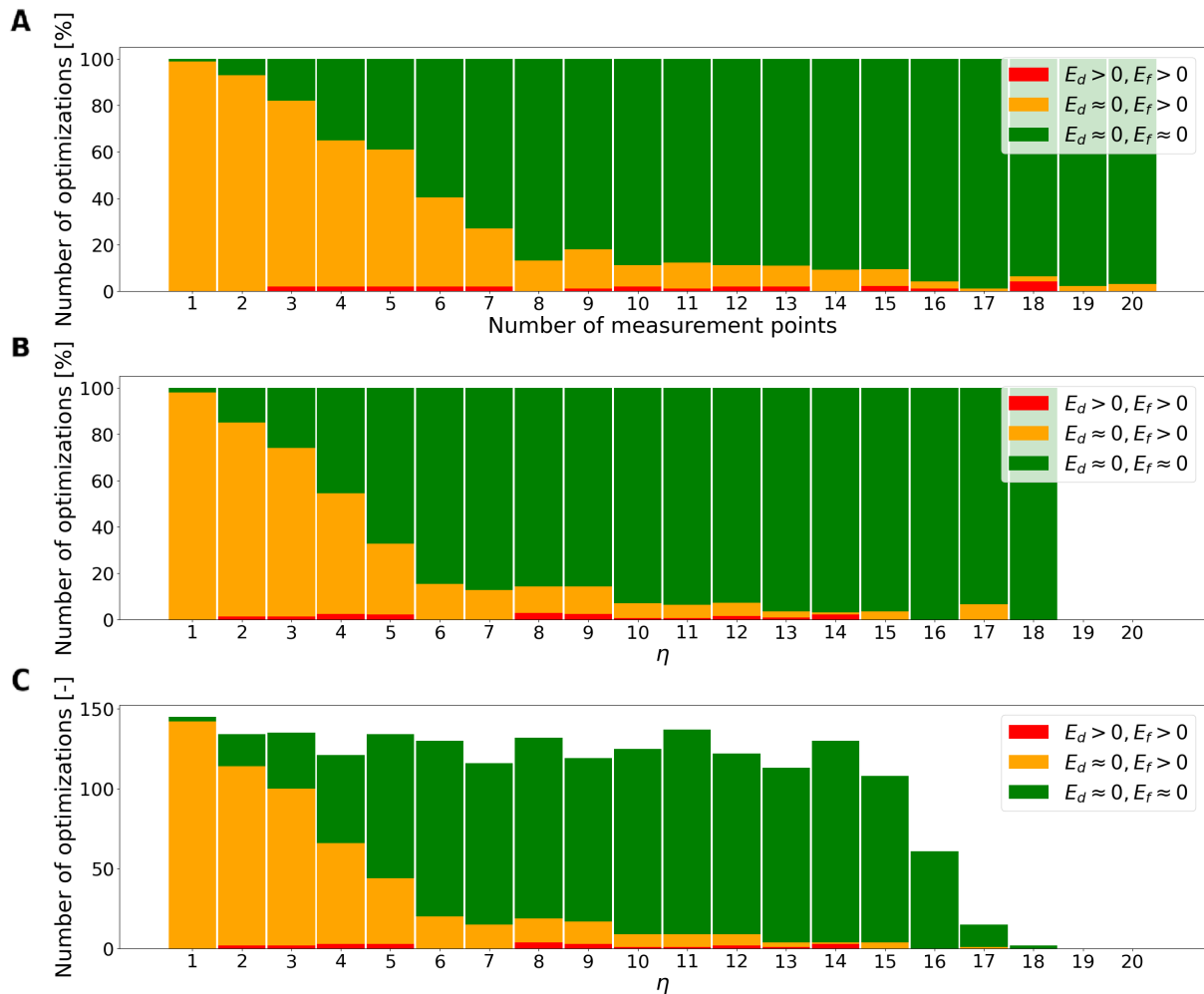


Figure 8.7: Results of 100 optimization runs with 1–20 randomly distributed measurement points. (A) Optimization success based on measurement points. (B) Optimization success relative to the effective number of measurement points, while (C) presents their absolute distribution.

8.2.4 Mesh independence

Given that the method is intended for near-real-time use, when computationally expensive numerical simulations are impractical, a coarse numerical mesh for the CFD model is required. To evaluate the accuracy of simulation results under this constraint, a mesh convergence analysis was carried out using a standard meshing approach. For the synthetic Simple bay test case, three meshes were generated: coarse (4625 cells), medium (10564 cells), and fine (23296 cells), maintaining a uniform refinement ratio of 1.5. The Grid Convergence Index (GCI) was calculated based on vorticity values at all mesh points, following the procedure from [172], which applies Richardson extrapolation to estimate the convergence order. As summarized in Table 8.2, the results indicate that the solution lies within the asymptotic convergence range. Further evidence is provided by an estimated order of convergence of $p = 1.79$ and an average correction factor $\bar{c}_c = 0.976$, which exceeds the standard threshold of 0.95, indicating consistent error behavior with mesh refinement.

Table 8.2: Mesh characteristics and Grid Convergence Index (GCI) values for the synthetic Simple Bay case. Vorticity values were evaluated at all grid points.

Mesh	Number of Cells	Refinement Ratio (r)	Relative Error (%)	GCI (%)
Coarse	4625	1	—	—
Medium	10564	1.5	1.53	1.09
Fine	23296	2.25	0.76	1.34

8.2.5 Case studies of Steady Flow Fit

Datasets with detailed, simultaneous surface current measurements were selected to validate the method and assess the impact of different observations on reconstruction accuracy. One key dataset originates from the TOSCA experiment in April 2012 [173], containing simultaneous HF-radar and drifter measurements for the Gulf of Trieste. This makes it an excellent test case for seeing how well this approach works with different measurement types.

The method was further validated with HF-radar measurements from the Stončica-Ražanj stations near the island of Vis. This data, collected in October 2019 and provided by the Institute of Oceanography and Fisheries [174], helps validate this method in a region with complex coastal features, despite the radar stations no longer being active.

The method's reliability under sparse data conditions was tested by reducing the number of measurements and observing the impact on flow reconstruction accuracy. This allows assessment of the method's performance in realistic scenarios with limited observational data.

8.2.5.1 Gulf of Trieste

The Gulf of Trieste, located at the northernmost edge of the Adriatic Sea, is a shallow bay spanning over 500 square kilometers. Surface flow patterns in this region have been the subject of detailed investigation, particularly in [118], where a combination of high-resolution outputs from the Northern Adriatic Princeton Ocean Model (NAPOM), HF-radar data, and measurements from ADCPs was employed. This study highlighted a wide range of surface velocities, typically from below 0.1 m/s up to over 0.5 m/s, and reported that the RMSE between radar-based and model-derived currents mostly fell within 8.6 to 11.2 cm/s for 80% of the dataset.

In a related study, [16] performed a targeted validation of HF-radar surface velocities by comparing them to Lagrangian data obtained from CODE drifters. They found an RMSE of approximately 10 cm/s for the radial velocity component, aligning well with commonly accepted HF-radar accuracy thresholds in the 5–15 cm/s range [109, 175–177].

In a comparable effort, [120] applied the MIKE3/21 hydrodynamic modeling system in conjunction with localized measurements of wind, waves, currents, and sea level to analyze current patterns in the northern Adriatic region. Their work involved a detailed sensitivity analysis, testing various model parameterizations and configurations. The model outputs were compared with in-situ measurements such as wave height, current velocity, water level, and temperature, along with results from a high resolution implementation of the COAWST modeling framework applied in the same area. During a year-long simulation, the MIKE3/21 model demonstrated good agreement with observational data, performing similarly to COAWST. Specifically, the RMSE in surface current velocities, validated using observations from the “Acqua Alta” platform, was approximately 13 cm/s.

Together, these studies highlight the complex and varied nature of surface circulation in the Gulf of Trieste. The validation of the Gulf of Trieste surface flow was carried out using data obtained as part of the TOSCA experiment in April 2012 [173], with available measurements shown in Figure 8.8. This visualization outlines the measurement sources, with HF-radar velocity vectors available at 225 locations throughout April 2012, and 44 drifters deployed between April 23 and May 4, 2012.

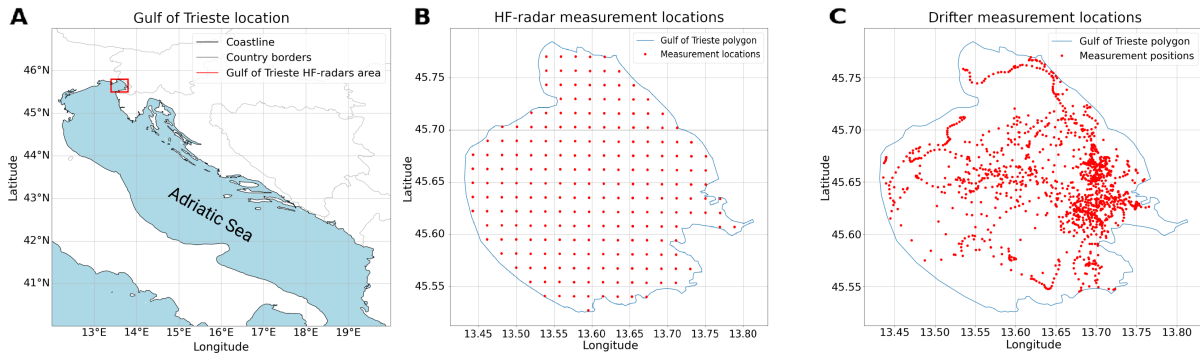


Figure 8.8: (A) Gulf of Trieste location. (B) HF-radar velocity vectors available at 225 locations for April 2012. (C) Positions of 44 drifters deployed between April 23 and May 4, 2012.

To assess the influence of measurement data on flow reconstruction from drifter and HF-radar sources, a fixed evaluation time was selected. Drifter data collected at 4:00 AM on April 24, 2012, provided 15 drifter positions, which were relatively clustered. Further examination of the HF-radar measurements revealed inconsistencies with the continuity principle, as several flow vectors pointed toward the coastline, as visualized in Figure 8.9. These inconsistencies are likely due to strong wind effects on the sea surface, which alter the current direction and drive flow toward the shore. This phenomenon has also been acknowledged in earlier studies [118, 178], highlighting the substantial role of local atmospheric conditions in modulating surface currents. Consequently, wind forcing was included by adding the wind vector field to the x and y components of the domain-wide velocity. While mass flux conservation is preserved, the resulting vectors are biased toward the coastline, providing a more realistic match to the observed data.

For both the drifter and HF-radar cases, three control points were used, corresponding to six optimization parameters. While the drifter dataset was relatively sparse, the HF-radar measurements offered a much denser spatial coverage. Sensitivity analyses were conducted by reducing the available measurement data to evaluate the robustness of the reconstruction method. A reduction of $x\%$ indicates that $(100-x)\%$ of available data points are used for reconstruction as n_{MP} , while the remaining $x\%$ are reserved for observation as n_{FP} . Specifically, the drifter data points were reduced by 7% and 30%, while the HF-radar data points were reduced by 10%, 50%, and 90%. Reconstruction accuracy was then evaluated using the full dataset as a reference for field error. Representative flow reconstructions for the 30% drifter data points reduction and 50% HF-radar data points reduction are shown in Figure 8.9.

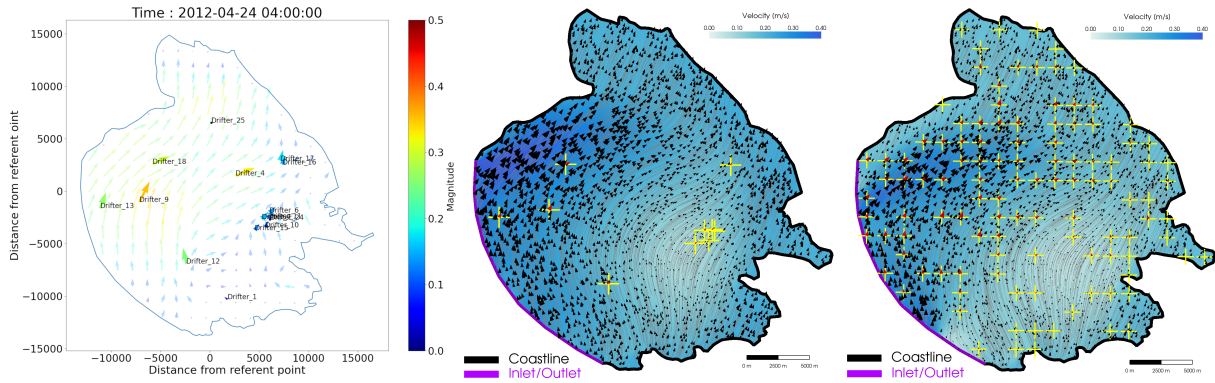


Figure 8.9: (A) Combined drifter and HF-radar data at 4:00 AM on April 24, 2012. (B) Flow reconstruction based on a 30% reduction of drifter measurements. (C) Flow reconstruction based on a 50% reduction of HF-radar measurements.

To generate meaningful results across different data availability scenarios, 50 independent optimization runs were performed for each case. The outcomes of these assessments, along with the corresponding data reduction levels, are summarized in Table 8.3.

Table 8.3: Data coverage and reconstruction performance for the Gulf of Trieste.

Data Source	Available measurements	Reduction [%]	n_{MP}	n_{FP}	\bar{E}_d [cm/s]	\bar{E}_f [cm/s]
Trieste drifters	15	7	14	1	8.2	5.6
	15	30	10	5	7.9	7.6
Trieste HF radars	225	10	202	23	10.1	9.9
	225	50	112	113	9.7	10.2
	225	90	23	202	8.5	11.2

* $\bar{\cdot}$ is average across 50 optimization runs.

The comparison of flow fields reconstructed using drifter and HF-radar measurements reveals distinctions stemming from differences in measurement principles. In the vertical dimension, HF-radar data represent depth-weighted averages influenced by radar frequency and vertical current shear [179, 180], while drifter data represent near-surface motion at a discrete depth. Horizontally, HF-radar values are spatially averaged over large grid cells spanning several kilometers, whereas drifter data capture movement at a much finer scale, typically on the order of 1 meter [177].

Despite methodological differences, the reconstructed velocity fields from both data sources exhibit similar spatial patterns, with some expected variations. The dominant flow features, their directions, magnitudes, and associated RMSE values indicate that the proposed meta-model fitting approach delivers consistent performance, particularly in capturing non-physical currents directed normal to the coastline/shoreline.

8.2.5.2 Vis island

The region surrounding the island of Vis, located in the central Adriatic near the Croatian coast, spans over 2200 square kilometers. This area serves as a comprehensive test case due to its complex geography, which includes numerous islands, inlets, and outlets, which are features that encompass a wide range of potential modeling challenges. The dataset used for this analysis was provided by the Institute of Oceanography and Fisheries [174], and consists of HF-radar measurements collected in October 2019 from two radar stations, which are now inactive. The study area was intentionally defined to be broader than the direct coverage of the HF-radar system, in order to capture the flow development leading into the radar-observed region, as illustrated in Figure 8.10.

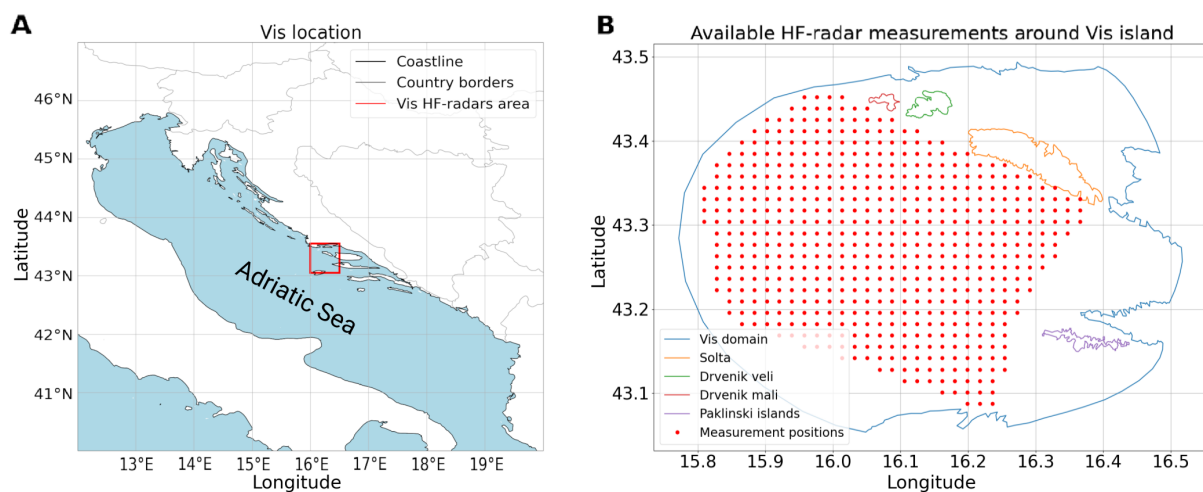


Figure 8.10: (A) Study area around Vis island, with over 2200 km². (B) Spatial distribution of 555 HF-radar velocity measurements, including four islands and parts of the mainland coastline.

As shown in Figure 8.11, the reconstructed surface flow closely resembles the general flow structure captured by the HF-radar measurements, although finer details such as small-scale vortices are not fully resolved in some areas. These discrepancies may stem from the resolution used in the simulation setup, which prioritized computational efficiency over fine-scale accuracy, or from the limited density of measurements in certain regions. To assess the impact of measurement availability on reconstruction quality, data subsets corresponding to 10%, 50%, and 90% reduction were used. The results demonstrate that even with significantly fewer input measurements, the main flow patterns are still recognizable. Examples of flow reconstruction under 50% and 90% data reduction are shown in Figure 8.11, highlighting the method's ability to maintain structural consistency despite limited observational data.

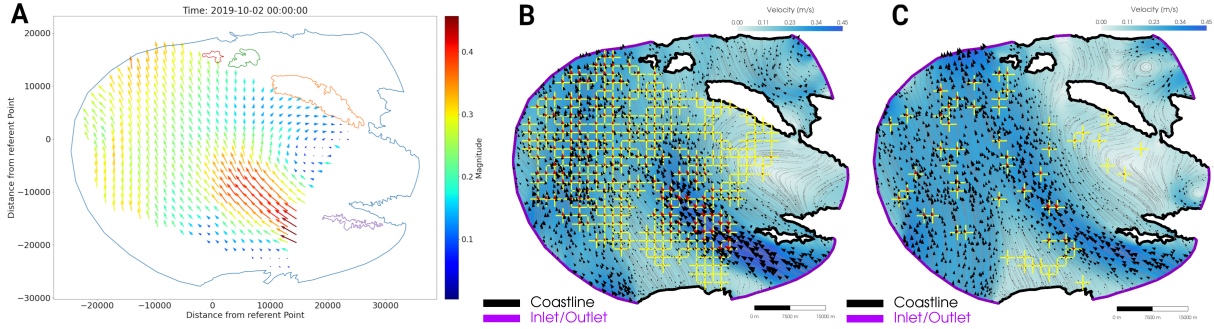


Figure 8.11: (A) HF-radar measurement locations with velocity vectors colored by magnitude. (B) Reconstructed flow using 277 measurements and 278 field points (50% data reduction). (C) Reconstruction with 55 measurements and 500 field points (90% reduction).

Furthermore, as shown by the average RMSE values over 50 optimization runs in Table 8.4, results confirm that even with significant reductions in measurement points, the flow reconstruction remains highly accurate.

Table 8.4: Data availability for the Vis case.

Data Type	Available data points	Reduction [%]	n_{MP}	n_{FP}	\bar{E}_d [cm/s]	\bar{E}_f [cm/s]
Vis HF radars	555	10	500	55	5.7	5.8
	555	50	277	278	5.4	5.5
	555	90	55	500	5.0	6.0

* $\bar{\cdot}$ is average across 50 optimization runs.

These results validate the robustness and effectiveness of the simulation-based optimization method for surface flow reconstruction.

8.3 Analysis of transient flow reconstruction

The transient reconstruction approach extends the flexibility of the discussed methodology by addressing the unsteady flow dynamics using a series of short steady-state simulations, performed at regular intervals. During each interval, boundary conditions are updated based on reference measurements, allowing the system to adapt to gradual flow changes without the need for computationally intensive full transient simulations. This approach reduces temporal complexity, while the fusion model addresses spatial complexity by integrating information from both domains. Through this iterative process, the resulting passive scalar transport better captures real-world behavior, particularly in situations where temporal variations strongly influence advection. In order to clarify the iterative process of the method, the complete optimization-simulation loop for each measurement interval is shown in Figure 8.12.

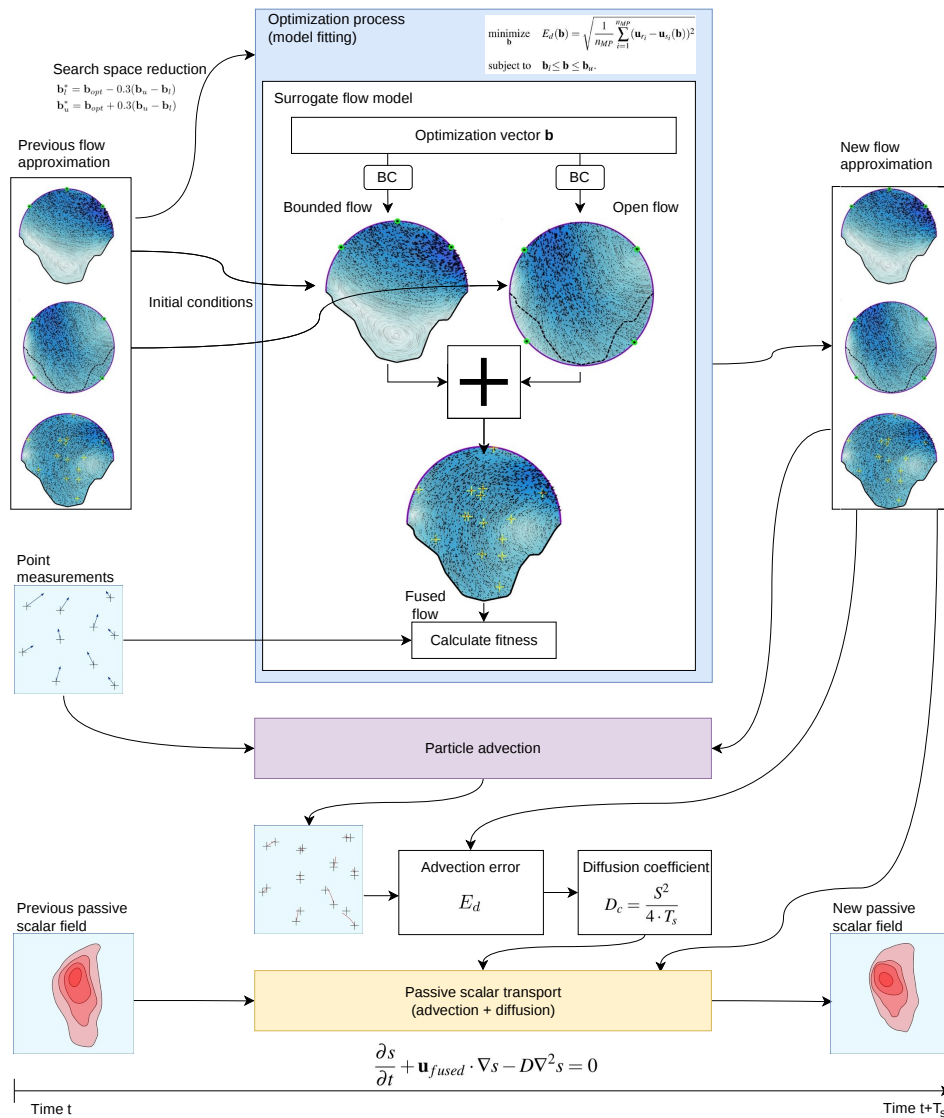


Figure 8.12: Schematic of the optimization–simulation workflow initiated at time t for evaluating scalar transport over interval $[t, t + T_s]$.

The workflow consists of measuring velocity fields, performing dual-domain simulations in OpenFOAM, optimizing boundary conditions, fusing velocity fields, evaluating errors, and iteratively minimizing the drifter-based error E_d . This cycle is repeated for each subsequent time step incremented by T_s , reconstructing the transient flow field in stages.

8.3.1 Robustness analysis of quasi-steady period

Choosing an appropriate value for T_s is essential. Choosing an appropriate value for T_s is essential. While a longer T_s provides the optimization more time to improve the reconstruction,

excessively long T_s can lead to errors due to temporal changes in the flow affecting passive scalar transport. The accuracy of scalar advection is directly influenced by the quality of the reconstructed velocity field, and any discrepancies tend to accumulate over time. The effect of T_s was investigated by evaluating reconstruction accuracy through the RMSE of the full velocity field (E_f) over a range of T_s values from 300 to 1500 seconds in the Simple Bay test case. For each selected T_s , 10 separate optimization runs were conducted to account for algorithmic randomness, and the median E_f was calculated. The outcomes of this evaluation are illustrated in Figure 8.13.

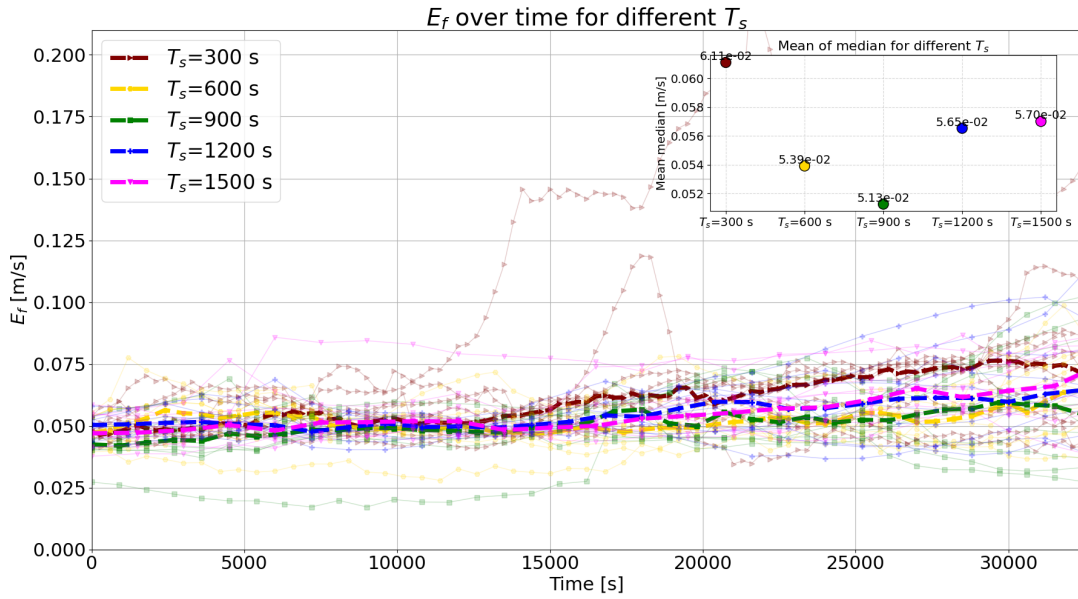


Figure 8.13: Reconstruction error (E_f) of the velocity field obtained for five different values of T_s .

Faded lines on Figure 8.13 correspond to individual optimization runs, while the bold dotted line denotes the median E_f for each set. The inset in the top-right corner shows the average of median E_f values, highlighting the balance between reconstruction time and error introduced by flow evolution. From these results, $T_s = 900$ s is chosen as the optimal interval. Decreasing T_s makes the optimization more difficult, while increasing it enhances transient effects. This chosen value therefore provides a balance between accurate flow reconstruction and minimal error due to temporal variations.

8.3.2 Case studies of Transient Flow Fit

The proposed quasi-steady approach was evaluated using two test cases: the familiar synthetic scenario called Simple Bay, and the realistic domain, the Unije Channel near the island of

Lošinj. The goal was to achieve accurate reconstruction of passive scalar advection to assess the method's suitability for such applications, with the level of accuracy primarily depending on the quality of the flow reconstruction. Based on the results presented in Section 8.3.1, a T_s value of 900 seconds was used in both cases. To assess the method's performance, passive scalar advection was compared across four different approaches: steady flow reconstruction, transient flow reconstruction without the fusion model (using only the bounded domain), transient flow reconstruction with the fusion model, and transient flow reconstruction with the fusion model combined with an adaptive diffusion coefficient to compensate for measurement and reconstruction errors.

8.3.2.1 Simple bay

Since the objective was to evaluate the methodology under highly dynamic flow conditions, a synthetic scenario was designed with an evolving flow over a period of 9 hours (32400 seconds), featuring significant variations in both direction and magnitude to challenge the reconstruction accuracy. Therefore, Figure 8.14 presents the temporal evolution of this referent flow during this period, highlighting the complexity of the flow patterns that the reconstruction seeks to replicate. Although such pronounced flow changes are unlikely to occur over short timescales in natural environments, the synthetic scenario allows for testing the method's robustness and adaptability under evolving boundary conditions.

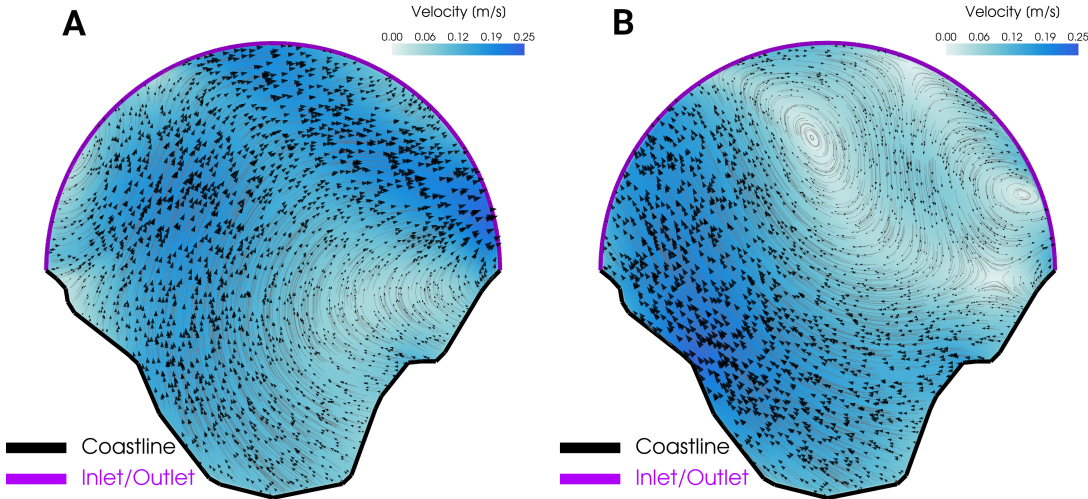


Figure 8.14: Figure shows one example of the evolving referent flow in the synthetic Simple Bay case after 9 hours (32400 seconds), comparing the initial flow state (A) with the final state (B).

A comparison of already mentioned reconstruction approaches and their influence on passive scalar advection is presented in Figure 8.15. Given the time-dependent nature of the referent flow, the steady fit approach (**B**), which uses only the initial 15 drifter measurements to reconstruct the flow and then advects the passive scalar over 32400 seconds without further updates, results in substantial inaccuracies, yielding zero percent overlap with the referent scalar field. Similarly, the bounded domain transient fit approach (**C**), based on reconstructing the referent flow at each T_s interval using repeated steady state optimizations, also fails to capture the complexity of the evolving referent flow, mainly due to limitations imposed by the bounded domain. This approach also results in zero percent intersection. Furthermore, after 32400 seconds, only four drifters remain within the domain, limiting the availability of data and further reducing reconstruction performance.

To address this issue, the fusion model was included in the fitting procedure (**E**), significantly improving flow accuracy and achieving an 86% intersection. Additional refinement using an adaptive diffusion coefficient (**F**) with the fusion model further improved the result, reaching 90% intersection with the referent scalar field by the end of the simulation.

The success analysis (**D**) illustrates the effectiveness of each approach in capturing the passive scalar field. Moreover, the most effective approach, which integrates the fusion model with adaptive diffusion, achieved the highest intersection percentage while maintaining a balanced tradeoff between coverage and overestimation, resulting in the most accurate reconstruction of the passive scalar field.

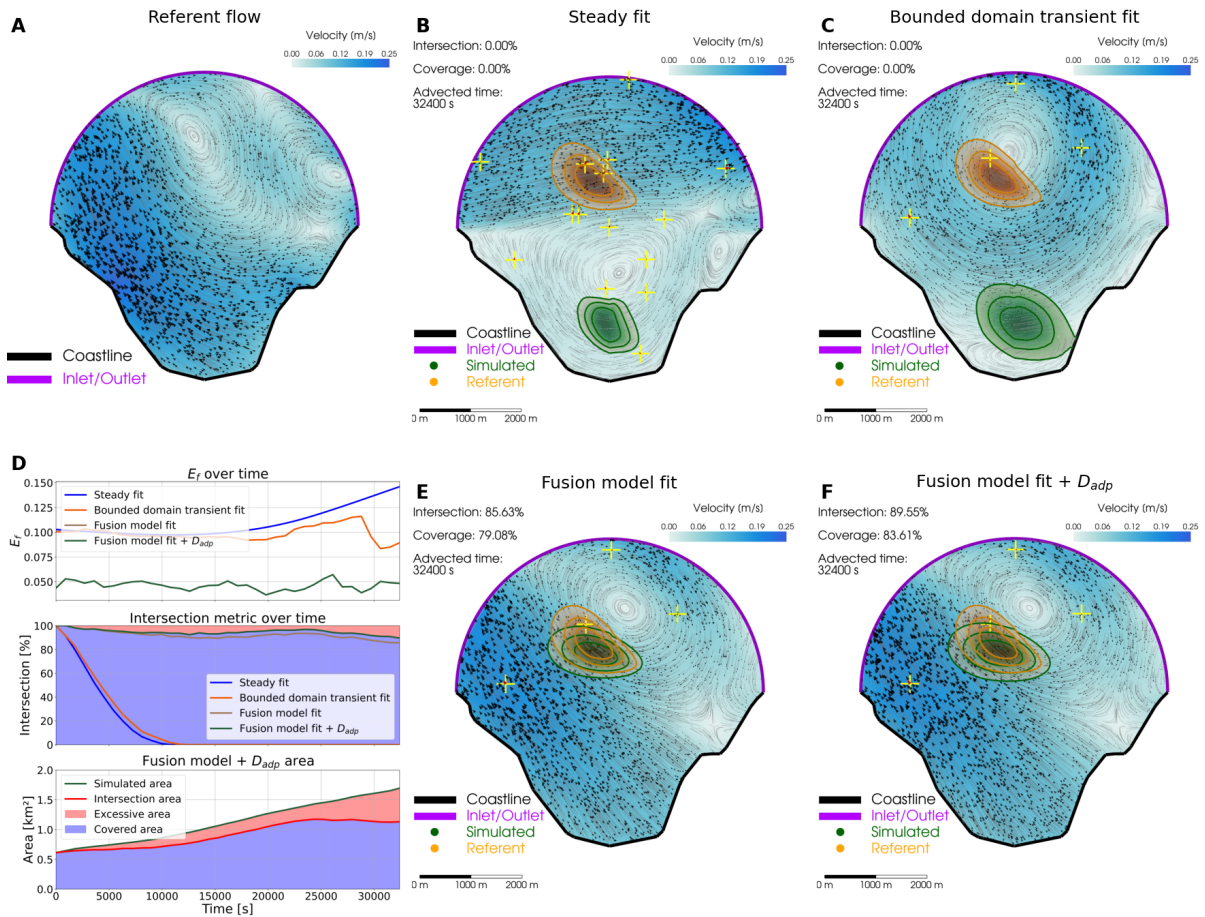


Figure 8.15: (A) Referent flow after 32400 seconds. (B) Steady reconstruction from 15 drifter measurements. (C) Reconstruction with periodic measurement updates without fusion model. (D) Analysis of proposed metrics for passive scalar advection. (E) Reconstruction with measurement updates and a fusion model. (F) Reconstruction with measurement updates, fusion model, and adaptive diffusion compensation.

8.3.2.2 Unije Channel

To test the proposed methodology in a real-world setting, the Unije Channel near the island of Lošinj, covering an area of 96.5 km^2 , was selected. The domain contains four separate inlet and outlet regions, which contribute to complex and variable flow behavior. Unlike the synthetic case, the realistic domain captures naturally occurring variations driven by environmental influences, offering a more demanding scenario for testing flow reconstruction accuracy. These spatial and temporal variations in surface flow can be observed in Figure 8.16.

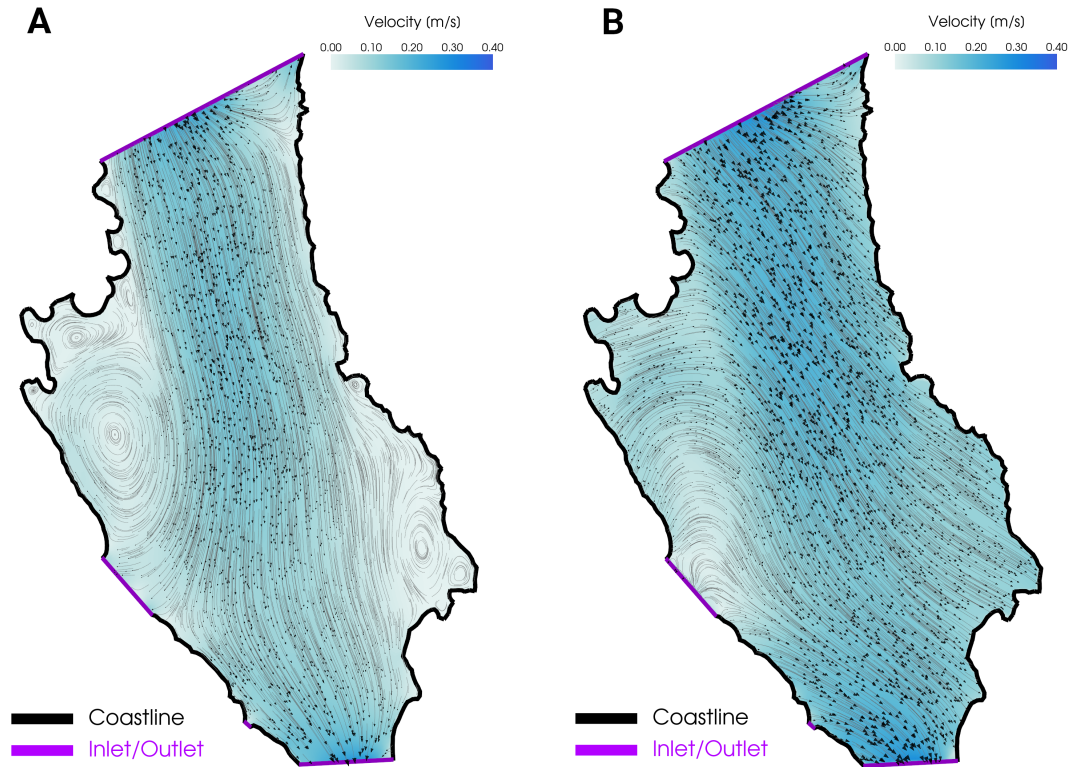


Figure 8.16: Evolution of the referent flow in Unije Channel after 10 hours (36000 seconds), showing the initial (**A**) and final (**B**) states with four inlet and outlet areas.

To showcase how well the method performs in realistic domains, Figure 8.17 presents a comparison of four different flow approximation techniques and their corresponding passive scalar advection results. Similar to the synthetic scenario conducted in 8.3.2.1, both the steady fit (**B**) and bounded domain transient fit (**C**) struggled to accurately reproduce the movement of the referent passive scalar. Interestingly, the bounded domain transient fit in this case produced even less accurate results than the steady fit, highlighting that optimization can sometimes lead to incorrect outcomes. By integrating the fusion model (**E**) into the transient fitting process, the reconstruction accuracy improved substantially, reaching nearly 93% overlap with the referent passive scalar field after 10 hours (36000 seconds). Introducing an adaptive diffusion coefficient (**F**) further enhanced the results, achieving a 94% intersection and full coverage of the scalar field.

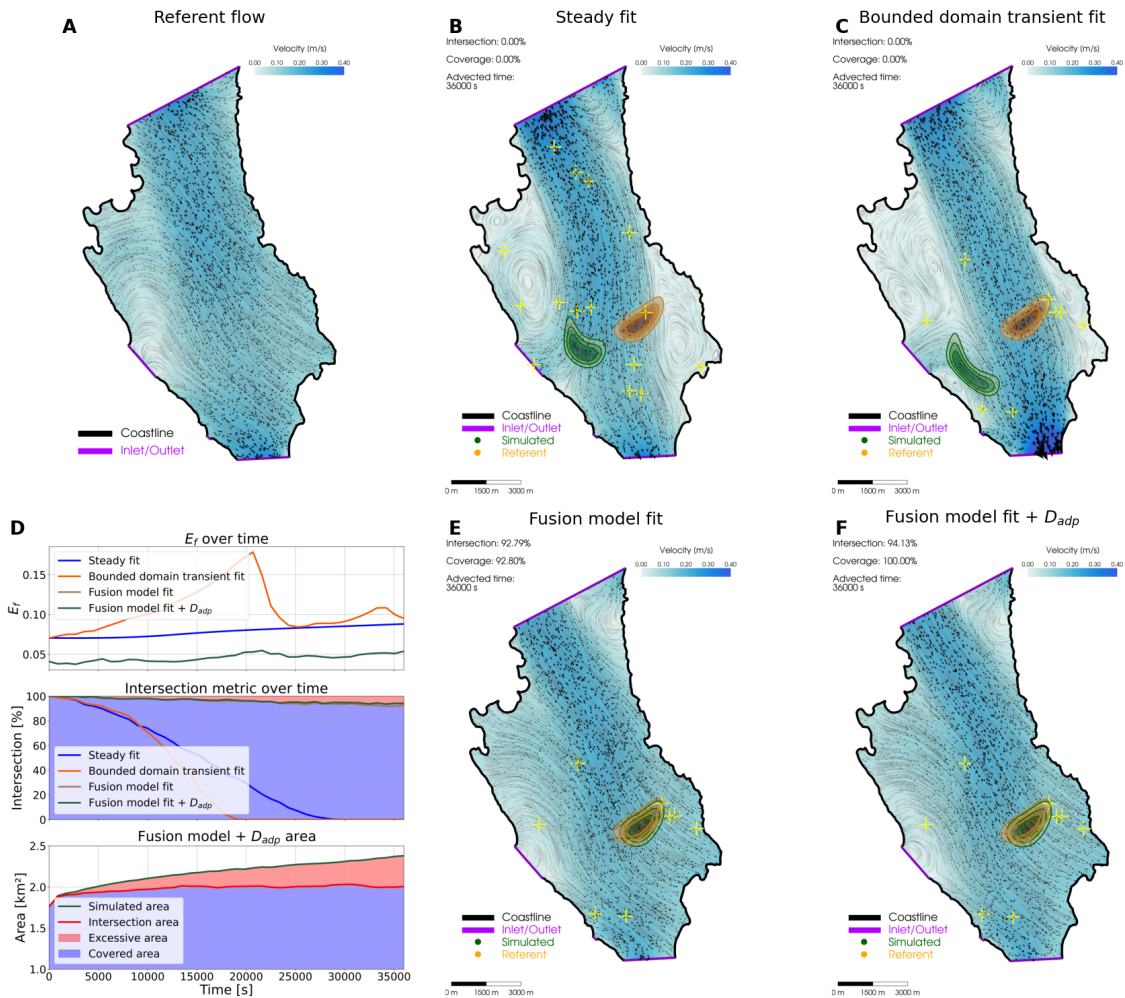


Figure 8.17: (A) Referent flow after 36000 s. (B) Steady reconstruction from 15 drifters with no overlap of the passive scalar. (C) Transient reconstruction showing an even larger mismatch. (D) Analysis of proposed metrics for passive scalar advection. (E) The fusion model achieves high accuracy. (F) The fusion approach and adaptive diffusion closely match the referent passive scalar field.

The success analysis (D) shows a modest improvement with the addition of the adaptive diffusion coefficient and an unexpectedly better result from the steady fit compared to the transient fit. Additionally, the top-performing approach, which combines the fusion model and adaptive diffusion, includes some overestimated areas. Nevertheless, the coverage metric suggests that this excess region contains only a negligible amount of passive scalar, likely due to numerical errors, and can therefore be ignored when predicting the main passive scalar distribution.

9 EXPERIMENTAL RESULTS

After validating the approach in a simulation environment, additional experimental validation in a real environment was carried out in multiple field experiments in the Kvarner region near Rijeka, Croatia. To enable this, suitable and reliable equipment was first acquired to match the requirements of the methodology. This included setting up a complete system for sensor deployment, data acquisition, flow reconstruction, and finally, advection simulation based on the reconstructed surface flow derived from point measurements.

This chapter is divided into the following sections: Section 9.1 describes the selection and configuration of the measurement and transmission system used in conducted deployments. Section 9.2 presents the preliminary sea experiment conducted in a small bay, aimed at validating steady flow reconstruction and evaluating the system's velocity, GPS, and drifting accuracy. Section 9.3 addresses transient flow reconstruction in a larger domain, focusing on how the measurement period impacts reconstruction accuracy. Lastly, Section 9.4 demonstrates an integrated scenario combining transient flow reconstruction with autonomous UAV search, highlighting the framework's practical application in a search task.

9.1 Equipment and preparation

For experimental validation of the proposed methodology, in-situ sea surface velocity measurements were obtained using commercially available equipment, as described in Section 3. To support near-real-time reconstruction of flow fields across multiple submesoscale domains, the measurement system was required to provide accurate and frequent data under varying spatial and temporal conditions. Standard technologies, such as HF radar systems, are effective in fixed coastal areas but lack mobility and are very expensive, while satellite-based alternatives offer wide spatial coverage but come with high costs and insufficient temporal resolution for frequent updates.

To tackle these issues, GPS-tracked drifters were chosen. These devices are floating buoys that are equipped with sensors, which record and transmit surface velocity. Floating buoys are

equipped with sensors that measure and transmit surface velocity data. This method offers a mobile, scalable, and relatively low-cost solution for dynamic marine environments. Among various options available, drifters that use GSM/GPRS communication stood out as especially beneficial due to their easy deployment, accessible infrastructure, and affordable data plans. However, the selection of these drifters is limited by availability and vendor-specific features. Therefore, to address these limitations, particularly for reliable offshore communication in real time, the Automatic Identification System (AIS) was selected as the primary method for obtaining measurements. This system is originally created for maritime navigation and vessel tracking, but is now commonly used in many oceanographic applications [181]. AIS is actually a mandatory maritime transponder network that continuously broadcasts vital vessel information, such as identity, position, course, and speed, to nearby ships and shore stations. Its primary purpose is to enhance safety, prevent collisions, and support vessel traffic management and maritime domain awareness [182]. An example of possible AIS messages is shown in Table 9.1.

Table 9.1: Overview of AIS message types.

Message	Description	Example Applications
Type 1	Position Report Class A	Live location data for Class A vessels
Type 5	Static and Voyage Information	Identification and voyage specifics
Type 8	Binary Broadcast Message	Custom data transmissions for specialized uses
Type 18	Standard Position Report Class B	Live location data for Class B vessels
Type 22	Channel Management	AIS frequency and channel coordination
Type 24	Static Data	Key vessel identification details
Type 27	Long-Range Position Report	Extended distance position updates

Although such AIS transponders are primarily designed as fixed-mounted equipment for small vessels, they were repurposed for buoy-based oceanographic monitoring in this research. Therefore, 14 units of the Alltek Marine Electronics Corp (AMEC) TB-560 [94] tracking beacon model were acquired and mounted on custom floating buoys. The combination of these TB-560 beacons with the buoys created custom drifters equipped with GPS and surface velocity sensors. This method of monitoring sea surface velocity allows for analyzing drift patterns, forecasting trajectories of drifting objects or persons, and identifying the most promising search areas. Such information is particularly suitable for experimental validation of the proposed methodology.

It should be noted that each tracking beacon is paired with a specific mounting bracket and was therefore labeled sequentially from 1 to 14, as shown in Figure 9.1. Once a TB-560 beacon is activated with a clear view of the sky, it typically obtains a GPS fix within one minute.



Figure 9.1: Labeled AMEC TB-560 tracking beacons (left) and AMEC Cypho-150 AIS receiver with VHF antenna (right), used for receiving AIS transmissions.

Configuring the AMEC TB-560 involves programming parameters to tailor its operation for the study. This includes setting the transmission frequency, vessel identification (MMSI and name), and other settings to ensure accurate AIS broadcasts using AMEC software.

The last step in the equipment setup procedure involves receiving and decoding the AIS signals broadcast by the AMEC TB-560 tracking beacons through an AIS receiver. For this purpose, the AMEC Cypho-150 receiver was employed, as illustrated on the right side of Figure 9.1. It comes equipped with a VHF antenna and dedicated software. This receiver allows us to accurately capture AIS transmissions from vessels within a range of approximately 40–50 nautical miles (70–90 km). Before deploying the tracking beacons at sea, it was essential to confirm their signal transmission and verify reception with the receiver. Therefore, an initial field test was conducted on land. The left part of Figure 9.2 shows AIS messages received from multiple vessels within range, containing coded information including vessel position, identity, course, speed, and other relevant data.

The decoding of these messages was performed using the Python library `pyais` [183], which supports both encoding and decoding of AIS data, enabling the extraction of essential information from the received messages. As the receiver captured AIS signals from vessels beyond the

purchased tracking beacons, a Python-based filtering script was implemented to extract only messages with MMSI numbers corresponding exclusively to the deployed beacons (lower part of Figure 9.2).

```

!AIVDM,1,1,,A,33-jmV5000126k@IsoeGIFRF0000,0*3D
!AIVDM,1,1,,B,402AaJ1vP0e>Q26fNIskFG0005:,0*32
!AIVDM,1,1,,B,13STF80P00Q22uLIsbpf4?VH20Rq,0*0C
!AIVDM,1,1,,A,D02AaJ1itNfp0006DBd06D0,2*6A
!AIVDM,1,1,,B,D02ANS1qhN? T0N01rhN000,2*4B
!AIVDM,1,1,,B,13SSk`PP00Q25<VIs1fIKOVN05`p,0*60
!AIVDM,1,1,,B,13SLTN5001Q22bNIskcv2PjJ088a,0*4F
!AIVDM,2,1,4,A,55Solr42DD@<PuIJ220=U18E=>0598uN
!AIVDM,2,2,4,A,888888888880,2*20
!AIVDM,1,1,,B,402ANS1vP0e>@<tsF014Q@00<0h,0*7C
!AIVDM,1,1,,A,13SmFJ7P00Q23DDIsoe@0?VR2H:6,0*0C
!AIVDM,1,1,,A,13S3V10P1M122=FIscgKJ0VT08:o,0*07
!AIVDM,1,1,,A,H02AaJ0hf18T`Dd400000000000,2*23
!AIVDM,1,1,,A,13SSk`PP00Q25<VIs1fKv0vf00SJ,0*58
!AIVDM,1,1,,A,402AaJ1vP0e>FQ26fNIskFG00D2?,0*5B
!AIVDM,1,1,,A,13STF80P00Q22uLIsbpf4?vd25`p,0*15
!AIVDM,1,1,,B,33SDd;5P00122HjIswBh0?vf0Ddb,0*11
!AIVDM,1,1,,A,13SLTN5001Q22bNIsk<umPjh0H?E,0*7B
!AIVDM,1,1,,A,402ANS1vP0e>J<tsF014Q@0008?J,0*5C
!AIVDM,1,1,,B,13SmFJ7P00Q23DDIsoeP0?vp2L0d,0*61
!AIVDM,1,1,,B,331Sw85000Q25i>Is1RV<H`l0Dg:,0*72
!AIVDM,1,1,,B,13S3V10P1M1223nIsdAckOvp08@o,0*74
!AIVDM,1,1,,B,D02AaJ1UHNfp0006EFH06D0,2*60
!AIVDM,1,1,,A,D02ANS1=tn?a`N01sDN0170@00,2*26
!AIVDM,1,1,,B,13STF80P00Q22uLIsbpf4?vv28Bo,0*32
!AIVDM,1,1,,B,H02AaJ0hf18T`Dd400000000000,2*20
!AIVDM,1,1,,B,13SSk`PP00Q25<VIs1fI0hm20@C@,0*47
!AIVDM,1,1,,B,402AaJ1vP0e>PQ26fNIskFG0005:,0*5E
!AIVDM,2,1,5,A,531SN882?IgcTQDKr2059@01U>222222
MMSI: 999123001 A0SeR Drifter 1 LAT: 45.33737 LON: 14.424983 Vx: 0.0 Vy: 0.0
MMSI: 999123008 A0SeR Drifter 8 LAT: 45.337307 LON: 14.425002 Vx: 0.0 Vy: 0.0
MMSI: 999123008 A0SeR Drifter 8 LAT: 45.337307 LON: 14.425008 Vx: 0.0 Vy: 0.0
MMSI: 999123008 A0SeR Drifter 8 LAT: 45.33741 LON: 14.425105 Vx: 0.0 Vy: 0.0
MMSI: 999123001 A0SeR Drifter 1 LAT: 45.337347 LON: 14.425028 Vx: 0.0 Vy: 0.0
MMSI: 999123008 A0SeR Drifter 8 LAT: 45.337257 LON: 14.425072 Vx: 0.0 Vy: 0.0
MMSI: 999123001 A0SeR Drifter 1 LAT: 45.337353 LON: 14.424995 Vx: 0.0 Vy: 0.0
MMSI: 999123008 A0SeR Drifter 8 LAT: 45.337323 LON: 14.425032 Vx: 0.0 Vy: 0.0
MMSI: 999123001 A0SeR Drifter 1 LAT: 45.337353 LON: 14.424995 Vx: 0.0 Vy: 0.0
MMSI: 999123001 A0SeR Drifter 1 LAT: 45.337347 LON: 14.425028 Vx: 0.0 Vy: 0.0
MMSI: 999123008 A0SeR Drifter 8 LAT: 45.337257 LON: 14.425072 Vx: 0.0 Vy: 0.0
MMSI: 999123008 A0SeR Drifter 8 LAT: 45.337323 LON: 14.425032 Vx: 0.0 Vy: 0.0
MMSI: 999123001 A0SeR Drifter 1 LAT: 45.337347 LON: 14.425028 Vx: 0.0 Vy: 0.0
MMSI: 999123008 A0SeR Drifter 8 LAT: 45.337307 LON: 14.425008 Vx: 0.0 Vy: 0.0
MMSI: 999123001 A0SeR Drifter 1 LAT: 45.337347 LON: 14.425028 Vx: 0.0 Vy: 0.0
MMSI: 999123008 A0SeR Drifter 8 LAT: 45.337257 LON: 14.425072 Vx: 0.0 Vy: 0.0

```

pyais →

Figure 9.2: AIS messages decoded using the Python pyais module

To adapt the AIS tracking beacons for monitoring sea surface velocity, custom buoy platforms were developed to accommodate the mounting of the AMEC TB-560 devices. This required procuring appropriate floating buoys, adding concrete weight to ensure stability, and designing a drogue system aimed at reducing wave- and wind-induced motion. The necessary materials for drifter construction, including mounting brackets and vertical support rods, were acquired. A dedicated ground station was established, consisting of a laptop connected to the AMEC Cypho-150 receiver to capture and process AIS signals from the beacons. After integration of all components, operational drifters capable of recording surface current velocities were successfully assembled. The full workflow for drifter preparation, from initial planning to final configuration, is illustrated in Figure 9.3.

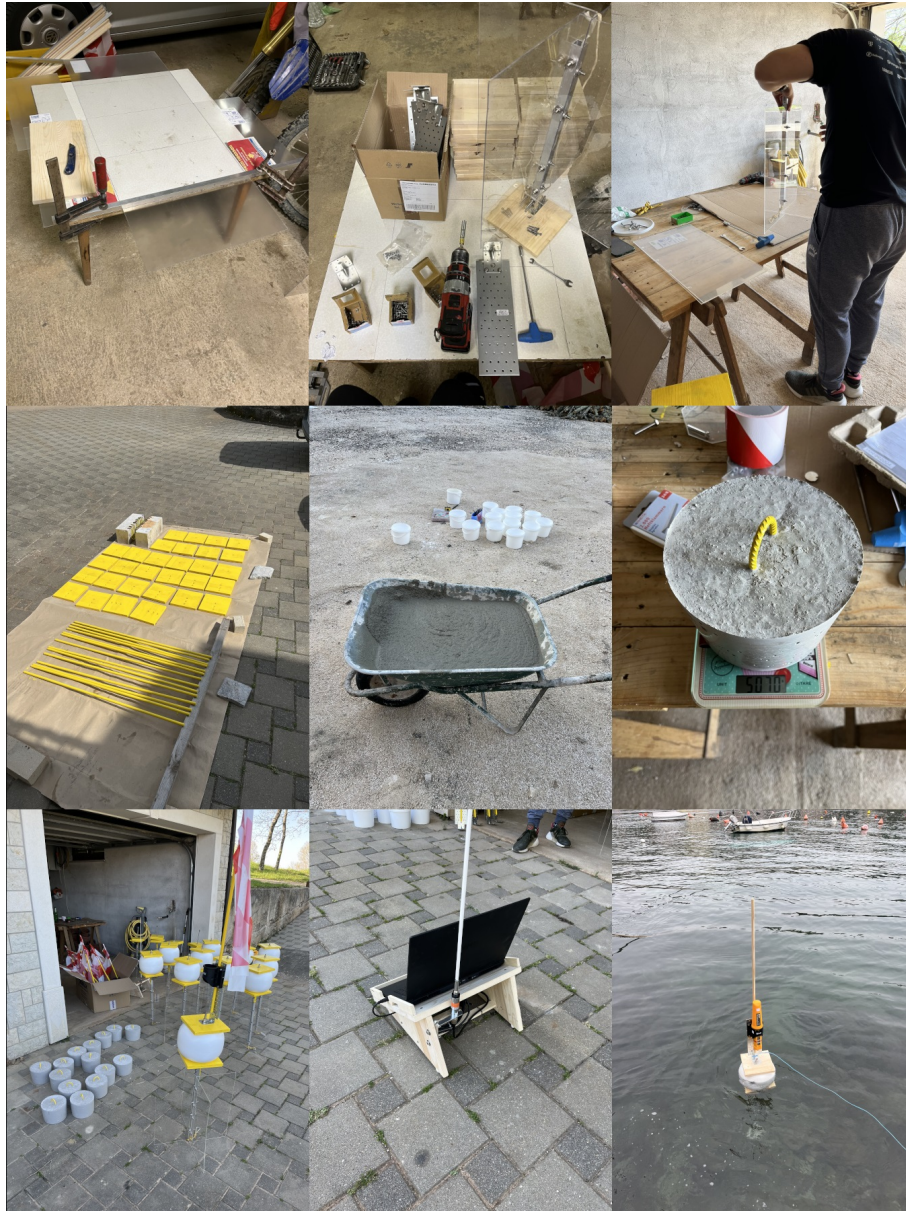


Figure 9.3: Overview of drifter setup: from design and acquisition to final assembly

After the custom drifters were completed and their AIS communication settings configured, buoyancy tests were conducted to verify that each unit floats stably and transmits positional data reliably. Once these verifications were successfully completed, the system was ready for deployment, marking the final step before initiating the first sea experiment.

9.2 Plomin Bay flow experiment

For the preliminary sea experiment and drifter deployment, Plomin Bay, situated in the northern Adriatic Sea on the east coast of the Istria peninsula, was selected. The bay covers approximately 3.5 km² and was chosen for its relatively low maritime traffic and favorable study conditions. Its sheltered waters provide a controlled environment that minimizes the effects of external disturbances such as strong currents and heavy vessel movement, which could otherwise interfere with data quality. Moreover, the bay's compact size facilitates easier tracking and retrieval of the drifters.

The experiment took place on April 15, 2024, and involved deploying drifters at specific locations within the bay. Navigation followed a predefined route to ensure accurate placement of the drifters. Figure 9.4 shows the actual deployment process, along with the workstation setup consisting of a laptop and the AMEC Cypho-150 receiver. This receiver, equipped with a VHF antenna and dedicated decoding software, allowed us to capture the AIS signals transmitted by the tracking beacons.

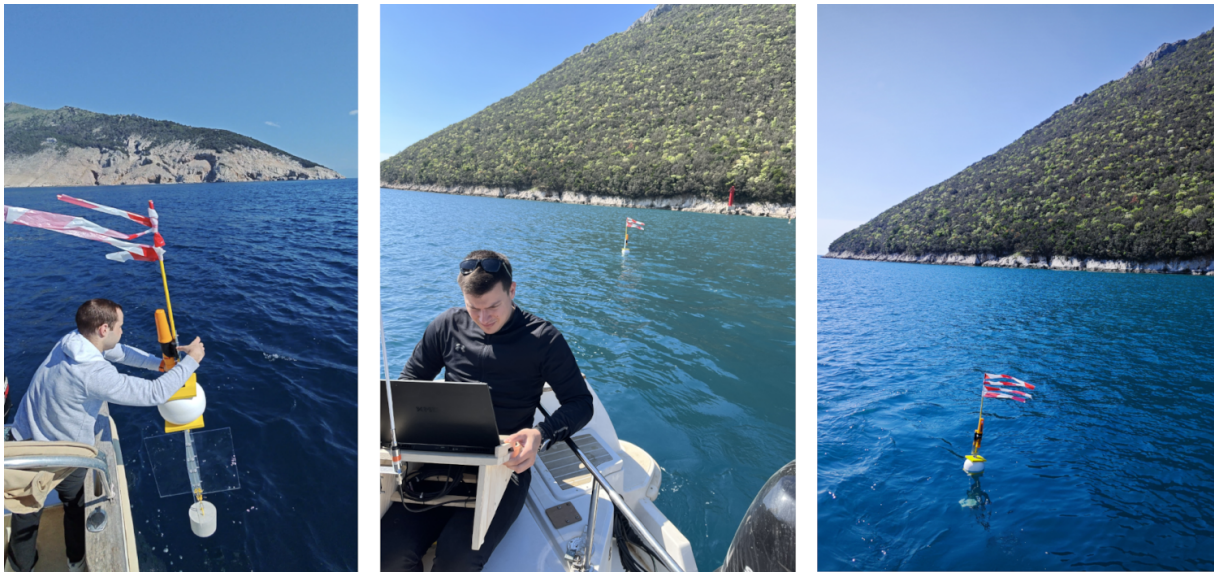


Figure 9.4: Drifter deployment and AIS message reception using the AMEC Cypho-150 receiver

To collect measurements from multiple locations within Plomin Bay, several drifters were manually retrieved and redeployed at different positions. This method enabled us to analyze spatial variations in the data and evaluate the effects of operating with fewer than the full set of drifters. A total of eight drifter deployment configurations were carried out, each differing in duration and the number of active drifters. A summary of the collected AIS messages is given in

Table 9.2. Throughout all deployments, no issues occurred, such as loss of signal transmission or drifters or colliding with the coastline.

Table 9.2: Overview of received AIS messages.

Configuration	Active drifters	Duration [min]	AIS messages
1	8	40	1516
2	8	13	423
3	5	8	112
4	6	12	212
5	8	60	2538
6	5	3	108
7	7	11	470
8	5	21	525

Since drifter configuration 5 had the longest AIS transmission and produced the highest number of received AIS messages, it was selected for a more detailed analysis. Figure 9.5 shows the outcomes of this deployment. On the left side, the figure presents the AIS messages received from each individual drifter, offering a clear view of their spatial distribution and the area they covered within Plomin Bay at that time. On the right side, a steady flow field is reconstructed from one representative time step during the same deployment. The flow inside the bay appears streamlined, with no evident vortex structures. This outcome is expected given the shape of Plomin Bay, which has a narrow and enclosed inlet where lateral movement is constrained. The bathymetry also lacks significant features that typically promote eddy formation, further contributing to the absence of vortices in the reconstructed flow field.

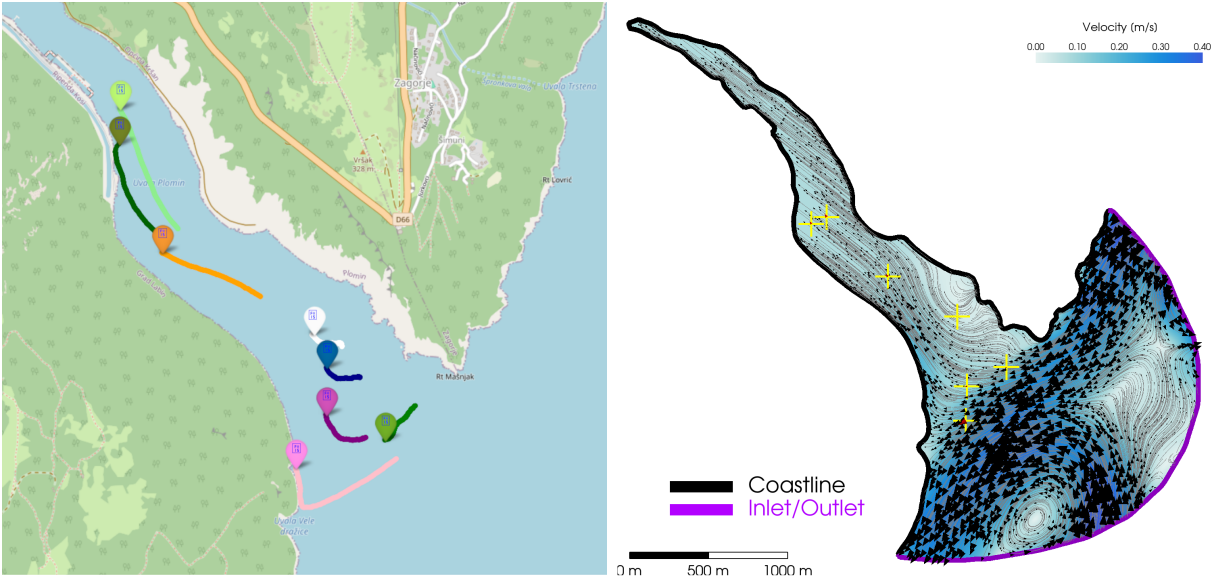


Figure 9.5: Results from deployment configuration 5 with 8 drifters in Plomin Bay. Left: drifter trajectories with final positions marked. Right: reconstructed steady surface flow from a single time step.

It should be noted that, although the drifter trajectories inside the bay are longer than those toward the open sea, the reconstructed velocities appear reversed. This is because the reconstruction represents a single snapshot, while the trajectories correspond to moving drifters, highlighting the limitations of a steady-fit approach for that measurement instance.

Based on the reconstructed flow field shown in Figure 9.5, a comparison was made between the observed drifter trajectories and those generated through Lagrangian particle advection using the steady surface velocity field. The goal was to assess how well a single time step reconstruction can predict drifter motion over time. The outcome of this comparison is illustrated in Figure 9.6, where darker colored lines represent the experimental drifter trajectories, while the corresponding simulated trajectories advected on the reconstructed flow are shown in the same colors with increased transparency for distinction.

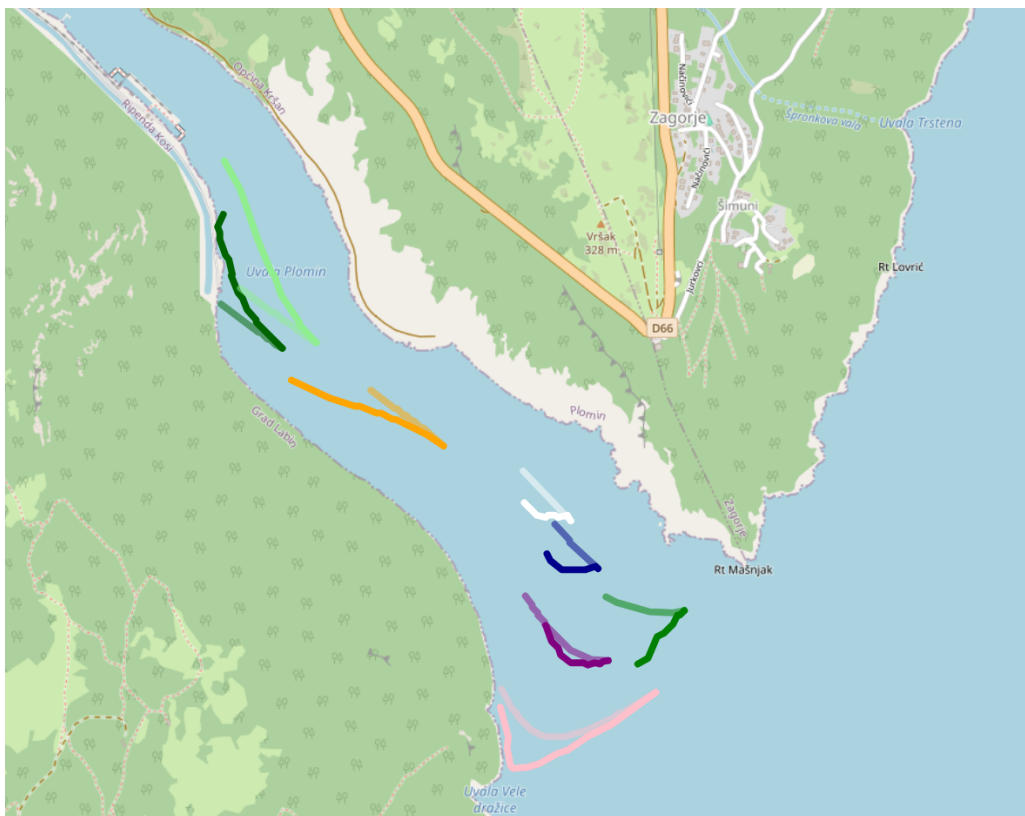


Figure 9.6: Comparison of real and simulated drifter trajectories in Plomin Bay, with dark lines showing observed paths and transparent lines showing 60-minute simulated paths from reconstructed flow.

As shown on Figure 9.6, a notable discrepancy exists between the real and simulated trajectories, further confirming the transient nature of surface dynamics in the bay. A single steady flow reconstruction cannot fully capture the evolving flow field over an extended period, such as 60 minutes. Nevertheless, the reconstruction visually aligns well with the drifter measurements

at that specific time step, indicating that the approximation is satisfactory in the short term. This suggests that employing more frequent flow reconstructions, for example, every 10 to 15 minutes, would likely improve the accuracy of simulated drifter trajectories. While the flow is not expected to vary significantly within such short intervals, substantial changes do occur over the course of an hour. Based on these findings, the next step in the experimental validation was to conduct a deployment in a larger and more dynamic domain, where vortex formation could occur and where high-frequency flow updates would more effectively improve trajectory prediction.

9.3 Valun Bay flow experiment

Based on the findings from the first sea experiment, a second deployment was conducted to further test the reconstruction algorithm's predictive performance. This experiment took place in Valun Bay on the island of Cres, located in the Kvarner region of the northern Adriatic Sea. It involved more frequent flow field reconstruction over a significantly larger domain capable of supporting mesoscale phenomena such as vortex formation. The area, spanning approximately 5 km by 10 km, was chosen for its moderate and stable environmental conditions. While it is more open and exposed than smaller enclosed bays like Plomin Bay, it still provides sufficient natural boundaries to ensure safe deployment and retrieval operations, while enabling the development of more complex and dynamic surface flows.

Given that velocity measurements are recorded every 10 seconds using satellite-based GPS, a certain level of inaccuracy is inevitable due to signal noise and positioning limitations. These short-term fluctuations and GPS noise can distort the drifter trajectories and result in misleading velocity estimates. To reduce the impact of this error, a moving average filter was used on the raw velocity data. For each drifter, the velocity was averaged over 1-minute windows. This method smoothed out high-frequency noise and highlighted consistent movement patterns caused by the underlying flow field.

Before initiating the deployment, it was necessary to design a strategy that would maximize drifter coverage and provide a more complete depiction of surface circulation in Valun Bay. For this purpose, the Halton sequence was employed, a low-discrepancy quasi-random method that provides better spatial uniformity than purely random placement. This enabled a more deliberate distribution of drifters throughout the domain, effectively reducing clustering and

enhancing the mapping of flow patterns. Deployment timing was also planned in advance by considering the vessel's speed and the time required to release each drifter, enabling a well-paced and efficient process. The finalized deployment coordinates obtained using this approach are shown on the left side of Figure 9.7 while the right side of the figure illustrates the actual deployment process, beginning with the loading of drifters at Cres Marina and continuing with the departure toward the predefined release locations in Valun Bay.

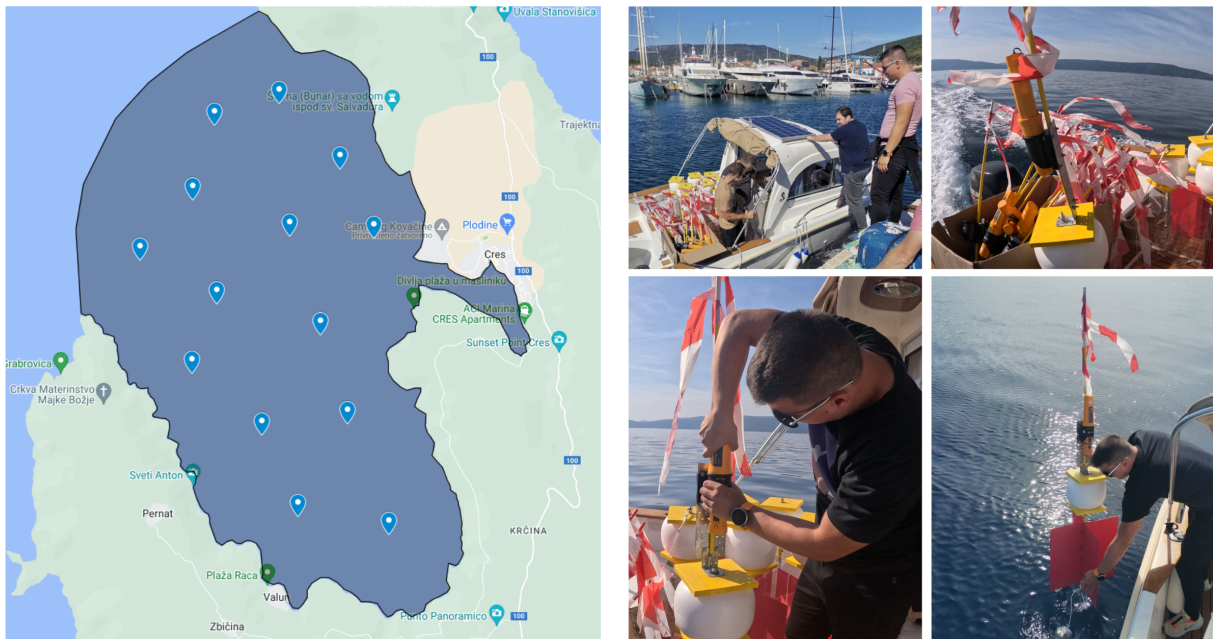


Figure 9.7: Selected deployment locations across Valun Bay, generated using the Halton sequence for improved spatial uniformity (left). Field photos showing the preparation and release of drifters during the experiment (right).

The deployment took place on September 22, 2024, with drifters distributed across the 55 km² bay. The entire deployment process lasted around 1 hour and 30 minutes, with each unit placed at a predetermined location. During the observation period, surface current and wind forecasts were monitored using publicly available sources such as Windy [184], DHMZ [185], and Windfinder [186]. The left side of Figure 9.8 shows the predicted surface flow directions based on these sources, which initially indicated southeastward movement.

However, shortly after deployment, the drifters began to move in a direction opposite to what was forecasted. The right side of Figure 9.8 presents the recorded drifter trajectories. Each path is colored individually to differentiate between units, with dots marking received signal positions and balloon-shaped icons denoting the last known locations.

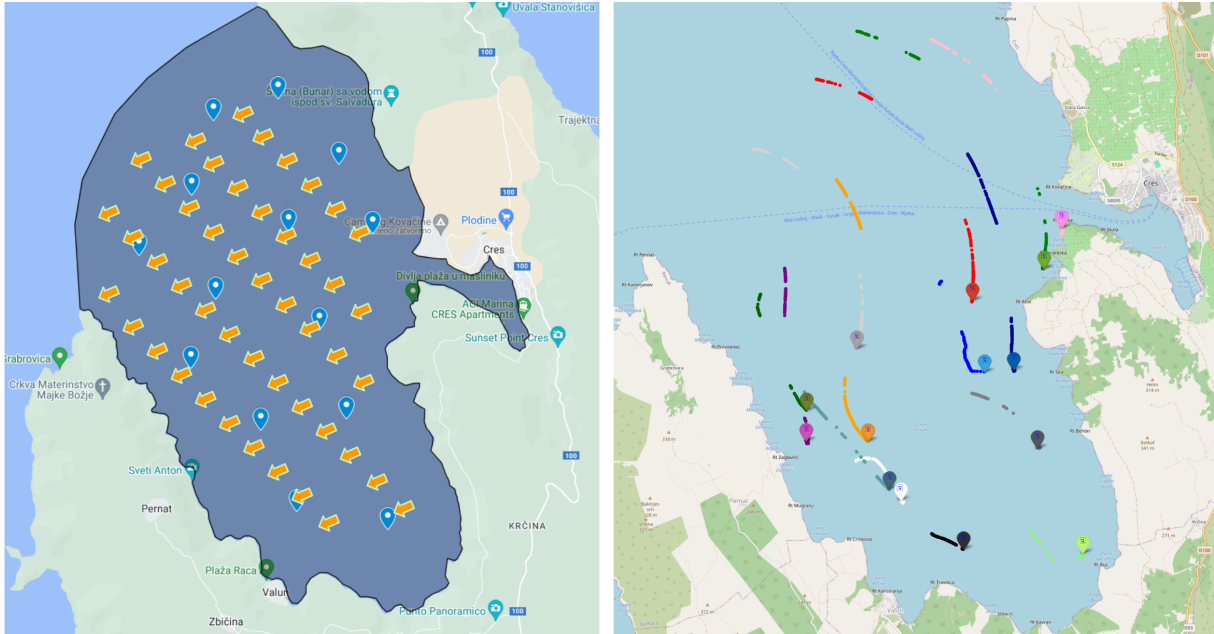


Figure 9.8: Forecasted surface flow direction from publicly available prediction sources (left). Drifter trajectories recorded during the September 22, 2024, deployment where colored lines indicating individual drifter paths.

Although certain segments of the bay exhibit missing data, the general movement trends of the drifters remain evident. These data gaps are likely caused by temporary signal interruptions. Since the receiver AMEC Cypho-150 with antenna was placed on a boat, potential issues include signal loss due to increased distance between drifters and the receiver, as well as the influence of sea conditions. In particular, waves may have intermittently obstructed the line of sight between the antenna and the drifters, further contributing to reduced signal reliability. Despite these limitations, the deployment yielded valuable insights into drifter behavior and flow conditions within the bay.

To replicate the observed drifter trajectories, a representative 2-hour segment of the total 4.5-hour experiment was analyzed. Out of the 14 deployed drifters, 12 were used in this analysis since the remaining two emitted signals while still on the boat, which would have negatively influenced the flow reconstruction. Based on robustness analysis from 8.3.1, drifter positions were sampled every 900 seconds, assuming relatively stable flow conditions during each interval.

As a first step, the method presented in [112] was applied, which considers a spatially uniform wind field superposed on a CFD-based flow model. However, this approach revealed

discrepancies in the southern bay region, where the presence of the surrounding coastline constrains flow and reduces surface velocities. The artificially imposed wind led to overestimated velocities in this semi-enclosed area, producing simulated trajectories that diverged significantly from those recorded during the experiment.

To improve prediction accuracy within this complex flow environment, a fusion-based modeling approach was adopted. The model incorporated new drifter data every $T_s = 900$ s and used those measurements to update the reconstructed velocity field. This iterative process allowed the model to adapt to evolving surface conditions and maintain consistency with real-world observations. The impact of this approach is illustrated in Figure 9.9, which presents the flow field at both the beginning and end of the reconstruction period.

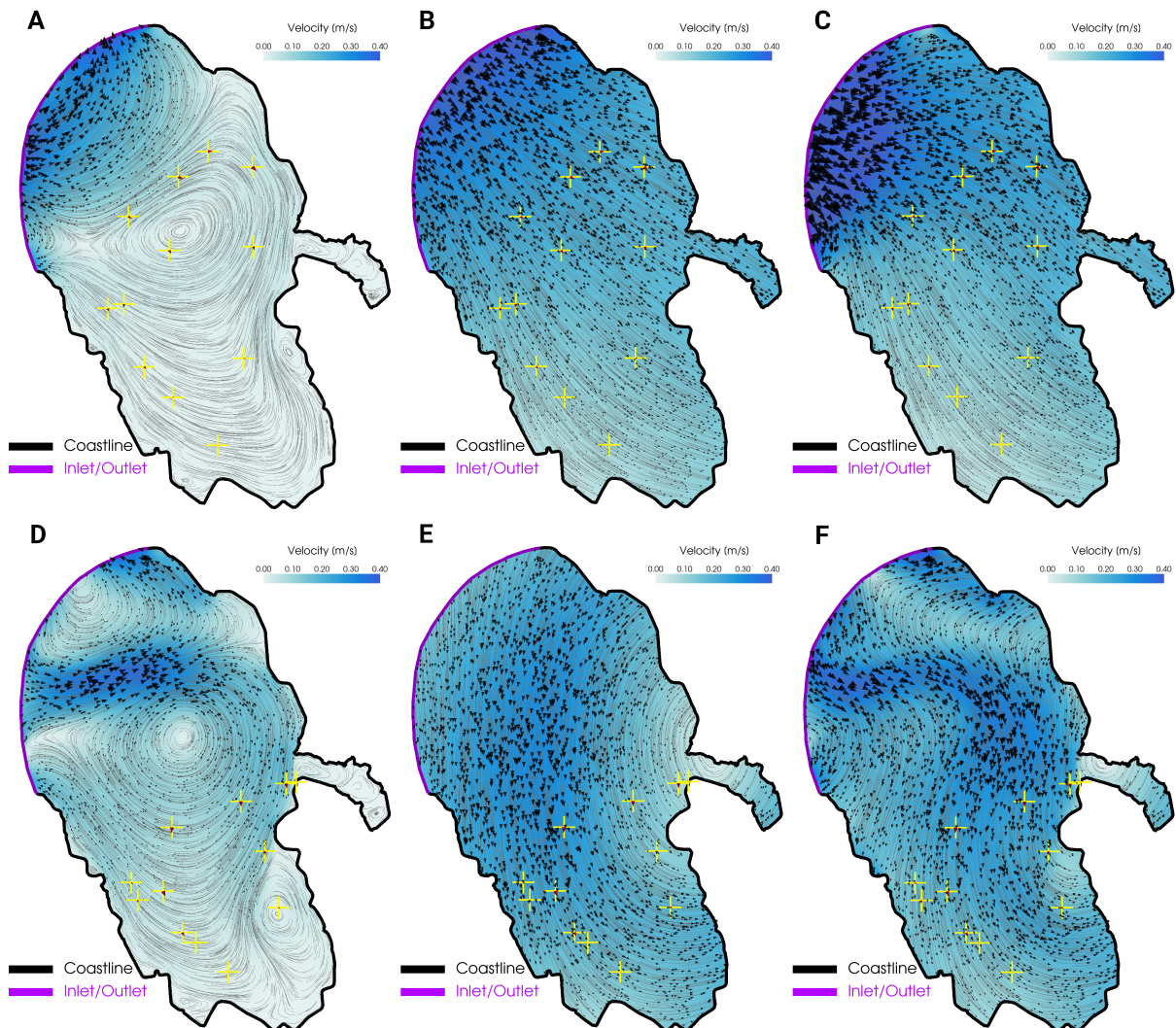


Figure 9.9: Flow reconstruction using the fusion model for the initial $t = 0$ s (A, B, C) and the final $t = 7200$ s (D, E, F) period.

The CFD simulation at $t = 0$ s within a bounded domain (A) shows reduced velocities in

the southern region due to coastal confinement, with initial drifter positions marked by yellow crosses. The flow from the open domain model at the same time (**B**) illustrates stronger northern currents and weaker southern flow due to non-uniform conditions. By combining these, the fusion model at $t = 0$ s (**C**) improves flow representation through integration of bounded and open domain data. At $t = 7200$ s, the bounded domain CFD simulation (**D**) captures temporal changes in flow direction and magnitude based on drifter displacement, while the adjusted open domain flow (**E**) aligns with updated drifter trajectories. The final reconstructed field at $t = 7200$ s (**F**) demonstrates how fusion forcing effectively captures the temporal evolution of surface currents.

Presented results highlight a major limitation of standard CFD simulations, as the bounded domain simulation approach encounters difficulties in producing velocity fields that reflect realistic surface flow patterns, particularly in regions distant from the boundaries. On the other hand, the open domain approximation offers a more flexible framework, introducing non-uniform velocity fields that adapt more closely to observed data. As time progresses, the flexibility of the fusion surrogate model enhances the model's capacity to replicate actual surface conditions.

To assess the reliability of the proposed approach, the drifter paths recorded during the experiment were reconstructed using both the previous method with a fixed wind component from [112] and the updated fusion-based approach. As illustrated in Figure 9.10, the comparison reveals clear differences where the fusion model better follows the curvature of observed trajectories, with several paths closely matching the measurements.

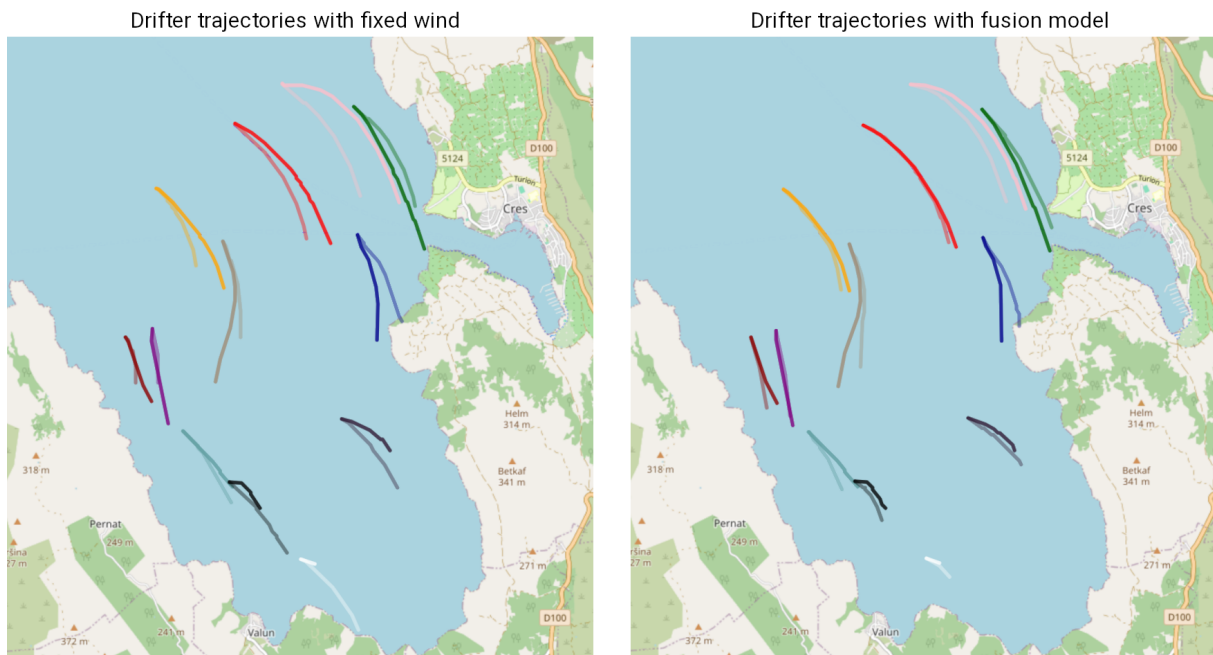


Figure 9.10: The figure compares reconstructed drifter trajectories using a fixed wind approach and the fusion model based on measurements every 900 seconds over two hours. Darker lines show experimental paths, while transparent lines show reconstructed paths.

The fusion model approximation demonstrates a clear improvement, capturing the realistic curvature of drifter trajectories more accurately, especially in the southern area of the domain. In contrast, the fixed wind approximation tends to overestimate surface flow velocities in this region, whereas the fusion model effectively addresses this problem. While many reconstructed trajectories closely resemble the experimental paths, some differences still remain. To evaluate the precision of the trajectory reconstruction, Figure 9.11 shows the reconstruction error, defined as the distance in meters between the reconstructed and observed trajectories.

The results indicate that the steady fit flow model, which advects drifter positions using only the initial reconstructed velocity field, exhibits a wide range of errors, reflecting unstable trajectory predictions. The transient fit approach improves accuracy over longer durations by incorporating updated measurements every 900 seconds. The fusion model further reduces trajectory reconstruction errors, providing a closer match to the observed experimental data. This comparison shows that both the steady and transient fit methods have considerable variability in trajectory errors, with minimum and maximum values spanning a wide range throughout the period. In contrast, the fusion approach, highlighted by the green-shaded area, displays much narrower error bounds, indicating a more stable and reliable reconstruction of drifter trajectories.

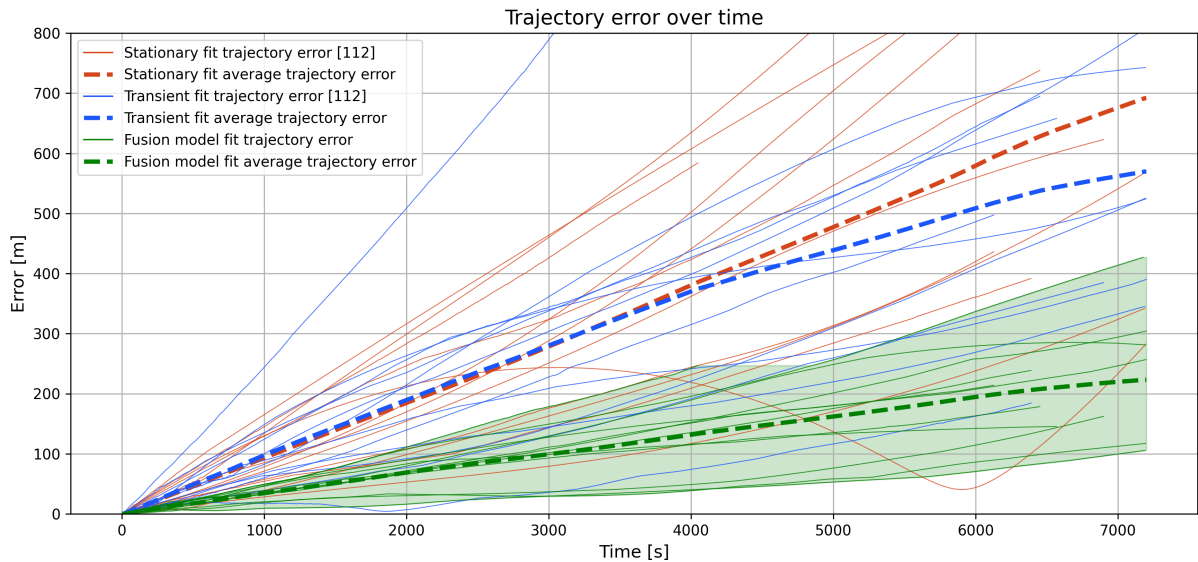


Figure 9.11: Comparison of reconstructed drifter trajectories using steady fit, transient fit and fusion model approach.

9.4 Valun Bay search experiment

Following the successful second sea experiment, which provided valuable results for surface flow reconstruction and drifter trajectory estimation, a third sea experiment, also conducted in Valun Bay, aimed to simulate a realistic search scenario. To recreate such conditions, custom targets were deployed along with drifters to transmit surface flow measurements, while UAVs were tasked with searching for these targets.

Each of the four identical, custom-made targets was constructed from 0.5 x 0.5 meter wooden boards painted yellow to maximize visibility. A one-meter metal rod with marking tape was mounted at each target to further enhance visibility for surrounding vessels. Figure 9.12 shows an example of a deployed target alongside a drifter.

In order to locate the floating targets during the experiment, a commercially available UAV, the DJI Matrice 210 v2, was employed. It was equipped with a DJI Zenmuse X5S RGB camera, capable of capturing high-resolution images at 5280 x 2970 pixels with a 16:9 aspect ratio. An example of the UAV used in the experiment is shown in Figure 9.13.

The idea of this search mission was to conduct autonomous flights using the methodology described in 7.4, where the probability field was updated based on the reconstructed surface flow. To allow autonomous control of the UAVs from a central PC, a dedicated communication system that manages the exchange of commands and telemetry data was implemented. For any flight operation, each UAV must be paired with a remote controller and a tablet running either

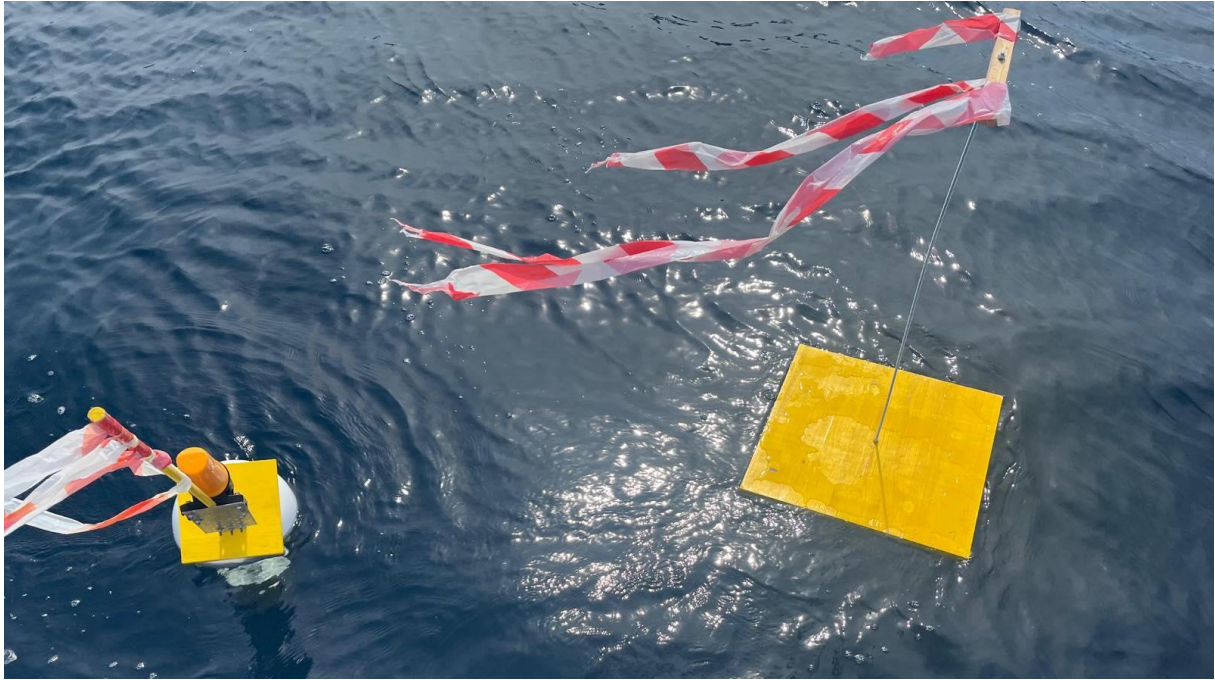


Figure 9.12: Illustration of a deployed target in the experiment.



Figure 9.13: UAV used in this realistic search scenario.

DJI’s official “Pilot” application or a custom app built on the DJI SDK. The UAV communicates with the remote controller via radio signals, and the controller is linked to the tablet through a wired connection.

To enable this communication, a custom Android application was developed. This application connects to the PC server, which generates flight commands and sends them to the UAV. Meanwhile, the UAV continuously transmits status and position updates back to the server, enabling real-time two-way communication. The complete communication architecture is illustrated in Figure 9.14.

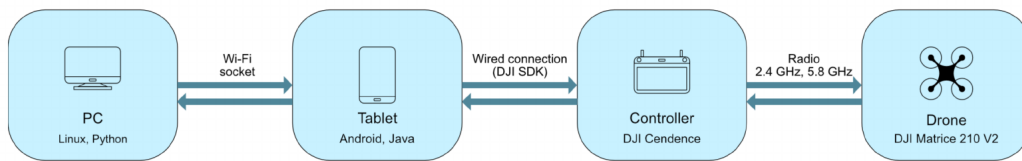


Figure 9.14: Illustration of the communication setup between the PC and UAV [187].

To validate whether targets were successfully located, UAVs captured aerial images every three seconds to detect floating targets, which was the maximum frequency permitted by DJI software constraints. For this purpose, a machine learning model was employed, using a dataset of 522 aerial images collected at altitudes between 60 and 100 meters.

Object detection relied on the YOLOv8 algorithm, initialized with the yolo8l.pt model, previously trained on the COCO dataset. The key metric considered is recall, which measures the proportion of actual targets correctly detected by the model. This metric, used to construct the sensing function, yields a value of $\mu_s = 0.68$ with the default detection confidence threshold of 0.001. Figure 9.15 illustrates detections of sea targets, including the corresponding confidence values with labels.



Figure 9.15: Examples of sea target detections with corresponding confidence levels.

To implement the proposed search methodology, drifter data processing, flow field reconstruction, and UAV operations were integrated within a dedicated search framework, as illustrated in Figure 9.16.

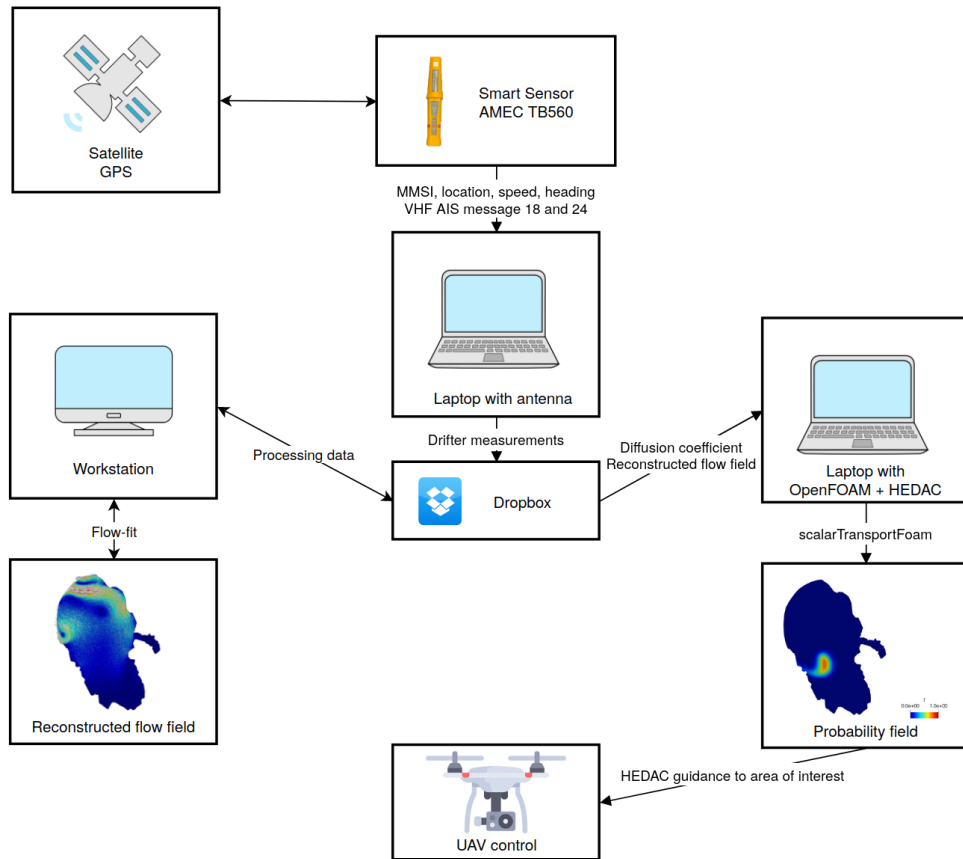


Figure 9.16: Overview of the search framework integrating drifter data processing, flow field reconstruction, and UAV operations to locate objects at sea.

The process starts with a Smart Sensor (AMEC TB560) transmitting real-time information, including its MMSI, location, speed, and heading, via VHF AIS messages 18 and 24. This data is received by a laptop with an antenna receiver and stored as a drifter measurements file in a Dropbox folder. At the same time, a workstation processes the raw data, applies the Flow-fit approach for T_s , and reconstructs the surface flow field.

The reconstructed flow field, along with a diffusion coefficient calculated from the difference between estimated drifter positions and newly received measurements, is then provided to another laptop running a coupled OpenFOAM and HEDAC model. This model advects the probability field using the reconstructed flow and diffusion coefficient through *scalarTransportFoam*. The resulting probability field guides the UAV during the visual search, directing it to areas of interest identified by HEDAC in order to locate the target.

To carry out this search experiment, which took place on June 04, 2025, the team was organized into two groups: one on the vessel, responsible for deploying targets and drifters, and one on land, handling drifter data processing, flow field reconstruction, and UAV operations. In

the previous sea experiment, gaps in drifter data transmission occurred because the receiving antenna was located on the vessel, where signals were frequently interrupted due to distance and wave motion. To address this, the AIS receiver is positioned on an elevated land location rather than on the moving vessel. Additionally, launching and recovering UAVs from the boat was considered highly risky because the vessel was constantly moving. If a UAV needed to return to its takeoff point due to an issue, it would attempt to land at the original launch location, which would no longer be under the UAV due to the vessel's motion, creating a significant safety risk. Therefore, the land group operated from the base station on the central part Valun Bay's eastern coast, at an elevation of 85 m, offering an unobstructed view of the search area and reliable signal coverage from both UAV and drifters. Figure 9.17 provides a view of the experiment base station and the area around Valun Bay.



Figure 9.17: Base station with a view over the Valun Bay search area.

The search experiment began with the deployment of 12 drifters in the domain, with 4 evenly spaced throughout the bay, 5 placed near the target site to improve the accuracy of the flow field reconstruction, and the remaining 3 used solely for observational purposes. The area for target deployment was defined within a circle of 300 m radius, located approximately 1.4 km to the west of the base station. Four targets were arranged in a cross formation, with each positioned roughly 120 m from the central point. The deployment of targets was completed at 10:15 AM, marking $t = 0$, with all targets successfully placed within the designated area. An example of

a deployed sea target along with the corresponding reconstructed flow at that time is shown in Figure 9.18.

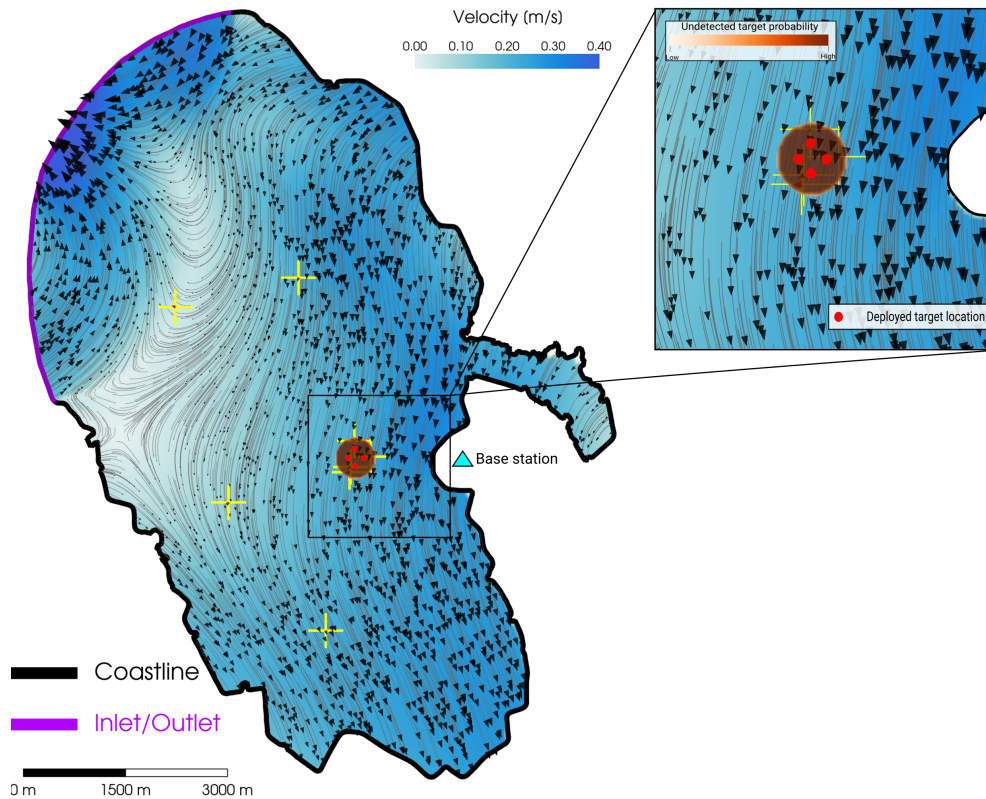


Figure 9.18: The search area with the reconstructed flow field, deployed target positions, and undetected target probability field at $t=0$.

To simulate a realistic search scenario, in which targets drift from their initial locations, a delay in the search start was introduced. Since the targets were not equipped with GPS devices, their positions after the 30-minute delay were estimated using Lagrangian particle advection as described in (6.10). Figure 9.19 depicts the estimated target positions at the start of the search, the estimated trajectories during the 30-minute delay, and the advected probability of undetected targets.

The actual search began with the UAV being manually guided to the offshore starting location within the search domain, after which it proceeded autonomously. Autonomous control was then applied with a constant velocity of 8 m/s and a constant altitude of 75 m. For probability area exploration, the sensing interval Δt_s and the control interval Δt were set to 3 s, while the HEDAC parameters were assigned values of $\alpha = 5000$ and $\beta = 0.1$. During this mission, the probability of an undetected target within the UAV's Field of View (FOV) was discretely

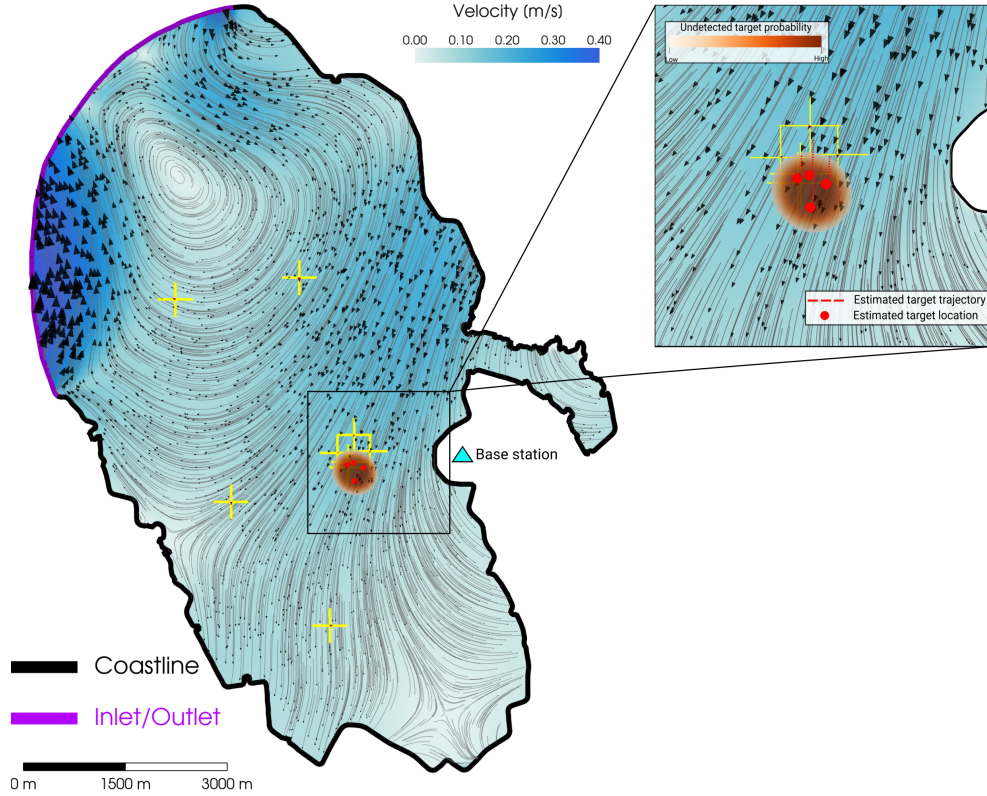


Figure 9.19: The reconstructed flow, probability of undetected targets, and estimated target positions at the start of the search, including their estimated trajectories after the 30-minute delay.

reduced at each captured image, based on the recall of the detection model. The probability field is therefore updated as:

$$s_{i+1} = \begin{cases} s_i(\mathbf{y})(1 - \mu_s), & \text{if } \mathbf{y} \in \text{UAV FOV}, \\ s_i, & \text{otherwise.} \end{cases} \quad (9.1)$$

Following the completion of the search, the captured images were analyzed using the detection model to identify targets. Each detected target's position was calculated based on the UAV's location at the time of image capture and the position of the target label within the image. Figure 9.20 illustrates the search outcome, showing the UAV trajectory, locations of detected targets, estimated target positions and trajectories from $t = 0$, as well as the probability distribution of undetected targets.

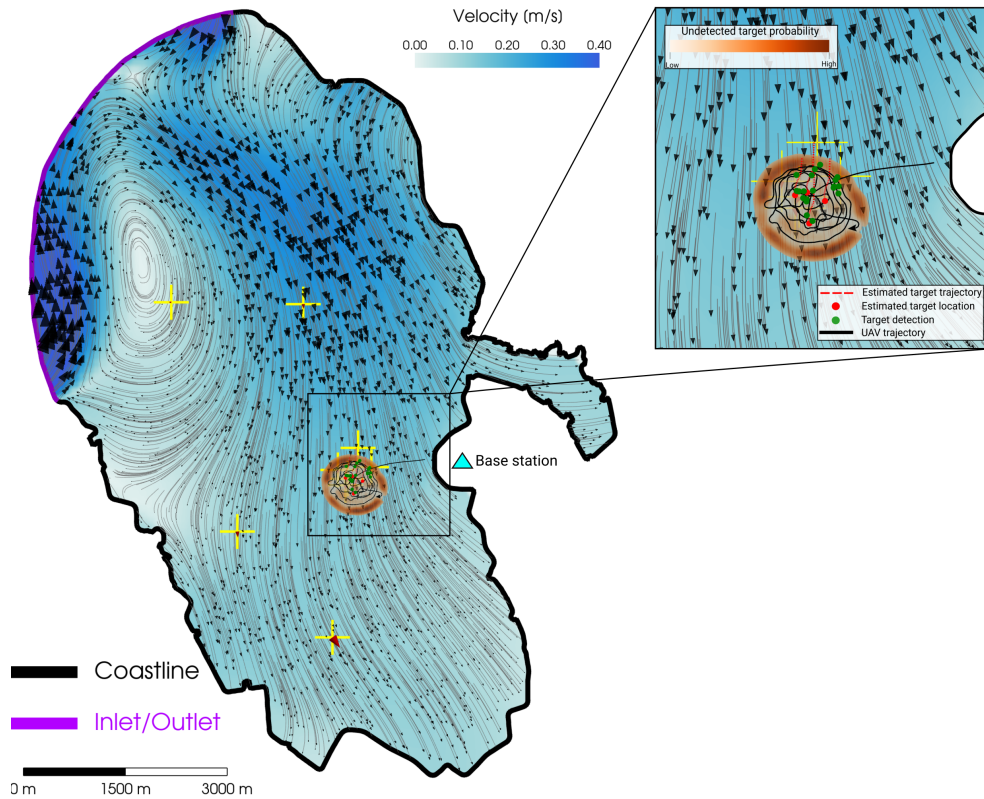


Figure 9.20: The reconstructed flow, probability of undetected targets, the UAV trajectory, detected target locations, and the estimated target positions and trajectories at the end of the search.

It should be noted that detections and their recorded positions occurred at different times throughout the search and therefore may not exactly match the estimated target positions shown for the final state of the search. The few detections located on the right are assumed to correspond to the rightmost target, even though its estimated trajectory does not perfectly align with these observations. Such a discrepancy indicates that the flow field approximation contains inherent inaccuracies, which are accounted by using an adaptive diffusion coefficient. These inaccuracies are quantified by the E_d error of the 9 drifters included in the optimization process, the E_f error of the 3 drifters placed along the targets only for observation, and the corresponding diffusion coefficient, as presented in Figure 9.21.

The use of an adaptive diffusion coefficient confirms that the diffused probability field compensates for uncertainties in both the flow reconstruction and the GPS measurements (positional uncertainty up to 2.5, as specified by manufacturer). As the UAVs explored these areas, they successfully detected targets multiple times, demonstrating that the diffusion-based approach effectively accounts for both modeling errors and measurement limitations.

Since the deployed targets lacked GPS trackers, it was not possible to reliably associate

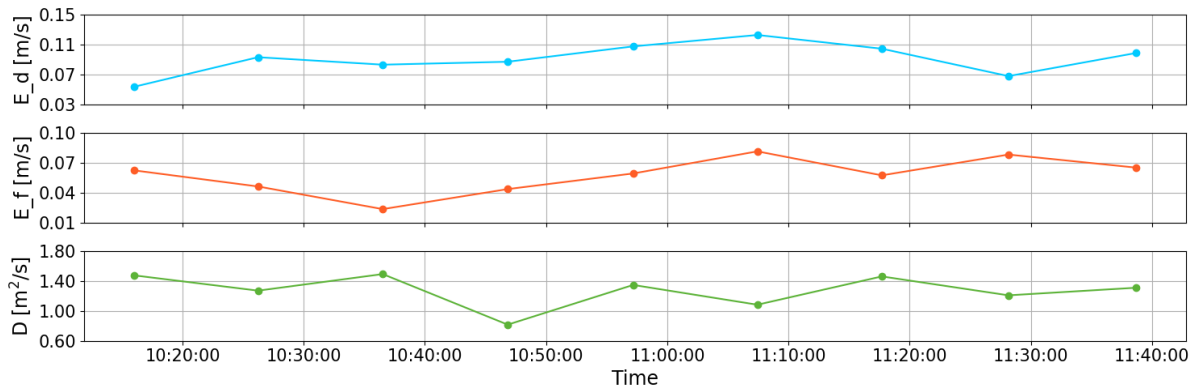


Figure 9.21: Reconstruction errors based on drifter velocity and position, from the beginning to the end of the search.

detections with specific targets. Nevertheless, by examining the estimated target trajectories together with the detected locations and assuming that each detection corresponds to the closest trajectory, it is clear that all targets were successfully detected. The probability field closely matched the target distribution, and at least one target was detected outside its estimated trajectory, providing further confirmation of the effectiveness of the adaptive diffusion approach.

10 LIMITATIONS AND DISCUSSION

This methodology combines two simplified two-dimensional steady flow models to approximate submesoscale sea surface flow, using a quasi-steady approach in which sea surface velocity measurements are continuously updated to improve the accuracy of the reconstructed velocity field. This approach serves as a basis for the advection of particles or objects, as well as passive scalar transport and diffusion, making it suitable for modeling and predicting target probability density dynamics.

Because the model needs to remain fast for near real-time applications, an appropriate resolution of the computational mesh is crucial, as it strongly affects computation time. Since refining the mesh offers little advantage in this context, a coarse grid was chosen to reduce computational cost, even though it limits the ability to capture fine-scale details. Mesh sensitivity tests additionally confirmed stable convergence and provided clear error margins. As a result, the model is less capable of resolving localized flow structures, which can be critical in coastal settings or when precise trajectory prediction is required. Although the use of finer meshes is not excluded, it is important to acknowledge the numerical trade-offs and the significant increase in computational demand they involve. Additionally, the model deliberately omits factors such as bathymetry, the vertical component of flow, transient effects, and the Coriolis force to maintain computational efficiency. These omissions are addressed by the fusion model through an open-domain flow approximation, thereby balancing computational speed with predictive accuracy. The two-dimensional flow assumption constrains the model's applicability in scenarios where vertical flow structures substantially influence horizontal transport. Furthermore, although innovative, the approach may produce unrealistic velocity patterns near the coastline. While similar anomalies have been documented in similar studies, they can affect the reliability of predictions in near-coastline regions. It is important to emphasize that, as a surrogate model, the proposed method is not designed to provide absolute accuracy, but rather a level of precision acceptable within the established computational and operational constraints.

One of the main limitations of the proposed approach is that, over time, it can accumulate

errors. Trajectory discrepancies arising from imperfections in the velocity field are not corrected between optimization windows, causing deviations to grow progressively and leading to increasingly divergent predictions. Moreover, the methodology has only been evaluated for velocities up to 1.5 m/s, leaving its performance under higher or more variable flow conditions untested. It should also be noted that in smaller domains with faster flows, passive drifters (measurement points) may exit the area quickly, reducing the available reference data and potentially affecting the accuracy of the reconstructed flow field.

Since the simplified two-dimensional quasi-steady flow model is unable to fully replicate transient flow dynamics and tends to accumulate errors over time, an adaptive diffusion coefficient is employed to govern scalar transport. This coefficient is updated according to the discrepancies observed between the reconstructed velocity field and the actual flow, assessed by recorded and simulated motion of drifters, thereby compensating for inaccuracies of the flow reconstruction. Although this adjustment improves the ability to capture the referent scalar probability distribution, it often leads to a wider spreading of the scalar, enlarging the area that must be considered and potentially including regions with very low probability. The extent of this spreading is influenced by both the magnitude and spatial pattern of reconstruction errors, which can result in deviations from the true physical dispersion and dilution of the scalar.

To test the proposed methodology under realistic conditions, three separate sea experiments were carried out, each designed to explore different aspects of the approach: steady flow reconstruction, the quasi-steady updating method, and a realistic search scenario. The preliminary experiment, conducted in Plomin Bay, offered valuable insights into surface velocity patterns, drifter dynamics, buoyancy effects, and small-scale variability of the flow. It also highlighted the limitations of relying on a steady reconstruction based on a single time step, as it was unable to accurately predict drifter movements, confirming the complex underlying behavior of the surface currents. In this relatively small bay, signal transmission remained largely reliable, posing minimal issues for data collection. The second sea experiment, conducted in Valun Bay, covered a much larger area and revealed additional challenges, including interruptions in data transmission and decreased GPS reliability. These problems were addressed by applying interpolation to fill missing measurements and a moving average technique to reduce GPS positional noise. Despite these complications, the reconstructed velocity fields closely matched observed flow patterns, demonstrating the robustness of the method within an acceptable margin of error. A fundamental aspect of this approach is that measurements are updated at each

measurement period, improving the optimization process while utilizing the progressive field initialization and search narrowing. This relies on the assumption that the surface flow does not change dramatically between updates, allowing computations to be carried out much more quickly, especially in larger or more complex domains.

Nevertheless, this method carries a risk of guiding the optimization toward suboptimal solutions, since each scenario begins with the internal field taken from the current best-estimated flow. Even without progressive field initialization, the optimization can still perform effectively. Adding numerical complexity, however, can limit the time available for real-time optimization, which directly affects the precision of flow reconstruction. Examining experimental drifter paths reveals that the method cannot capture every detail of the flow, yet it still produces reliable trajectory approximations. Challenges also emerge when measurement points are sparse, complicating error evaluation and making it difficult to determine which optimized outcome best represents reality. The issue becomes more pronounced when drifters are concentrated in a small region, restricting the ability to accurately reconstruct the flow across a broader domain. Thus, maintaining a balance between computational simplicity and sufficient optimization time is essential.

To address the challenges observed in the first two sea experiments and to test the methodology in a realistic search scenario with UAVs, a base station was positioned on elevated ground onshore, where all control, signal reception, and UAV takeoffs were conducted. This setup eliminated the signal gaps that occurred when the base station was on a boat in the second experiment, while also making operations such as UAV battery changes much easier, which would have been very difficult at sea. Despite this improvement, signal limitations from the UAVs themselves and the time spent before starting the search still significantly affected the coverage and detection of target objects. This experiment also confirmed that the shape and buoyancy of floating objects strongly influence drift behavior. Acquired sensors were placed on a floating buoy with a submerged drougue, while the target objects consisted of 0.5 x 0.5 meter wooden boards with flags, which were more strongly affected by purely surface currents. Consequently, the drift of sensors and the targets was not perfectly identical, as evidenced by their dispersal patterns over time. One potential improvement is the deployment of instruments capable of measuring the relative influence of wind, surface currents, and sub-surface flows at any given moment, so that the flow reconstruction can account for differences in object shape and buoyancy.

Overall, these experiments demonstrate the potential of the proposed methodology to reliably approximate surface flow and predict object movement under realistic conditions, while also highlighting areas for refinement, particularly in accounting for variable object properties and optimizing UAV-assisted search operations.

11 CONCLUSION

Reliable approximation of sea surface velocity fields is essential in tasks such as search and rescue or tracking the dispersion of pollutants, where modeling the advection of passive scalars must be performed in real or near real time. Achieving this, however, remains challenging because of the highly variable nature of oceanic flows. Existing approaches can capture certain aspects effectively, but they often fall short in representing the detailed dynamics of the flow and tend to require considerable computational resources, which limits their use for time-sensitive applications.

Therefore, this thesis proposes an ad-hoc data-driven framework for approximating sea surface velocity fields based on scattered drifter measurements. The approach relies on a two-dimensional surrogate fusion model coupled with an optimization procedure that adapts boundary conditions to ensure consistency with observed data. By deliberately omitting influences such as wind, tides, and temperature variations, the method emphasizes computational efficiency, offering a practical tool for real-world scenarios where assuming quasi-steady flow is sufficient for forecasting advection processes, including pollutant transport and object drift. Based on the results, several conclusions can be drawn:

- The framework reliably reconstructs the flow field across the entire domain, including regions without direct measurements, reducing the need for dense data collection and high computational cost.
- Coarse numerical meshes can be used, enhancing computational efficiency while still capturing essential flow patterns.
- A limited number of strategically placed measurements is sufficient for accurate reconstruction of sea surface velocity.
- Transient patterns can be reproduced by updating flow fields at regular intervals, without the need for fully time-dependent simulations.

- Passive scalar advection with compensating diffusion accounts for GPS errors, flow reconstruction inaccuracies, and other uncertainties, enabling dynamic updates of the probability distribution around the target location.
- The methodology was validated through three sea experiments, addressing practical challenges such as drifting dynamics, data transmission, computational framework, and realistic search scenarios with deployed targets.

Nevertheless, some limitations remain. By simplifying environmental influences such as wind, tides, and temperature variations, the method may not fully capture highly complex or three-dimensional flow structures, particularly in regions where such effects play a dominant role. Additionally, the framework assumes predominantly passive target motion, which may not accurately represent situations where objects or individuals actively navigate or swim, potentially affecting the predictive performance. The accuracy of flow reconstruction is also influenced by the number and allocation of measurement points, meaning that poorly distributed or insufficient data can reduce the fidelity of the reconstructed field. Finally, the assumption of quasi-steady flow may limit the method's applicability in rapidly evolving or highly turbulent scenarios, where temporal variability is significant and reconstruction of one time frame may not adequately describe the dynamics of the system.

Building on these findings, several directions for future research can further enhance the framework:

- Develop adaptive measurement deployment strategies to optimize data collection.
- Improve guidance strategies, detection models, and real-time data assimilation to increase operational efficiency and success rate.
- Combine the current framework with higher-fidelity simulations or complementary measurement systems to extend applicability to more complex or rapidly changing environments, while keeping in mind real-time applicability and computational efficiency

The results from both simulations and field experiments confirm that the approach effectively supports real-time search operations, demonstrating a practical balance between computational efficiency and adaptability, and confirming the hypothesis that limited measurements suffice for accurate reconstruction of the sea surface flow field and prediction of target probability dynamics.

BIBLIOGRAPHY

- [1] M. Reed, Ø. Johansen, P. J. Brandvik, P. Daling, A. Lewis, R. Fiocco, D. Mackay, and R. Prentki, “Oil spill modeling towards the close of the 20th century: Overview of the state of the art”, *Spill Science & Technology Bulletin*, vol. 5, no. 1, pp. 3–16, 1999.
- [2] M. F. Kirby and R. J. Law, “Accidental spills at sea—risk, impact, mitigation and the need for co-ordinated post-incident monitoring”, *Marine pollution bulletin*, vol. 60, no. 6, pp. 797–803, 2010.
- [3] J. Wang and Y. Shen, “Modeling oil spills transportation in seas based on unstructured grid, finite-volume, wave-ocean model”, *Ocean Modelling*, vol. 35, no. 4, pp. 332–344, 2010.
- [4] M. J. Olascoaga and G. Haller, “Forecasting sudden changes in environmental pollution patterns”, *Proceedings of the National Academy of Sciences*, vol. 109, no. 13, pp. 4738–4743, 2012.
- [5] A. C. Haza, E. D’Asaro, H. Chang, S. Chen, M. Curcic, C. Guigand, H. Huntley, G. Jacobs, G. Novelli, T. Özgökmen, *et al.*, “Drogue-loss detection for surface drifters during the lagrangian submesoscale experiment (laser)”, *Journal of atmospheric and oceanic technology*, vol. 35, no. 4, pp. 705–725, 2018.
- [6] S. Chaturvedi, B. P. Yadav, N. A. Siddiqui, and S. K. Chaturvedi, “Mathematical modelling and analysis of plastic waste pollution and its impact on the ocean surface”, *Journal of Ocean Engineering and Science*, vol. 5, no. 2, pp. 136–163, 2020.
- [7] V. S. Gulakaram, N. K. Vissa, and P. K. Bhaskaran, “Role of mesoscale eddies on atmospheric convection during summer monsoon season over the bay of bengal: A case study”, *Journal of Ocean Engineering and Science*, vol. 3, no. 4, pp. 343–354, 2018.
- [8] P.-M. Poulain, “Adriatic sea surface circulation as derived from drifter data between 1990 and 1999”, *Journal of Marine Systems*, vol. 29, no. 1-4, pp. 3–32, 2001.

- [9] L. Ursella, P.-M. Poulain, and R. P. Signell, “Surface drifter derived circulation in the northern and middle adriatic sea: Response to wind regime and season”, *Journal of Geophysical Research: Oceans*, vol. 111, no. C3, 2006.
- [10] D. B. Rao and D. J. Schwab, “A method of objective analysis for currents in a lake with application to lake ontario”, *Journal of Physical Oceanography*, vol. 11, no. 5, pp. 739–750, 1981.
- [11] V. Eremeev, L. Ivanov, and A. Kirwan Jr, “Reconstruction of oceanic flow characteristics from quasi-lagrangian data: 1. approach and mathematical methods”, *Journal of Geophysical Research: Oceans*, vol. 97, no. C6, pp. 9733–9742, 1992.
- [12] K. Cho, R. O. Reid, and W. D. Nowlin Jr, “Objectively mapped stream function fields on the texas-louisiana shelf based on 32 months of moored current meter data”, *Journal of Geophysical Research: Oceans*, vol. 103, no. C5, pp. 10 377–10 390, 1998.
- [13] M. Solano, M. Canals, and S. Leonardi, “Development and validation of a coastal ocean forecasting system for puerto rico and the us virgin islands”, *Journal of Ocean Engineering and Science*, vol. 3, no. 3, pp. 223–236, 2018.
- [14] J. Marmain, A. Molcard, P. Forget, A. Barth, and Y. Ourmieres, “Assimilation of hf radar surface currents to optimize forcing in the northwestern mediterranean sea”, *Non-linear Processes in Geophysics*, vol. 21, no. 3, pp. 659–675, 2014.
- [15] J. Hernandez-Lasheras, B. Mourre, A. Orfila, A. Santana, E. Reyes, and J. Tintoré, “Evaluating high-frequency radar data assimilation impact in coastal ocean operational modelling”, *Ocean Science*, vol. 17, no. 4, pp. 1157–1175, 2021.
- [16] L. Bellomo, A. Griffa, S. Cosoli, P. Falco, R. Gerin, I. Iermano, A. Kalampokis, Z. Kokkini, A. Lana, M. Magaldi, *et al.*, “Toward an integrated hf radar network in the mediterranean sea to improve search and rescue and oil spill response: The toasca project experience”, *Journal of Operational Oceanography*, vol. 8, no. 2, pp. 95–107, 2015.
- [17] J. D. Paduan and H. C. Graber, “Introduction to high-frequency radar: Reality and myth”, *oceanography*, vol. 10, no. 2, pp. 36–39, 1997.
- [18] A. Sentchev, P. Forget, and P. Fraunié, “Surface current dynamics under sea breeze conditions observed by simultaneous hf radar, adcp and drifter measurements”, *Ocean Dynamics*, vol. 67, no. 3, pp. 499–512, 2017.

- [19] J. T. Kohut, H. J. Roarty, and S. M. Glenn, “Characterizing observed environmental variability with hf doppler radar surface current mappers and acoustic doppler current profilers: Environmental variability in the coastal ocean”, *IEEE Journal of Oceanic Engineering*, vol. 31, no. 4, pp. 876–884, 2007.
- [20] R. Kostaschuk, J. Best, P. Villard, J. Peakall, and M. Franklin, “Measuring flow velocity and sediment transport with an acoustic doppler current profiler”, *Geomorphology*, vol. 68, no. 1-2, pp. 25–37, 2005.
- [21] D. Ciani, C. Fanelli, and B. Buongiorno Nardelli, “Estimating ocean currents from the joint reconstruction of absolute dynamic topography and sea surface temperature through deep learning algorithms”, *EGUsphere*, vol. 2024, pp. 1–25, 2024.
- [22] F. Doglioni, R. Ricker, B. Rabe, A. Barth, C. Troupin, and T. Kanzow, “Sea surface height anomaly and geostrophic current velocity from altimetry measurements over the arctic ocean (2011–2020)”, *Earth System Science Data*, vol. 15, no. 1, pp. 225–263, 2023.
- [23] B. Qiu, S. Chen, P. Klein, H. Torres, J. Wang, L.-L. Fu, and D. Menemenlis, “Reconstructing upper-ocean vertical velocity field from sea surface height in the presence of unbalanced motion”, *Journal of Physical Oceanography*, vol. 50, no. 1, pp. 55–79, 2020.
- [24] M. J. Martin, I. Hoteit, L. Bertino, and A. M. Moore, “Data assimilation schemes for ocean forecasting: State of the art”, *State of the Planet*, vol. 5, pp. 1–12, 2025.
- [25] R. Fablet, P. H. Viet, and R. Lguensat, “Data-driven models for the spatio-temporal interpolation of satellite-derived sst fields”, *IEEE Transactions on Computational Imaging*, vol. 3, no. 4, pp. 647–657, 2017.
- [26] M. Raissi, P. Perdikaris, and G. E. Karniadakis, “Physics-informed neural networks: A deep learning framework for solving forward and inverse problems involving nonlinear partial differential equations”, *Journal of Computational physics*, vol. 378, pp. 686–707, 2019.
- [27] Z. Chen, P. Wang, S. Bao, and W. Zhang, “Rapid reconstruction of temperature and salinity fields based on machine learning and the assimilation application”, *Frontiers in Marine Science*, vol. 9, p. 985 048, 2022.

- [28] J. Li and A. D. Heap, “A review of spatial interpolation methods for environmental scientists”, 2008.
- [29] M. A. Oliver and R. Webster, “Kriging: A method of interpolation for geographical information systems”, *International Journal of Geographical Information System*, vol. 4, no. 3, pp. 313–332, 1990.
- [30] G. Y. Lu and D. W. Wong, “An adaptive inverse-distance weighting spatial interpolation technique”, *Computers & geosciences*, vol. 34, no. 9, pp. 1044–1055, 2008.
- [31] J. Busch, D. Giese, L. Wissmann, and S. Kozerke, “Reconstruction of divergence-free velocity fields from cine 3d phase-contrast flow measurements”, *Magnetic resonance in medicine*, vol. 69, no. 1, pp. 200–210, 2013.
- [32] F. J. Narcowich, J. D. Ward, and G. B. Wright, “Divergence-free rbfs on surfaces”, *Journal of Fourier Analysis and Applications*, vol. 13, no. 6, pp. 643–663, 2007.
- [33] L. Li and Z. Pan, “Three-dimensional time-resolved lagrangian flow field reconstruction based on constrained least squares and stable radial basis function”, *Experiments in Fluids*, vol. 65, no. 4, p. 57, 2024.
- [34] S. Ward, P. Robins, A. Owen, J. Demmer, and S. Jenkins, “The importance of resolving nearshore currents in coastal dispersal models”, *Ocean Modelling*, vol. 183, p. 102 181, 2023.
- [35] J. Ohlmann, M. Molemaker, B. Baschek, B. Holt, G. Marmorino, and G. Smith, “Drifter observations of submesoscale flow kinematics in the coastal ocean”, *Geophysical Research Letters*, vol. 44, no. 1, pp. 330–337, 2017.
- [36] S. Guo, J. Mou, L. Chen, and P. Chen, “Improved kinematic interpolation for ais trajectory reconstruction”, *Ocean Engineering*, vol. 234, p. 109 256, 2021.
- [37] A. Sinha and R. Abernathey, “Estimating ocean surface currents with machine learning”, *Frontiers in Marine Science*, vol. 8, p. 672 477, 2021.
- [38] G. E. Manucharyan, L. Siegelman, and P. Klein, “A deep learning approach to spatiotemporal sea surface height interpolation and estimation of deep currents in geostrophic ocean turbulence”, *Journal of Advances in Modeling Earth Systems*, vol. 13, no. 1, e2019MS001965, 2021.

- [39] L. Zanna and T. Bolton, “Data-driven equation discovery of ocean mesoscale closures”, *Geophysical Research Letters*, vol. 47, no. 17, e2020GL088376, 2020.
- [40] C. G. Kerry, M. Roughan, S. Keating, D. Gwyther, G. Brassington, A. Siripatana, and J. M. A. Souza, “Comparison of 4-dimensional variational and ensemble optimal interpolation data assimilation systems using a regional ocean modeling system (v3. 4) configuration of the eddy-dominated east australian current system”, *Geoscientific Model Development*, vol. 17, no. 6, pp. 2359–2386, 2024.
- [41] I. Hoteit, X. Luo, M. Bocquet, A. Kohl, and B. Ait-El-Fquih, “Data assimilation in oceanography: Current status and new directions”, *New frontiers in operational oceanography*, pp. 465–512, 2018.
- [42] S. Ghalambaz, M. Abbaszadeh, I. Sadrehaghghi, O. Younis, M. Ghalambaz, and M. Ghalambaz, “A forty years scientometric investigation of artificial intelligence for fluid-flow and heat-transfer (aifh) during 1982 and 2022”, *Engineering Applications of Artificial Intelligence*, vol. 127, p. 107 334, 2024.
- [43] M. D. Grossi, M. Kubat, and T. M. Özgökmen, “Predicting particle trajectories in oceanic flows using artificial neural networks”, *Ocean Modelling*, vol. 156, p. 101 707, 2020.
- [44] M. Song, W. Hu, S. Liu, S. Chen, X. Fu, J. Zhang, W. Li, and Y. Xu, “Developing an artificial intelligence-based method for predicting the trajectory of surface drifting buoys using a hybrid multi-layer neural network model”, *Journal of Marine Science and Engineering*, vol. 12, no. 6, p. 958, 2024.
- [45] L. Sun, H. Gao, S. Pan, and J.-X. Wang, “Surrogate modeling for fluid flows based on physics-constrained deep learning without simulation data”, *Computer Methods in Applied Mechanics and Engineering*, vol. 361, p. 112 732, 2020.
- [46] M. Tang, Y. Liu, and L. J. Durlofsky, “Deep-learning-based surrogate flow modeling and geological parameterization for data assimilation in 3d subsurface flow”, *Computer Methods in Applied Mechanics and Engineering*, vol. 376, p. 113 636, 2021.
- [47] M. Reichstein, G. Camps-Valls, B. Stevens, M. Jung, J. Denzler, N. Carvalhais, and F. Prabhat, “Deep learning and process understanding for data-driven earth system science”, *Nature*, vol. 566, no. 7743, pp. 195–204, 2019.

- [48] E. De Bézenac, A. Pajot, and P. Gallinari, “Deep learning for physical processes: Incorporating prior scientific knowledge”, *Journal of Statistical Mechanics: Theory and Experiment*, vol. 2019, no. 12, p. 124 009, 2019.
- [49] S. J. Saida, S. P. Sahoo, and S. Ari, “Deep convolution neural network based semantic segmentation for ocean eddy detection”, *Expert Systems with Applications*, vol. 219, p. 119 646, 2023.
- [50] J. Willard, X. Jia, S. Xu, M. Steinbach, and V. Kumar, “Integrating physics-based modeling with machine learning: A survey”, *arXiv preprint arXiv:2003.04919*, vol. 1, no. 1, pp. 1–34, 2020.
- [51] A. Farchi, P. Laloyaux, M. Bonavita, and M. Bocquet, “Using machine learning to correct model error in data assimilation and forecast applications”, *Quarterly Journal of the Royal Meteorological Society*, vol. 147, no. 739, pp. 3067–3084, 2021.
- [52] T. de Wolff, H. Carrillo, L. Marti, and N. Sanchez-Pi, “Assessing physics informed neural networks in ocean modelling and climate change applications”, in *AI: Modeling Oceans and Climate Change Workshop at ICLR 2021*, 2021.
- [53] V. Futch and A. Allen, “Search and rescue applications: On the need to improve ocean observing data systems in offshore or remote locations”, *Frontiers in Marine Science*, vol. 6, p. 301, 2019.
- [54] Z. Yin and P. A. Durbin, “Passive scalar transport modeling for hybrid rans/les simulation”, *Flow, turbulence and combustion*, vol. 98, no. 1, pp. 177–194, 2017.
- [55] R. B. Rood, “Numerical advection algorithms and their role in atmospheric transport and chemistry models”, *Reviews of geophysics*, vol. 25, no. 1, pp. 71–100, 1987.
- [56] Z. Warhaft, “Passive scalars in turbulent flows”, *Annual review of fluid mechanics*, vol. 32, no. 1, pp. 203–240, 2000.
- [57] E. Van Sebille, S. M. Griffies, R. Abernathey, T. P. Adams, P. Berloff, A. Biastoch, B. Blanke, E. P. Chassignet, Y. Cheng, C. J. Cotter, *et al.*, “Lagrangian ocean analysis: Fundamentals and practices”, *Ocean modelling*, vol. 121, pp. 49–75, 2018.
- [58] R. E. Davis, “Lagrangian and eulerian measurements of ocean transport processes”, in *Ocean Processes in climate dynamics: Global and Mediterranean examples*, Springer, 1994, pp. 29–60.

- [59] W. Shi, P. Peruzzo, and A. Defina, “An eulerian model for the transport and diffusion of floating particles within regions of emergent vegetation”, *Water Resources Research*, vol. 57, no. 8, e2021WR029625, 2021.
- [60] F. Hernandez, P.-Y. Le Traon, and R. Morrow, “Mapping mesoscale variability of the azores current using topex/poseidon and ers 1 altimetry, together with hydrographic and lagrangian measurements”, *Journal of Geophysical Research: Oceans*, vol. 100, no. C12, pp. 24 995–25 006, 1995.
- [61] A. Molcard, L. I. Piterbarg, A. Griffa, T. M. Özgökmen, and A. J. Mariano, “Assimilation of drifter observations for the reconstruction of the eulerian circulation field”, *Journal of Geophysical Research: Oceans*, vol. 108, no. C3, 2003.
- [62] J. R. Bennett and A. H. Clites, “Accuracy of trajectory calculation in a finite-difference circulation model”, *Journal of Computational Physics*, vol. 68, no. 2, pp. 272–282, 1987.
- [63] P. Tkalich, “A cfd solution of oil spill problems”, *Environmental Modelling & Software*, vol. 21, no. 2, pp. 271–282, 2006.
- [64] A. F. Shchepetkin and J. C. McWilliams, “The regional oceanic modeling system (roms): A split-explicit, free-surface, topography-following-coordinate oceanic model”, *Ocean modelling*, vol. 9, no. 4, pp. 347–404, 2005.
- [65] E. P. Chassignet, H. E. Hurlburt, O. M. Smedstad, G. R. Halliwell, P. J. Hogan, A. J. Wallcraft, R. Baraille, and R. Bleck, “The hycom (hybrid coordinate ocean model) data assimilative system”, *Journal of Marine Systems*, vol. 65, no. 1-4, pp. 60–83, 2007.
- [66] D. Storkey, E. Blockley, R. Furner, C. Guiavarc’h, D. Lea, M. Martin, R. Barciela, A. Hines, P. Hyder, and J. Siddorn, “Forecasting the ocean state using nemo: The new foam system”, *Journal of operational oceanography*, vol. 3, no. 1, pp. 3–15, 2010.
- [67] R. Vennell, M. Scheel, S. Weppe, B. Knight, and M. Smeaton, “Fast lagrangian particle tracking in unstructured ocean model grids”, *Ocean Dynamics*, vol. 71, no. 4, pp. 423–437, 2021.
- [68] R. Camassa, N. Martinsen-Burrell, and R. M. McLaughlin, “Dynamics of probability density functions for decaying passive scalars in periodic velocity fields”, *Physics of Fluids*, vol. 19, no. 11, 2007.

- [69] S. Ghosh, A. Leonard, and S. Wiggins, “Diffusion of a passive scalar from a no-slip boundary into a two-dimensional chaotic advection field”, *Journal of Fluid Mechanics*, vol. 372, pp. 119–163, 1998.
- [70] D. Qi and A. J. Majda, “Predicting extreme events for passive scalar turbulence in two-layer baroclinic flows through reduced-order stochastic models”, *Commun. Math. Sci*, vol. 16, no. 1, pp. 17–51, 2018.
- [71] K. H. Christensen, Ø. Breivik, K.-F. Dagestad, J. Röhrs, and B. Ward, “Short-term predictions of oceanic drift”, *Oceanography*, vol. 31, no. 3, pp. 59–67, 2018.
- [72] A. Carbone, D. Ciacelli, A. Finzi, and F. Pirri, “Autonomous attentive exploration in search and rescue scenarios”, in *International Workshop on Attention in Cognitive Systems*, Springer, 2007, pp. 431–446.
- [73] Z. Qian, T. Yang, and M. Liu, “An overview of coupled lagrangian–eulerian methods for ocean engineering”, *Journal of Marine Science and Application*, vol. 23, no. 2, pp. 366–397, 2024.
- [74] Y.-T. Shen, J.-W. Lai, L.-G. Leu, Y.-C. Lu, J.-M. Chen, H.-J. Shao, H.-W. Chen, K.-T. Chang, C.-T. Terng, Y.-C. Chang, *et al.*, “Applications of ocean currents data from high-frequency radars and current profilers to search and rescue missions around taiwan”, *Journal of Operational Oceanography*, vol. 12, no. sup2, S126–S136, 2019.
- [75] A. A. Allen and J. V. Plourde, “Review of leeway: Field experiments and implementation”, Tech. Rep., 1999.
- [76] A. A. Allen, “Leeway divergence”, *US Coast Guard Research and Development Center*, 2005.
- [77] Ø. Breivik, A. A. Allen, C. Maisondieu, and J. C. Roth, “Wind-induced drift of objects at sea: The leeway field method”, *Applied Ocean Research*, vol. 33, no. 2, pp. 100–109, 2011.
- [78] K. Zhu, L. Mu, and X. Xia, “An ensemble trajectory prediction model for maritime search and rescue and oil spill based on sub-grid velocity model”, *Ocean Engineering*, vol. 236, p. 109 513, 2021.

- [79] A. Révelard, E. Reyes, B. Mourre, I. Hernández-Carrasco, A. Rubio, P. Lorente, C. D. L. Fernández, J. Mader, E. Álvarez-Fanjul, and J. Tintoré, “Sensitivity of skill score metric to validate lagrangian simulations in coastal areas: Recommendations for search and rescue applications”, *Frontiers in Marine Science*, vol. 8, p. 630 388, 2021.
- [80] M. Hart-Davis, B. Backeberg, and M. Bakhoday-Paskyabi, “An assessment of the importance of combining wind, ocean currents and stochastic motions in a particle trajectory model for search and rescue applications”, *South Afr. Soc. Atmos. Sci*, vol. 34, pp. 157–160, 2018.
- [81] S.-z. Wang, H.-b. Nie, and C.-j. Shi, “A drifting trajectory prediction model based on object shape and stochastic motion features”, *Journal of Hydrodynamics*, vol. 26, no. 6, pp. 951–959, 2014.
- [82] Ø. Breivik, A. A. Allen, C. Maisondieu, and M. Olagnon, “Advances in search and rescue at sea”, *Ocean Dynamics*, vol. 63, pp. 83–88, 2013.
- [83] G. Sutherland, N. Soontiens, F. Davidson, G. C. Smith, N. Bernier, H. Blanken, D. Schillinger, G. Marcotte, J. Röhrs, K.-F. Dagestad, *et al.*, “Evaluating the leeway coefficient of ocean drifters using operational marine environmental prediction systems”, *Journal of Atmospheric and Oceanic Technology*, vol. 37, no. 11, pp. 1943–1954, 2020.
- [84] M. Serra, P. Sathe, I. Rypina, A. Kirincich, S. D. Ross, P. Lermusiaux, A. Allen, T. Peacock, and G. Haller, “Search and rescue at sea aided by hidden flow structures”, *Nature communications*, vol. 11, no. 1, p. 2525, 2020.
- [85] J. Röhrs, G. Sutherland, G. Jeans, M. Bedington, A. K. Sperrevik, K.-F. Dagestad, Y. Gusdal, C. Mauritzen, A. Dale, and J. H. LaCasce, “Surface currents in operational oceanography: Key applications, mechanisms, and methods”, *Journal of Operational Oceanography*, vol. 16, no. 1, pp. 60–88, 2023.
- [86] O. Nesterov, “Consideration of various aspects in a drift study of mh370 debris”, *Ocean Science*, vol. 14, no. 3, pp. 387–402, 2018.
- [87] C. H. Barker, V. H. Kourafalou, C. J. Beegle-Krause, M. Boufadel, M. A. Bourassa, S. G. Buschang, Y. Androulidakis, E. P. Chassignet, K.-F. Dagestad, D. G. Danmeier, *et al.*, “Progress in operational modeling in support of oil spill response”, *Journal of marine science and engineering*, vol. 8, no. 9, p. 668, 2020.

- [88] B. Hackett, Ø. Breivik, and C. Wettré, “Forecasting the drift of objects and substances in the ocean”, *Ocean weather forecasting: an integrated view of oceanography*, pp. 507–523, 2006.
- [89] T. J. Wagner, I. Eisenman, A. M. Ceroli, and N. C. Constantinou, “How winds and ocean currents influence the drift of floating objects”, *Journal of Physical Oceanography*, vol. 52, no. 5, pp. 907–916, 2022.
- [90] X. André, B. Moreau, and S. Le Reste, “Argos-3 satellite communication system: Implementation on the arvor oceanographic profiling floats”, *Journal of Atmospheric and Oceanic Technology*, vol. 32, no. 10, pp. 1902–1914, 2015.
- [91] metOcean telematics, *Stokes drifter*, <https://metocean.com/products/stokes-drifter/>, [Online; accessed 06-July-2025], 2025.
- [92] X. B. Satlink, *Roby x, iridium gps surface current tracker*, <https://xeostech.com/roby-x>, [Online; accessed 06-July-2025], 2025.
- [93] S. S. Technologies, *Coastal nomad*, <https://www.southteksl.com/index.php/products/coastal-nomad/drifter-coastal-nomad-b-detail>, [Online; accessed 06-July-2025], 2025.
- [94] A. Marine, *Portable ais, tb560*, <https://www.alltekmarine.com/products/portable-ais/TB560>, [Online; accessed 06-July-2025], 2025.
- [95] P. Gyre, *Pacific gyre drifting buoys*, <https://pacific-gyre.odoo.com/applications-meteorology>, Accessed: 2025-29-08, 2025.
- [96] J. Röhrs, A. K. Sperrevik, K. H. Christensen, G. Broström, and Ø. Breivik, “Comparison of hf radar measurements with eulerian and lagrangian surface currents”, *Ocean Dynamics*, vol. 65, no. 5, pp. 679–690, 2015.
- [97] G. L. O. System, *High-frequency-radar*, <https://glos.org/observing/high-frequency-radar/>, Accessed: 2025-07-11, 2025.
- [98] I. O. O. System, *Hf radar*, <https://ioos.noaa.gov/project/hf-radar/>, Accessed: 2025-07-21, 2025.
- [99] D. B. Chelton, M. G. Schlax, R. M. Samelson, and R. A. de Szoeke, “Global observations of large oceanic eddies”, *Geophysical Research Letters*, vol. 34, no. 15, 2007. DOI: 10.1029/2007GL030812.

- [100] R. Morrow, L.-L. Fu, F. Arduin, G. Dibarboure, S. Gille, P. Klein, D. Menemenlis, A. Pascual, M.-H. Rio, and C. Ubelmann, “Global observations of fine-scale ocean surface currents from satellite altimetry and their applications”, *Frontiers in Marine Science*, vol. 6, p. 382, 2019. DOI: 10.3389/fmars.2019.00382.
- [101] P.-Y. Le Traon, P. Klein, B. L. Hua, and A. Duguay-Tetzlaff, “Use of satellite altimetry to study mesoscale and submesoscale processes”, *Remote Sensing*, vol. 7, no. 12, pp. 16398–16419, 2015. DOI: 10.3390/rs71215874.
- [102] V. Klemas, “Remote sensing of ocean currents: An overview”, *Remote Sensing*, vol. 4, no. 5, pp. 1232–1261, 2012. DOI: 10.3390/rs4051232.
- [103] E. R. Abraham, N. Young, and K. Richardson, “Importance of high resolution velocity fields in modelling drift of search and rescue objects”, *Ocean Modelling*, vol. 68, pp. 81–101, 2013. DOI: 10.1016/j.ocemod.2013.04.006.
- [104] P. Klein and G. Lapeyre, “The oceanic vertical pump induced by mesoscale and submesoscale turbulence”, *Annual Review of Marine Science*, vol. 1, pp. 351–375, 2009. DOI: 10.1146/annurev.marine.010908.163704.
- [105] V. Kudryavtsev, B. Chapron, and F. Collard, “Synergy of sentinel-1 and sentinel-2 imagery for surface current retrieval in coastal waters”, *Remote Sensing of Environment*, vol. 199, pp. 93–106, 2017. DOI: 10.1016/j.rse.2017.07.015.
- [106] W. J. Emery and R. E. Thomson, *Data Analysis Methods in Physical Oceanography*, 2nd. Elsevier, 2001.
- [107] M. S. Spydell, F. Feddersen, and J. Macmahan, “The effect of drifter gps errors on estimates of submesoscale vorticity”, *Journal of Atmospheric and Oceanic Technology*, vol. 36, no. 11, pp. 2101–2119, 2019.
- [108] A. C. Haza, T. M. Özgökmen, A. Griffa, A. C. Poje, and M.-P. Lelong, “How does drifter position uncertainty affect ocean dispersion estimates?”, *Journal of Atmospheric and Oceanic Technology*, vol. 31, no. 12, pp. 2809–2828, 2014.
- [109] R. Chapman, L. Shay, H. Graber, J. Edson, A. Karachintsev, C. Trump, and D. Ross, “On the accuracy of hf radar surface current measurements: Intercomparisons with ship-based sensors”, *Journal of Geophysical Research: Oceans*, vol. 102, no. C8, pp. 18737–18748, 1997.

- [110] J. D. Paduan and L. K. Rosenfeld, “Remotely sensed surface currents in monterey bay from shore-based hf radar (coastal ocean dynamics application radar)”, *Journal of Geophysical Research: Oceans*, vol. 101, no. C9, pp. 20 669–20 686, 1996.
- [111] A. Pascual, C. Boone, G. Larnicol, and P.-Y. Le Traon, “On the quality of real-time altimeter gridded fields: Comparison with in situ data”, *Journal of Atmospheric and Oceanic Technology*, vol. 26, no. 3, pp. 556–569, 2009.
- [112] K. Jakac, L. Lanča, A. Sikirica, and S. Ivić, “Approximation of sea surface velocity field by fitting surrogate two-dimensional flow to scattered measurements”, *arXiv preprint arXiv:2401.12746*, 2024.
- [113] M. Fingas, “Introduction to spill modeling”, in *Oil spill science and technology*, Elsevier, 2025, pp. 273–307.
- [114] M. D. Gunzburger, *Finite element methods for viscous incompressible flows: a guide to theory, practice, and algorithms*. Elsevier, 2012.
- [115] P.-L. Lions, *Mathematical Topics in Fluid Mechanics: Volume 2: Compressible Models*. Oxford Lecture Mathematics and, 1996, vol. 2.
- [116] M. Kronbichler, “Numerical methods for the navier–stokes equations applied to turbulent flow and to multi-phase flow”, PhD thesis, Uppsala University, 2009.
- [117] K. Jakac, L. Lanča, A. Sikirica, and S. Ivić, “Efficient data-driven flow modeling for accurate passive scalar advection in submesoscale domains”, *Applied Ocean Research*, vol. 162, p. 104 699, 2025, ISSN: 0141-1187. DOI: <https://doi.org/10.1016/j.apor.2025.104699>. [Online]. Available: <https://www.sciencedirect.com/science/article/pii/S0141118725002858>.
- [118] S. Cosoli, M. Ličer, M. Vodopivec, and V. Malačič, “Surface circulation in the gulf of trieste (northern adriatic sea) from radar, model, and adcp comparisons”, *Journal of Geophysical Research: Oceans*, vol. 118, no. 11, pp. 6183–6200, 2013.
- [119] G. Notarstefano, P.-M. Poulain, and E. Mauri, “Estimation of surface currents in the adriatic sea from sequential infrared satellite images”, *Journal of Atmospheric and Oceanic Technology*, vol. 25, no. 2, pp. 271–285, 2008.

- [120] R. Bolaños, J. V. T. Sørensen, A. Benetazzo, S. Carniel, and M. Sclavo, “Modelling ocean currents in the northern adriatic sea”, *Continental Shelf Research*, vol. 87, pp. 54–72, 2014.
- [121] M. U. Guçel and A. Sakalli, “Analyzing the mediterranean sea’s dynamic current system and modeling of renewable current energy potential”, *Journal of Marine Science and Engineering*, vol. 12, no. 4, p. 671, 2024.
- [122] V. Kovačević, M. Gačić, I. M. Mosquera, A. Mazzoldi, and S. Marinetti, “Hf radar observations in the northern adriatic: Surface current field in front of the venetian lagoon”, *Journal of marine systems*, vol. 51, no. 1-4, pp. 95–122, 2004.
- [123] M. Berta, L. Ursella, F. Nencioli, A. M. Doglioli, A. A. Petrenko, and S. Cosoli, “Surface transport in the northeastern adriatic sea from fsle analysis of hf radar measurements”, *Continental Shelf Research*, vol. 77, pp. 14–23, 2014.
- [124] P. Higuera, J. L. Lara, and I. J. Losada, “Simulating coastal engineering processes with openfoam®”, *Coastal Engineering*, vol. 71, pp. 119–134, 2013.
- [125] J. D. Anderson, J. Wendt, *et al.*, *Computational fluid dynamics*. Springer, 1995, vol. 206.
- [126] J. H. Ferziger and M. Perić, *Computational methods for fluid dynamics*. Springer, 2002, vol. 586.
- [127] P. Sagaut, *Large eddy simulation for incompressible flows: an introduction*. Springer, 2006.
- [128] E. Frederix, J. A. Hopman, T. Karageorgiou, and E. M. Komen, “Towards direct numerical simulation of turbulent co-current taylor bubble flow”, *arXiv preprint arXiv:2010.03866*, 2020.
- [129] T. O. Foundation, *Openfoam user guide*, <https://www.openfoam.com/documentation/user-guide>, [Online; accessed 04-June-2025], 2016.
- [130] J.-F. Hetu and D. H. Pelletier, “Fast, adaptive finite element scheme for viscous incompressible flows”, *AIAA journal*, vol. 30, no. 11, pp. 2677–2682, 1992.
- [131] F. M. White and J. Majdalani, *Viscous fluid flow*. McGraw-Hill New York, 2006, vol. 3.
- [132] H. Versteeg and W. Malalasekera, “Computational fluid dynamics: The finite volume method”, *Harlow, England: Longman Scientific & Technical*, 1995.

- [133] A. M. Saeed and T. A. F. Alfawaz, “Finite volume method and its applications in computational fluid dynamics”, *Axioms*, vol. 14, no. 5, p. 359, 2025.
- [134] J. Ferziger and M. Peric, *Computational Methods for Fluid Dynamics*. Springer Berlin Heidelberg, 2012, ISBN: 9783642560262. [Online]. Available: <https://books.google.hr/books?id=BZnvCAAQAQBAJ>.
- [135] F. R. Menter, “Improved two-equation k-omega turbulence models for aerodynamic flows”, NASA Ames Research Center Moffett Field, CA, United States, Tech. Rep., 1992.
- [136] H. G. Weller, G. Tabor, H. Jasak, and C. Fureby, “A tensorial approach to computational continuum mechanics using object-oriented techniques”, *Computers in physics*, vol. 12, no. 6, pp. 620–631, 1998.
- [137] T. Zirwes, M. Sontheimer, F. Zhang, A. Abdelsamie, F. E. H. Pérez, O. T. Stein, H. G. Im, A. Kronenburg, and H. Bockhorn, “Assessment of numerical accuracy and parallel performance of openfoam and its reacting flow extension ebidnsfoam”, *Flow, Turbulence and Combustion*, vol. 111, no. 2, pp. 567–602, 2023.
- [138] Z. Seifollahi Moghadam, F. Guibault, and A. Garon, “On the evaluation of mesh resolution for large-eddy simulation of internal flows using openfoam”, *Fluids*, vol. 6, no. 1, p. 24, 2021.
- [139] H. Jasak, “Openfoam: Open source cfd in research and industry”, *International journal of naval architecture and ocean engineering*, vol. 1, no. 2, pp. 89–94, 2009.
- [140] S. V. Patankar and D. B. Spalding, “A calculation procedure for heat, mass and momentum transfer in three-dimensional parabolic flows”, in *Numerical prediction of flow, heat transfer, turbulence and combustion*, Elsevier, 1983, pp. 54–73.
- [141] X. Chao, N. J. Shankar, and H. F. Cheong, “Two-and three-dimensional oil spill model for coastal waters”, *Ocean engineering*, vol. 28, no. 12, pp. 1557–1573, 2001.
- [142] P. Tkalich, K. Huda, and K. Y. Hoong Gin, “A multiphase oil spill model”, *Journal of Hydraulic Research*, vol. 41, no. 2, pp. 115–125, 2003.
- [143] N. Gruber and S. C. Doney, “Modeling of ocean biogeochemistry and ecology”, *Encyclopedia of Ocean Sciences*, vol. 5, pp. 547–560, 2019.

- [144] E. P. Chassignet, J. Le Sommer, and A. J. Wallcraft, “General circulation models”, *Encyclopedia of Ocean Sciences, 3rd edn., edited by: Cochran, KJ, Bokuniewicz, HJ, and Yager, PL*, vol. 5, pp. 486–490, 2019.
- [145] C. Bricaud, J. Le Sommer, G. Madec, C. Calone, J. Deshayes, C. Ethe, J. Chanut, and M. Levy, “Multi-grid algorithm for passive tracer transport in the nemo ocean circulation model: A case study with the nemo ogcm (version 3.6)”, *Geoscientific Model Development*, vol. 13, no. 11, pp. 5465–5483, 2020.
- [146] K. Tsiaras, Y. Hatzonikolakis, S. Kalaroni, A. Pollani, and G. Triantafyllou, “Modeling the pathways and accumulation patterns of micro-and macro-plastics in the mediterranean”, *Frontiers in Marine Science*, vol. 8, p. 743 117, 2021.
- [147] M. Fatahi, G. Akdogan, C. Dorfling, and P. Van Wyk, “Numerical study of microplastic dispersal in simulated coastal waters using cfd approach”, *Water*, vol. 13, no. 23, p. 3432, 2021.
- [148] Y. Lun, H. Wang, J. Wu, Y. Liu, and Y. Wang, “Target search in dynamic environments with multiple solar-powered uavs”, *IEEE Transactions on Vehicular Technology*, vol. 71, no. 9, pp. 9309–9321, 2022.
- [149] S. W. Cho, H. J. Park, H. Lee, D. H. Shim, and S.-Y. Kim, “Coverage path planning for multiple unmanned aerial vehicles in maritime search and rescue operations”, *Computers & Industrial Engineering*, vol. 161, p. 107 612, 2021.
- [150] B. Ai, B. Li, S. Gao, J. Xu, and H. Shang, “An intelligent decision algorithm for the generation of maritime search and rescue emergency response plans”, *IEEE Access*, vol. 7, pp. 155 835–155 850, 2019.
- [151] J. P. Martinez-Esteso, F. J. Castellanos, J. Calvo-Zaragoza, and A. J. Gallego, “Maritime search and rescue missions with aerial images: A survey”, *Computer Science Review*, vol. 57, p. 100 736, 2025.
- [152] L. Li, X. Zhang, W. Yue, and Z. Liu, “Cooperative search for dynamic targets by multiple uavs with communication data losses”, *ISA transactions*, vol. 114, pp. 230–241, 2021.
- [153] H. Zhang, Y. Huang, H. Qin, and Z. Geng, “Usv search mission planning methodology for lost target rescue on sea”, *Electronics*, vol. 12, no. 22, p. 4584, 2023.

- [154] G. Mathew and I. Mezić, “Metrics for ergodicity and design of ergodic dynamics for multi-agent systems”, *Physica D: Nonlinear Phenomena*, vol. 240, no. 4-5, pp. 432–442, 2011.
- [155] G. Mathew, A. Surana, and I. Mezić, “Uniform coverage control of mobile sensor networks for dynamic target detection”, in *49th IEEE Conference on Decision and Control (CDC)*, IEEE, 2010, pp. 7292–7299.
- [156] S. Ivić, B. Crnković, H. Arbabi, S. Loire, P. Clary, and I. Mezić, “Search strategy in a complex and dynamic environment: The mh370 case”, *Scientific Reports*, vol. 10, no. 1, p. 19 640, 2020.
- [157] I. Abraham and T. D. Murphey, “Decentralized ergodic control: Distribution-driven sensing and exploration for multiagent systems”, *IEEE Robotics and Automation Letters*, vol. 3, no. 4, pp. 2987–2994, 2018.
- [158] I. Abraham, A. Prabhakar, M. J. Hartmann, and T. D. Murphey, “Ergodic exploration using binary sensing for nonparametric shape estimation”, *IEEE robotics and automation letters*, vol. 2, no. 2, pp. 827–834, 2017.
- [159] S. Ivić, B. Crnković, and I. Mezić, “Ergodicity-based cooperative multiagent area coverage via a potential field”, *IEEE transactions on cybernetics*, vol. 47, no. 8, pp. 1983–1993, 2016.
- [160] S. Ivić, A. Sikirica, and B. Crnković, “Constrained multi-agent ergodic area surveying control based on finite element approximation of the potential field”, *Engineering applications of artificial intelligence*, vol. 116, p. 105 441, 2022.
- [161] S. Ivić, “Motion control for autonomous heterogeneous multiagent area search in uncertain conditions”, *IEEE Transactions on Cybernetics*, vol. 52, no. 5, pp. 3123–3135, 2020.
- [162] J. Schöberl, “Netgen an advancing front 2d/3d-mesh generator based on abstract rules”, *Computing and visualization in science*, vol. 1, no. 1, pp. 41–52, 1997.
- [163] ———, “C++ 11 implementation of finite elements in ngsolve”, *Institute for analysis and scientific computing, Vienna University of Technology*, vol. 30, 2014.
- [164] S. Hub, *Sentinel-2 l2a*, <https://www.sentinel-hub.com/>, [Online; accessed 14-June-2024], 2024.

- [165] S. K. McFeeters, “The use of the normalized difference water index (ndwi) in the delineation of open water features”, *International journal of remote sensing*, vol. 17, no. 7, pp. 1425–1432, 1996.
- [166] F. Juretic, “Cfmesh user guide”, *Creative Fields, Ltd*, vol. 1, 2015.
- [167] S. Ivić and S. Družeta, *Indago: Python 3 module for numerical optimization*, version 0.4.5, 2023. [Online]. Available: <https://pypi.org/project/Indago/0.4.5/>.
- [168] J. Kennedy and R. Eberhart, “Particle swarm optimization”, in *Proceedings of ICNN’95-international conference on neural networks*, IEEE, vol. 4, 1995, pp. 1942–1948.
- [169] Y. Tan and Y. Zhu, “Fireworks algorithm for optimization”, in *Advances in Swarm Intelligence: First International Conference, ICSI 2010, Beijing, China, June 12-15, 2010, Proceedings, Part I 1*, Springer, 2010, pp. 355–364.
- [170] D. Karaboga and B. Akay, “A comparative study of artificial bee colony algorithm”, *Applied mathematics and computation*, vol. 214, no. 1, pp. 108–132, 2009.
- [171] C. Audet and J. E. Dennis Jr, “Mesh adaptive direct search algorithms for constrained optimization”, *SIAM Journal on optimization*, vol. 17, no. 1, pp. 188–217, 2006.
- [172] P. J. Roache, *Verification and validation in computational science and engineering*. Hermosa Albuquerque, NM, 1998, vol. 895.
- [173] M. G. Magaldi, C. Mantovani, and S. Cosoli, *Current velocities measured by hf radars in gulf of trieste - april 2012*, 2019. DOI: 10.5281/zenodo.3245409. [Online]. Available: <https://doi.org/10.5281/zenodo.3245409>.
- [174] I. of Oceanography and Fisheries, *Physical oceanography laboratory*, <https://galijulador.hr/en/>, [Online; accessed 19-October-2023], 2023.
- [175] C. Ohlmann, P. White, L. Washburn, B. Emery, E. Terrill, and M. Otero, “Interpretation of coastal hf radar–derived surface currents with high-resolution drifter data”, *Journal of Atmospheric and Oceanic Technology*, vol. 24, no. 4, pp. 666–680, 2007.
- [176] A. Molcard, P. Poulain, P. Forget, A. Griffa, Y. Barbin, J. Gaggelli, J. De Maistre, and M. Rixen, “Comparison between vhf radar observations and data from drifter clusters in the gulf of la spezia (mediterranean sea)”, *Journal of Marine Systems*, vol. 78, S79–S89, 2009.

- [177] F. Enrile, G. Besio, A. Stocchino, M. Magaldi, C. Mantovani, S. Cosoli, R. Gerin, and P. Poulain, “Evaluation of surface lagrangian transport barriers in the gulf of trieste”, *Continental Shelf Research*, vol. 167, pp. 125–138, 2018.
- [178] S. Querin, S. Cosoli, R. Gerin, C. Laurent, V. Malačić, N. Pristov, and P.-M. Poulain, “Multi-platform, high-resolution study of a complex coastal system: The toasca experiment in the gulf of trieste”, *Journal of Marine Science and Engineering*, vol. 9, no. 5, p. 469, 2021.
- [179] R. H. Stewart and J. W. Joy, “Hf radio measurements of surface currents”, in *Deep sea research and oceanographic abstracts*, Elsevier, vol. 21, 1974, pp. 1039–1049.
- [180] D. V. Ivonin, P. Broche, J.-L. Devenon, and V. I. Shrira, “Validation of hf radar probing of the vertical shear of surface currents by acoustic doppler current profiler measurements”, *Journal of Geophysical Research: Oceans*, vol. 109, no. C4, 2004.
- [181] M. Svanberg, V. Santén, A. Hörteborn, H. Holm, and C. Finnsgård, “Ais in maritime research”, *Marine Policy*, vol. 106, p. 103 520, 2019.
- [182] D. Wright, C. Janzen, R. Bochenek, J. Austin, and E. Page, “Marine observing applications using ais: Automatic identification system”, *Frontiers in Marine Science*, vol. 6, p. 537, 2019.
- [183] *Decode ais messages*, <https://pyais.readthedocs.io/en/latest/>.
- [184] Windy.com, *Windy - Weather Forecast and Visualization*, <https://www.windy.com>, Accessed: 2024-09-22.
- [185] Croatian Meteorological and Hydrological Service, *DHMZ - Weather and Hydrological Forecasts*, <https://meteo.hr>, Accessed: 2024-09-22.
- [186] Windfinder GmbH & Co. KG, *Windfinder - Wind, Wave and Weather Forecasts*, <https://www.windfinder.com>, Accessed: 2024-09-22.
- [187] L. Lanča, S. Dumenčić, K. Jakac, and S. Ivić, “Experimental validation and robustness analysis of ergodic uav control”, in *2025 11th International Conference on Automation, Robotics, and Applications (ICARA)*, IEEE, 2025, pp. 257–261.

LIST OF FIGURES

- 3.1 Examples of surface drifters used in oceanographic studies. Different models are optimized for various applications and primarily differ in their communication and data transmission capabilities [91–94]. 18
- 3.2 Different types of drogues, constructed from various materials and designed for different deployment conditions [95]. 19
- 3.3 Great Lakes Observing System HF radar providing live snapshots of lake surface currents, 24 hours a day [97]. 20
- 3.4 Illustration of the effective number of measurement points η 25
- 3.5 Example of measurement point configurations in a coastal domain with different effective number of measurements η 26

- 5.1 Illustration of the fusion model methodology. The bounded domain, shown on the left, incorporates coastlines and represents the primary area of interest. The open domain, depicted in the middle, encloses the bounded domain and reflects broader environmental conditions. The fused velocity field, obtained by superimposing the two simulations, is displayed on the right. In the overlapping region, velocity values from both domains are interpolated and summed at each grid point. 33

- 6.1 Figure depicts the parametrization of boundary conditions by placing control points along the boundary, each specifying a pair (u_t, p) , with cubic spline interpolation used to generate the tangential velocity and pressure profiles. . . . 45
- 6.2 This figure illustrates the objective of adjusting the optimization variables at control points (green dots) until the red arrow (representing the current simulated velocity vector) aligns with the grey arrow (representing the referent velocity vector) for every measurement point (yellow cross). 46

6.3	Computational improvements from using field initialization in simulations. Colored bands represent simulation durations per iteration, bounded by the average minimum and maximum run times. Dotted lines show the average minimum, and dashed lines indicate the average maximum simulation times.	49
7.1	Visualization of the intersection between referent and simulated scalar fields, showing uncovered areas of referent scalar field and overestimated areas of the simulated scalar field.	53
7.2	Absolute and local coordinate systems, along with the agent's sensing function γ_i .	56
7.3	UAV navigation procedure based on dynamic probability fields.	60
8.1	The figure illustrates the coastline extraction polygon derived from the NDWI image. Blue colors represent water surfaces, while green areas correspond to land. The clear contrast between these regions reflects the NDWI value distribution, enabling accurate delineation of the coastline for mesh generation. . . .	62
8.2	Figure depicts the process of coastline extraction from the NDWI image. The largest constour representing raw coastline contour (blue) is smoothed (red) and prepared for conversion from pixels to geographic coordinates.	63
8.3	(A) Synthetic domain mesh with coastline generated with <code>blockMesh</code> . (B) Synthetic domain mesh without coastline generated with <code>blockMesh</code> . (C) Realistic domain mesh generated with <code>cfMesh</code>	63
8.4	Analysis of the multimodal characteristics of the flow fitting task. (A) shows the cavity lid scenario at $Re = 160$ with two marked observation points. (B) presents overlapping velocity profiles at point 48 (left marker), indicating identical local velocities from different boundary conditions, with another example shown in (C) at point 73 (right marker).	65
8.5	(A) The referent flow that needs to be reconstructed. (B) Velocities matched locally but field error threshold not met. (C) Main vortex captured, but northern flow diverges. (D) Distribution of optimization outcomes. (E) Both drifter and field errors are within limits. (F) Field error threshold met, but drifter error not met.	67

8.6	Overview of optimization algorithms for flow field reconstruction. Colored squares denote four outcome categories, while the lower panel shows average convergence trends.	69
8.7	Results of 100 optimization runs with 1–20 randomly distributed measurement points. (A) Optimization success based on measurement points. (B) Optimization success relative to the effective number of measurement points, while (C) presents their absolute distribution.	70
8.8	(A) Gulf of Trieste location. (B) HF-radar velocity vectors available at 225 locations for April 2012. (C) Positions of 44 drifters deployed between April 23 and May 4, 2012.	73
8.9	(A) Combined drifter and HF-radar data at 4:00 AM on April 24, 2012. (B) Flow reconstruction based on a 30% reduction of drifter measurements. (C) Flow reconstruction based on a 50% reduction of HF-radar measurements.	74
8.10	(A) Study area around Vis island, with over 2200 km ² . (B) Spatial distribution of 555 HF-radar velocity measurements, including four islands and parts of the mainland coastline.	75
8.11	(A) HF-radar measurement locations with velocity vectors colored by magnitude. (B) Reconstructed flow using 277 measurements and 278 field points (50% data reduction). (C) Reconstruction with 55 measurements and 500 field points (90% reduction).	76
8.12	Schematic of the optimization–simulation workflow initiated at time t for evaluating scalar transport over interval $[t, t + T_s]$	77
8.13	Reconstruction error (E_f) of the velocity field obtained for five different values of T_s	78
8.14	Figure shows one example of the evolving referent flow in the synthetic Simple Bay case after 9 hours (32400 seconds), comparing the initial flow state (A) with the final state (B).	79

8.15	(A) Referent flow after 32400 seconds. (B) Steady reconstruction from 15 drifter measurements. (C) Reconstruction with periodic measurement updates without fusion model. (D) Analysis of proposed metrics for passive scalar advection. (E) Reconstruction with measurement updates and a fusion model. (F) Reconstruction with measurement updates, fusion model, and adaptive diffusion compensation.	81
8.16	Evolution of the referent flow in Unije Channel after 10 hours (36000 seconds), showing the initial (A) and final (B) states with four inlet and outlet areas. . . .	82
8.17	(A) Referent flow after 36000 s. (B) Steady reconstruction from 15 drifters with no overlap of the passive scalar. (C) Transient reconstruction showing an even larger mismatch. (D) Analysis of proposed metrics for passive scalar advection. (E) The fusion model achieves high accuracy. (F) The fusion approach and adaptive diffusion closely match the referent passive scalar field.	83
9.1	Labeled AMEC TB-560 tracking beacons (left) and AMEC Cypho-150 AIS receiver with VHF antenna (right), used for receiving AIS transmissions.	86
9.2	AIS messages decoded using the Python pyais module	87
9.3	Overview of drifter setup: from design and acquisition to final assembly	88
9.4	Drifter deployment and AIS message reception using the AMEC Cypho-150 receiver	89
9.5	Results from deployment configuration 5 with 8 drifters in Plomin Bay. Left: drifter trajectories with final positions marked. Right: reconstructed steady surface flow from a single time step.	90
9.6	Comparison of real and simulated drifter trajectories in Plomin Bay, with dark lines showing observed paths and transparent lines showing 60-minute simulated paths from reconstructed flow.	91
9.7	Selected deployment locations across Valun Bay, generated using the Halton sequence for improved spatial uniformity (left). Field photos showing the preparation and release of drifters during the experiment (right).	93
9.8	Forecasted surface flow direction from publicly available prediction sources (left). Drifter trajectories recorded during the September 22, 2024, deployment where colored lines indicating individual drifter paths.	94

9.9	Flow reconstruction using the fusion model for the initial $t = 0$ s (A, B, C) and the final $t = 7200$ s (D, E, F) period.	95
9.10	The figure compares reconstructed drifter trajectories using a fixed wind approach and the fusion model based on measurements every 900 seconds over two hours. Darker lines show experimental paths, while transparent lines show reconstructed paths.	97
9.11	Comparison of reconstructed drifter trajectories using steady fit, transient fit and fusion model approach.	98
9.12	Illustration of a deployed target in the experiment.	99
9.13	UAV used in this realistic search scenario.	99
9.14	Illustration of the communication setup between the PC and UAV [187].	100
9.15	Examples of sea target detections with corresponding confidence levels.	100
9.16	Overview of the search framework integrating drifter data processing, flow field reconstruction, and UAV operations to locate objects at sea.	101
9.17	Base station with a view over the Valun Bay search area.	102
9.18	The search area with the reconstructed flow field, deployed target positions, and undetected target probability field at $t=0$	103
9.19	The reconstructed flow, probability of undetected targets, and estimated target positions at the start of the search, including their estimated trajectories after the 30-minute delay.	104
9.20	The reconstructed flow, probability of undetected targets, the UAV trajectory, detected target locations, and the estimated target positions and trajectories at the end of the search.	105
9.21	Reconstruction errors based on drifter velocity and position, from the beginning to the end of the search.	106

LIST OF TABLES

2.1	Overview of observation platforms and reconstruction techniques for sea surface velocity estimation.	11
3.1	Measurement characteristics of surface current data collection methods, including resolution and uncertainty ranges.	23
5.1	An overview of the OpenFOAM boundary condition type employed in flow simulations for surrogate model.	42
8.1	Characteristics of the simulation test cases.	64
8.2	Mesh characteristics and Grid Convergence Index (GCI) values for the synthetic Simple Bay case. Vorticity values were evaluated at all grid points.	71
8.3	Data coverage and reconstruction performance for the Gulf of Trieste.	74
8.4	Data availability for the Vis case.	76
9.1	Overview of AIS message types.	85
9.2	Overview of received AIS messages.	90

CURRICULUM VITAE

Karlo Jakac was born on 31 October 1996 in Rijeka, Croatia. He obtained his Bachelor's degree in Mechanical Engineering from the Faculty of Engineering, University of Rijeka, in 2019, and a Master's degree in Mechanical Engineering from the same institution in 2021. That same year, he began his doctoral studies in Technical Sciences, focusing on Mechanical Engineering, Fundamental Technical Sciences, and Interdisciplinary Technical Sciences. Since 2021, he has been working as an assistant at the Faculty of Engineering, where his research covers experimental studies, computational fluid dynamics (CFD), optimization methods, and autonomous unmanned aerial vehicle (UAV) control. As a member of the AOSeR project, he contributes to the development of an autonomous UAV system for oceanic search and rescue operations. Mr Jakac has performed multiple experimental validations of his proposed methods and has authored or co-authored seven scientific publications, five of which have been published in journals ranked in the top quartile (Q1) by Web of Science.

LIST OF PUBLICATIONS

Scientific papers in peer-reviewed journals:

1. Lanča, L., Jakac, K., Calinon S., and Ivić, S., 2025. Ergodic Exploration of Dynamic Distribution. *IEEE Robotics and Automation Letters*, 1 - 8, 2377-3766.
2. Lanča, L., Mališa, M., Jakac, K., and Ivić, S., 2025. Optimal Flight Speed and Height Parameters for Computer Vision Detection in UAV Search. *Drones*, 9(9), 595.
3. Jakac, K., Lanča, L., Sikirica, A. and Ivić, S., 2025. Efficient data-driven flow modeling for accurate passive scalar advection in submesoscale domains. *Applied ocean research*, 162, p.104699.
4. Dumenčić, S., Lanča, L., Jakac, K., and Ivić, S. 2025. Experimental Validation of UAV Search and Detection System in Real Wilderness Environment. *Drones*, 9(7), 473.
5. Jakac, K., Lanča, L., Sikirica, A. and Ivić, S., 2024. Approximation of sea surface velocity field by fitting surrogate two-dimensional flow to scattered measurements. *Applied ocean research*, 153, p.104246.

Conference papers:

1. Jakac, K., Lanča, L., Sikirica, A. and Ivić, S., 2025, February. Experimental Validation of Intelligent Ad Hoc System for Sea Surface Velocity Approximation. In 2025 11th International Conference on Automation, Robotics, and Applications (ICARA) (pp. 273-279). IEEE.
2. Lanča, L., Dumenčić, S., Jakac, K. and Ivić, S., 2025, February. Experimental Validation and Robustness Analysis of Ergodic UAV Control. In 2025 11th International Conference on Automation, Robotics, and Applications (ICARA) (pp. 257-261). IEEE.